Weighing the Giants: Measuring galaxy cluster masses with CMB lensing.

Submitted in Total Fulfillment
of the Requirements of the Degree of

Doctor of Philosophy

School of Physics

The University of Melbourne

Sanjaykumar Patil

Statement of contribution:

This is to certify that:

- This thesis entitled "Weighing the giants with CMB-lensing" comprises my original work towards the degree of Doctor of Philosophy.
- Due acknowledgement has been made in the text to all other material used.
- The thesis is less than 100,000 words in length, exclusive of tables, maps, bibliographies, and appendices.

Sanjaykumar Patil

Work dedicated to Amma, Appa, Akka, Bhava, and Vismaya.

Abstract

Galaxy clusters are powerful probes of cosmology. Their abundance depends on the rate of structure growth and the expansion rate of the universe, making the density of clusters highly sensitive to dark energy. Galaxy clusters additionally provide powerful constraints on matter density, matter fluctuation amplitude, and sum of neutrino masses. However, cluster cosmology is currently limited by systematic uncertainties in the cluster mass estimation. Generally, the cluster masses are estimated using observable-mass scaling relations where the observable can be optical richness, X-ray temperature etc. The observable-mass scaling relation depends on the complex cluster baryonic physics which is not well understood and any deviation in the baryonic physics will lead to uncertainties in the mass estimation. On the other hand, gravitational lensing offers one of the most promising techniques to measure cluster mass as it directly probes the total matter content of the cluster. Gravitational lensing can additionally be used to calibrate the observable-mass scaling relations. The gravitational lensing source can either be optical galaxies or the cosmic microwave background (CMB).

My thesis focuses on developing statistical and mathematical tools to robustly extract the cluster lensing signal from CMB data. We develop a maximum likelihood estimator to optimally extract cluster lensing signal from CMB data. We find that the Stokes QU maps and the traditional EB maps provide similar constraints on mass estimates. We quantify the effect of astrophysical foregrounds on CMB cluster lensing analysis. While the foregrounds set an effective noise floor for temperature estimator, the polarisation estimator is largely unaffected. We use realistic simulations to forecast that CMB cluster lensing is expected to constrain cluster masses to 3-6%(1%) level for upcoming (next generation) CMB experiments.

One of the standard ways to extract the CMB-cluster lensing signal is by using the quadratic estimator. The thermal Sunyaev-Zel'dovich effect (tSZ) acts as a major contaminant in quadratic estimator and induces significant systematic and statistical uncertainty. We develop modified quadratic estimator to eliminate the tSZ bias and to significantly reduce the tSZ statistical uncertainty. Using our modified quadratic estimator we constrain the mass of Dark Energy Survey year-3 cluster catalog. We also put constraints on the normalisation parameter of optical richness-mass scaling relation. In addition to removing the tSZ bias,

modified quadratic estimator also reduces tSZ induced statistical uncertainty by 40% in future low noise CMB-surveys.

Preface

While this thesis is substantially my own work, it also contains the work that has been done in collaboration with colleagues. This section describes the publications on which some of the chapters are based.

- Chapter 1 and 2 comprises a fully referenced literature review of the standard model of cosmology. Both the chapters have been written by me.

- Chapter 3 explains the Maximum Likelihood Estimator and is based on the work presented in the following publication
  Raghunathan, Patil, Baxter, Bianchini, Bleem, Crawford, Holder, Manzotti, and Reichardt (2017).
  The lensing pipeline and simulations were generated by Srinivasan Raghunathan. I did the validation of pipeline and quantified the systematic biases due to redshift uncertainty.

- Chapter 4 is based on the following publication
  Raghunathan, Patil, Baxter, Benson, Bleem, Chou, Crawford, Holder, McClintock, Reichardt, Rozo, Varga, Abbott, Ade, Allam, Anderson, Annis, Austermann, Avila, Beall, Bechtol, Bender, Bernstein, Bertin, Bianchini, Brooks, Burke, Carlstrom, Carretero, Chang, Chiang, Cho, Citron, Crites, Cunha, da Costa, Davis, Desai, Diehl, Dietrich, Dobbs, Doel, Eifler, Everett, Evrard, Flaugher, Fosalba, Frieman, Gallicchio, García-Bellido, Gaztanaga, George, Gilbert, Gruen, Gruendl, Gschwend, Gupta, Gutierrez, de Haan, Halverson, Harrington, Hartley, Henning, Hilton, Hollowood, Holzapfel, Honscheid, Hou, Hoyle, Hrubes, Huang, Hubmayr, Irwin, James, Jeltema, Kim, Carrasco Kind, Knox, Kovacs, Kuehn, Kuropatkin, Lee, Li, Lima, Maia, Marshall, McMahon, Melchior, Menanteau, Meyer, Miller, Miquel, Mocanu, Montgomery, Nadolski, Natoli, Nibarger, Novosad, Padin, Plazas, Pryke, Rapetti, Romer, Carnero Rosell, Ruhl, Saliwanchik, Sanchez, Sayre, Scarpine, Schaffer, Schubnell, Serrano, Sevilla-Noarbe, Smecher, Smith, Soares-Santos, Sobreira, Stark, Story, Suchyta, Swanson, Tarle, Thomas, Tucker, Vanderlinde, De Vicente, Vieira, Wang, Whitehorn, Wu, and Zhang (2019a).

I did the analysis using the simulations, applied it to the real data, and obtained the posterior probability distribution. In addition to that I quantified the bias due to our assumption of underlying cosmology and wrote the draft of introduction, data, results, and conclusion sections of the publication.

- Chapter 5 is based on:
  Patil, Raghunathan, and Reichardt (2019).
  I developed the new method to suppress the major foreground in lensing analysis, generated the simulations to validate the newly developed method, forecasted the mass uncertainties future surveys will achieve. I also wrote the entire draft with suggestions from Christian Reichardt and Srinivasan Raghunathan.

- Chapter 6 is entirely written by me. It summarizes all the work done during thesis and also sheds some light on future direction of CMB-cluster lensing.

In addition to the above mentioned publications, I have also been actively involved in:

- Raghunathan, Patil, Baxter, Benson, Bleem, Crawford, Holder, McClintock, Reichardt, Varga, Whitehorn, Ade, Allam, Anderson, Austermann, Avila, Avva, Bacon, Beall, Bender, Bianchini, Bocquet, Brooks, Burke, Carlstrom, Carretero, Castander, Chang, Chiang, Citron, Costanzi, Crites, da Costa, Desai, Diehl, Dietrich, Dobbs, Doel, Everett, Evrard, Feng, Flaugher, Fosalba, Frieman, Gallicchio, García-Bellido, Gaztanaga, George, Giannantonio, Gilbert, Gruendl, Gschwend, Gupta, Gutierrez, de Haan, Halverson, Harrington, Henning, Hilton, Hollowood, Holzapfel, Honscheid, Hrubes, Huang, Hubmayr, Irwin, Jeltema, Carrasco Kind, Knox, Kuropatkin, Lahav, Lee, Li, Lima, Lowitz, Maia, Marshall, McMahon, Melchior, Menanteau, Meyer, Miquel, Mocanu, Mohr, Montgomery, Corbett Moran, Nadolski, Natoli, Nibarger, Noble, Novosad, Ogand o, Padin, Plazas, Pryke, Rapetti, Romer, Roodman, Carnero Rosell, Rozo, Ruhl, Rykoff, Saliwanchik, Sanchez, Sayre, Scarpine, Schaffer, Schubnell, Serrano, Sevilla-Noarbe, Sievers, Smecher, Smith, Soares-Santos, Stark, Story, Suchyta, Swanson, Tarle, Tucker, Vanderlinde, Veach, De Vicente, Vieira, Vikram, Wang, Wu, Yefremenko, and Zhang (2019b)

- Raghunathan, Holder, Bartlett, Patil, Reichardt, and Whitehorn (2019c)

Contents

List of Tables

List of Figures

Chapter 1

Introduction

Cosmology answers the age-old question, "where did we come from?". Over the last two and half decades with flood of data from cosmological experiments, we have entered a "precision era" in cosmology. With the available cosmological data and the strong theoretical premises of the General Theory of relativity, the Universe can be divided into three main components. Only 5% of the universe is made up of baryons, which is mainly in the form of stars and gas in galaxies (Cooke et al., 2016). Approximately 27% is made up of dark matter, which is responsible for additional gravitational effects in the Large Scale Structures (Pryke et al., 2002). Remaining 68% is made up of elusive dark energy, which is responsible for the accelerated expansion of the universe (Riess et al., 1998). This chapter reviews the theoretical frame work of the homogenous universe with particular emphasis on the Cosmic Microwave Background (CMB) and it closely follows Dodelson (2003).

1.1 Expanding universe

In 1929, Edwin Hubble observed that the galaxies that are farther away from us are moving away at a faster rate (Hubble, 1929). This was the first observational evidence of expanding universe. The wavelength of the light traveling through space stretched by the Universe. This shift in wavelength to longer wavelengths is called redshift, z, and defined as:

$$z = \frac{\lambda_o - \lambda_e}{\lambda_e} = \frac{\lambda_o}{\lambda_e} - 1, \tag{1.1}$$

where λ_o and λ_e are the observed and emitted wavelengths respectively.

Hubble's data could be fit by a linear relation between galaxy velocity and its distance, a relation now known as Hubble's law

$$v = H_o d \tag{1.2}$$

where v is the velocity, d is the proper distance, and H_o is the Hubble constant which is usually expressed as

$$H_o = 100\, h\, \mathrm{km\,s^{-1}Mpc^{-1}} \tag{1.3}$$

where h is the dimensionless Hubble parameter, measured by Planck Collaboration et al. (2018) to be $h = 0.674 \pm 0.005$. Assuming the Universe is expanding at constant rate, v constant and at $t = 0$ the Universe started. Through simple math we can get rough age of the Universe also known as the Hubble time,

$$t_H = \frac{1}{H_0} = 9.836 \times 10^9\, h^{-1}\, \mathrm{yr}. \tag{1.4}$$

Hubble distance is defined as the distance light travelled in Hubble time which is roughly $3 \times 10^3\, h^{-1}$ Mpc.

The current paradigm of cosmology rests on the following three main assumptions

- General Theory of Relativity is valid on all length scales in the universe
- The different components of the universe obey equation of state
- universe is homogeneous and isotropic at sufficiently large length scales (Copernican Principle or CP)

The Friedmann-Lemaître-Robertson-Walker (FLRW) metric is the only metric in General Relativity consistent with the Copernican principle and expanding universe. The FLRW metric is given by:

$$ds^2 = dt^2 - a^2(t)\left[\frac{dr^2}{1-kr^2} + r^2(d\theta^2 + sin^2(\theta)d\phi^2)\right] \tag{1.5}$$

where $a(t)$ is the scale factor, r is the comoving distance, k is the curvature ($k = 0$ in flat ΛCDM cosmology) and the speed of light is assumed to be unity ($c = 1$).

1.2 Cosmological distances

While measuring distances is crucial in understanding the underlying cosmology, it can be tricky in an expanding universe. In a time interval dt light travels a comoving distance of $dt/a(t)$. The comoving distance light has travelled since the

beginning of the universe is obtained by integrating the equation below,

$$\eta = \int_0^t dt/a(t) \tag{1.6}$$

This distance, η, defines the comoving horizon, no information could have travelled between the regions that are separated by distance $> \eta$. We can get the comoving distance between an astrophysical object at redshift of z in a similar way

$$\chi(a) = \int_0^z \frac{dz'}{H(z')} \tag{1.7}$$

where $H(z) = \dot{a}/a$ is the Hubble parameter which depends on the cosmology. At late times the universe is matter dominated, so we can ignore the contribution of the other components in the universe. Under the assumptions, $\Omega_m = 1$ and $\Omega_\Lambda = 0$, we can analytically integrate the above equation

$$\chi(a) = \frac{2}{H_0}\left[1 - \frac{1}{\sqrt{1+z}}\right] \tag{1.8}$$

Another way to measure the distance in cosmology is by measuring the angle θ subtended by an object of know physical size l.

$$d_A = \frac{l}{\theta} \tag{1.9}$$

The subscript 'A' stands for the angular diameter distance. The comoving size of an object is given by l/a, the angle subtended in terms of comoving distance is $\theta = (l/\mathrm{a})/(\chi)$, plugging this in above equation gives

$$d_A = a\chi = \frac{\chi}{1+z} \tag{1.10}$$

Observed flux can be used to measure the luminosity distance of a cosmological object.

$$F = \frac{L(\chi)}{4\pi\chi^2} \tag{1.11}$$

where F is the observed flux and $L(\chi)$ is the comoving luminosity. Comoving Luminosity is related to intrinsic luminosity as $L(\chi) = La^2$, plugging this in the

above equation we get Luminosity distance as

$$d_L = \chi * (1 + z) \tag{1.12}$$

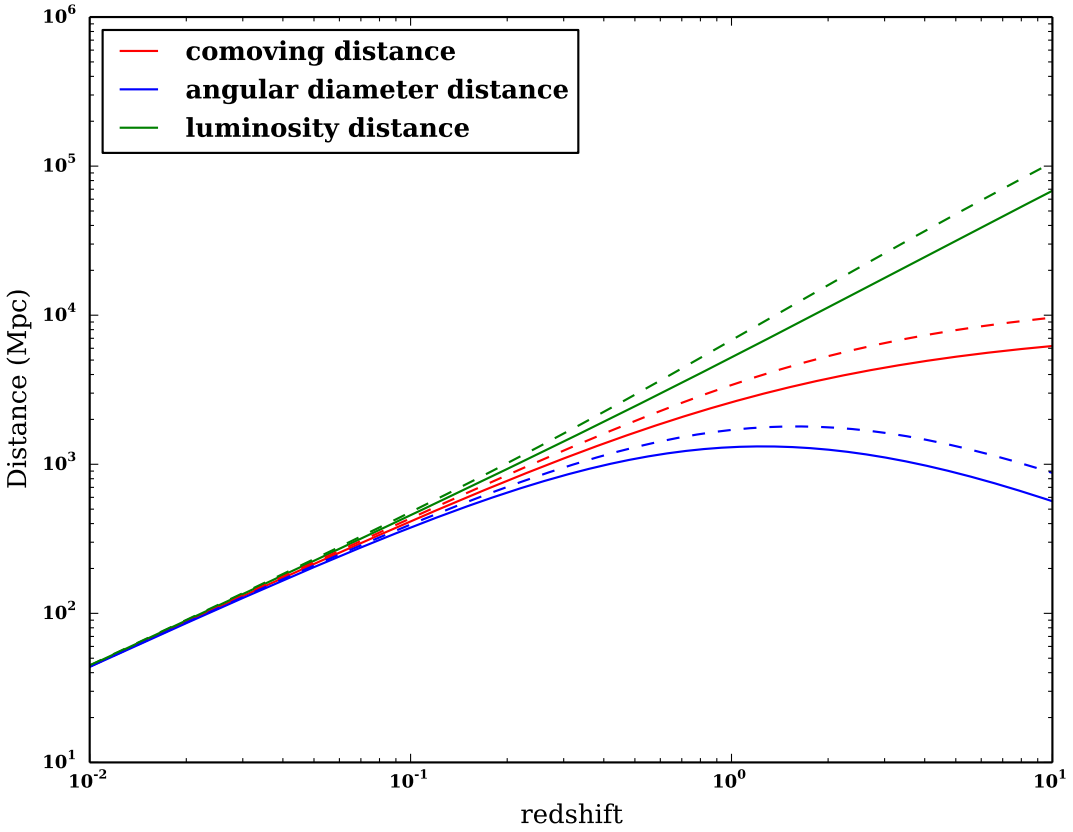

Figure 1.1: Cosmological distances as a function of redshift - solid lines represent matter dominated universe and dashed lines represent Planck Collaboration et al. (2018) cosmology. Measuring distance as a function of redshift provides valuable information on the constituent of the Universe.

Fig. 1.1 shows cosmological distances as a function of redshift; dashed lines represent the *Planck* (Planck Collaboration et al., 2018) cosmology and solid lines represent matter only universe.

1.3 Friedmann Equations

The mathematical formalism of the universe so far based on the assumption of isotropy and homogeneity in an expanding universe which led us to the FLRW metric. General theory of relativity relates the dynamics of the background universe to the matter and energy content in the universe via the Einstein Field

Equations

$$R_{\mu\nu} - \frac{1}{2}g_{\mu\nu}R = 8\pi G T_{\mu\nu}. \tag{1.13}$$

The L.H.S corresponds to the geometry of the universe, while the R.H.S represents the matter and energy content in the universe. In the above equation $R_{\mu\nu}$ is the Ricci tensor which depends on the metric and its derivatives, R is the Ricci scalar and $g_{\mu\nu}$ is the metric. The stress energy tensor, $T_{\mu\nu}$, is given by:

$$T^{\mu}_{\nu} = (\rho + P)u^{\mu}u_{\nu} - P\delta^{\mu}_{\nu} \tag{1.14}$$

where $\rho(t)$ and P(t) are the energy density and pressure in the rest frame of the fluid and u^{μ} is the relative four velocity of the fluid. Solving the time-time component of the Einstein field equation yields an equation for the evolution of the scale factor,

$$H^2 = \left(\frac{\dot{a}}{a}\right)^2 = \frac{8\pi G}{3}\rho - \frac{k}{a^2} \tag{1.15}$$

while all three spatial components reduce to

$$\frac{\ddot{a}}{a} = -\frac{4\pi G}{3}(\rho + 3P) \tag{1.16}$$

where $\rho = \Sigma_i \rho_i$ and $P = \Sigma_i P_i$ are the sum of energy density and pressure of all the components in the universe respectively. Equations 1.16 and 1.15 are the Friedmann equations governing the evolution of the background universe.

The average mass density of the Universe required to just halt the expansion of the Universe, it is given by,

$$\rho_{crit} = \frac{3H^2}{8\pi G} \tag{1.17}$$

Note that the value of critical density depends on Hubble's constant which is time dependent. The present value of critical density is approximately $10^{-26} kg/m^3$. While this is equivalent to 6 hydrogen atoms per cubic meter, the best achievable terrestrial vacuum is 10^9 atoms per cubic meter. The critical density can be used to define dimensionless density parameters as $\Omega_i = \rho_i/\rho_{crit}$. Assuming all the components in the universe are perfect isotropic fluids, we can write down the

stress energy tensor as

$$T^{\mu}_{\nu} = \begin{pmatrix} -\rho & 0 & 0 & 0 \\ 0 & P & 0 & 0 \\ 0 & 0 & P & 0 \\ 0 & 0 & 0 & P \end{pmatrix} \tag{1.18}$$

Using the energy-momentum conservation condition

$$\dot{\rho} + 3H(\rho + P) = 0 \tag{1.19}$$

Note that the continuity equation will also hold for individual species as long as we neglect the energy exchange among different components. As mentioned earlier the cosmological fluids are expected to obey the equation of state: P = w ρ. Plugging this in the above equation we can solve for density as function of scale factor

$$\rho(a) \propto \exp\left(-3 \int_1^a \frac{da'}{a'}[1 + w(a')]\right) \tag{1.20}$$

For a time-independent equation of state parameter w the above equation reduces to $\rho \propto a^{-3(1+w)}$.

The components of the Universe that we know about are:

- **Non relativistic matter**: For non-relativistic matter such as cold dark matter and baryons the energy density is equal to the rest mass energy. The pressure is much smaller than the energy-density ($P \ll \rho$). In such cases $w = 0$ and the density will scale as $\rho \propto a^{-3}$

- **Radiation and relativistic matter**: Pressure is related to the energy-density of relativistic matter as $P = 1/3\rho$. This includes photons and neutrinos whose density scales with scale factor as $\rho \propto a^{-4}$

- **Dark Energy**: It is a hypothetical form of energy which is responsible for late time cosmic acceleration. The equation of state parameter depends on the model of Dark Energy and in many of models the equation of state is time dependent. However the current data suggests the value equation of state parameter to be consistent with $w = -1$, with the Planck Collaboration et al. (2018) indicating $w = -1.04 \pm 0.1$. Substituting it in the above equation we get $\rho \propto a^0$ and hence the cosmic dilution doesn't affect the dark energy density.

It is important here to note that the cosmic dilution has different effect on different components. While radiation component is subdominant in today's universe, it played a major role in the early universe. Fig. 1.2 shows the energy density of different components as a function of scale factor; as one expects at late times cosmological constant and matter are the dominant components, whereas at earlier times radiation plays a significant role in the evolution of background universe. With the density scaling relations in hand and substituting a = 1/(1+z), we can

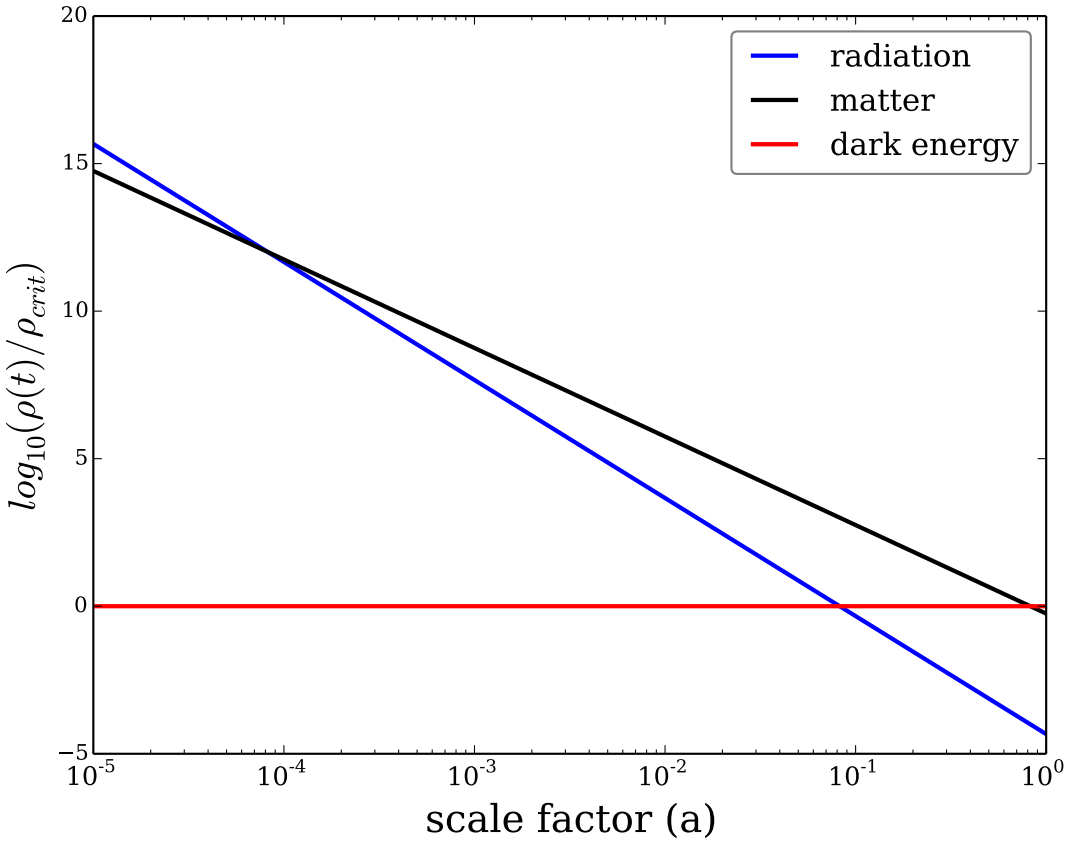

Figure 1.2: Scaling of various components as function of scale factor (a). While radiation is dominant component in the early universe, dark energy is dominant at present.

rewrite Eqn. 1.15 for a flat universe as

$$H^2(z) = H_0^2(\Omega_{ro}(1+z)^4 + \Omega_{mo}(1+z)^3 + \Omega_\Lambda) \tag{1.21}$$

where Ω_{ro},Ω_{mo} and Ω_Λ are the density parameters of radiation, matter and dark energy respectively.

1.4 Cosmic Microwave Background

Cosmic Microwave Background (CMB) was theoretically predicted by George Gamov in 1940s as an observational relic of Hot Big Bang model (Gamow, 1946). It was observed accidentally by Arno Penzias and Robert Wilson in 1964 at the Bell Laboratories for which there were awarded Nobel prize in physics in 1978 (Penzias and Wilson, 1965). Almost three decades after its discovery, Cosmic Background Explorer (COBE) detected anisotropies in CMB at a tiny level of 10 in a million. Far-Infrared Absolute Spectrophotometer (FIRAS), an instrument mounted on COBE measured the black body spectrum of CMB (Mather et al., 1994). Since then a number of experiments have been designed to measure the anisotropies in the CMB.

High density and temperature of the early universe ensured that all the components interacted with each other multiple times remaining in thermal equilibrium. Photons (γ), protons (p) and electrons (e) were tightly coupled into a state called photon-baryon plasma; proton and electrons interacted with each other through Coulomb scattering and photon interacted with electrons through Thompson scattering:

$$\mathrm{p} + \mathrm{e}^- \rightleftharpoons \mathrm{H} + \gamma \tag{1.22}$$

$$\gamma^+ \mathrm{e}^- \rightleftharpoons \mathrm{e}^- + \gamma \tag{1.23}$$

As the universe expands the mean energy density dilutes and the temperature decreases. When the temperature falls below the ionization energy of hydrogen, $\mathrm{E} < 13.6$ eV the reaction in Eq. 1.22 thermodynamically favours to $\mathrm{p} + \mathrm{e}^- \longrightarrow \mathrm{H} + \gamma$ [1]. This results in the creation of neutral hydrogen atoms and the electron density decreases, which results in the decoupling of photons from the baryons. This epoch is called the epoch of recombination; observations determine that it happened at redshift of $z = 1089.90 \pm 0.23$ (Planck Collaboration et al., 2018).

As a first light from the early universe, the CMB provides a wealth of cosmological information. The theory of inflation is able to describe the homogeneity measured in the CMB. The inhomogeneties are only of order of 10 in a million which can be directly measured from the observed anisotropies in CMB.

[1] To be precise, recombination occurs at slightly lower temperature (1MeV) due to the large over abundance of photons with respect to baryons

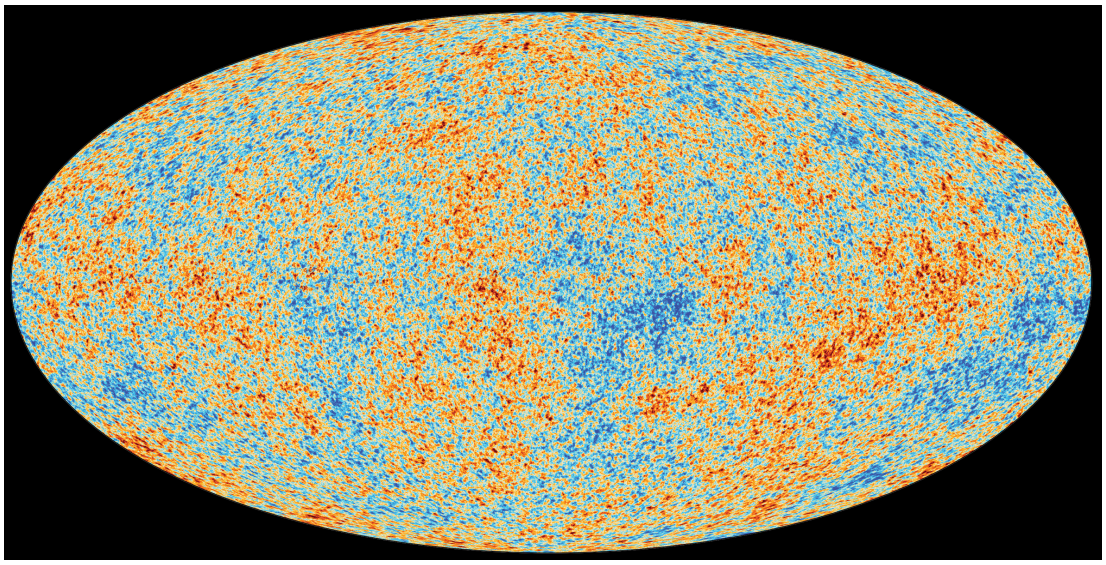

Figure 1.3: CMB anisotropies as observed by *Planck* satellite. Credits: ESA/*Planck* collaboration

1.5 Temperature primary anisotropies

The measured CMB temperature in a given direction $\hat{n}$ can be written as:

$$T = T_0 \left(1 + \vec{\beta}.\hat{n} + \frac{T(\hat{n})}{T_0}\right) \tag{1.24}$$

where T_0 is the average CMB temperature, $\vec{\beta}$ is the dipole term due to the relative velocity of Earth with respect to Hubble flow. Here β is equal to $\frac{\vec{v}}{c}$ where $\vec{v}$ is the Earth's relative velocity. The last term in the equation represents the anisotropies in the CMB which here after we denote by $\Phi(\hat{n}) = \frac{T(\hat{n})}{T_0}$. Note that in the above equation we have ignored foregrounds, systematics, and experimental noise.

Given the stochastic nature of fluctuations in CMB, we cannot predict the value of temperature at a given location. However, we can predict the statistical properties. As an function on the surface of sphere, CMB fluctuations can be decomposed in terms of spherical harmonics as follows:

$$\Phi(\hat{n}) = \Sigma_l \Sigma_m a^T_{lm} Y_{lm}(\hat{n}) \tag{1.25}$$

$$a^T_{lm} = \int d\Omega \Phi(\hat{n}) Y_{lm}(\hat{n}) \tag{1.26}$$

where Y_{lm} are the spherical harmonic basis, a^T_{lm} are the harmonic coefficients. It

is important to note here that angular scale θ is related to multipole l as $\theta \sim 1/l$.

The randomness of the fluctuations wont let us predict the value of the harmonic coefficient a^T_{lm}. However, theories do predict the distribution from which the a^T_{lm} are picked. In the inflationary paradigm CMB fluctuations are realisations of a Gaussian random field, meaning that the harmonic coefficients are drawn from random Gaussian distribution[2]. The harmonic coefficients satisfy

$$\langle a^T_{lm} \rangle = 0, \tag{1.27}$$

$$\langle a^T_{lm} a^{T*}_{l'am'} \rangle = \delta_{ll'}\delta_{mm'}C^{TT}_l, \tag{1.28}$$

$$a^T_{l-m} = (-1)^m a^{T*}_{lm} \tag{1.29}$$

where $\langle\rangle$ denotes the ensemble average over many realisations, C^{TT}_l is the angular power spectrum of CMB.

Our universe is only one of many realisations of the Gaussian random field, so we face fundamental limits on the knowledge available. This is known as cosmic variance. However, we can still calculate the angular power spectrum. The idea is to replace the ensemble average with the spatial sample average i.e averaging over $2l + 1$ samples.

$$\hat{C}^X_l = \frac{1}{2l+1}\Sigma_m |a^X_{lm}|^2 \tag{1.30}$$

where X ϵ (T,E,B) - T is the temperature mode and E, B are the polarisation modes . This measured power spectrum is fitted to the theoretical power spectrum to extract cosmological information. For historical reasons the CMB power spectrum is conventially parameterized as

$$D_l = \frac{l(l+1)}{2\pi} C_l. \tag{1.31}$$

The theoretical CMB power spectrum for standard ΛCDM cosmology as obtained from CMBFAST (Seljak and Zaldarriaga, 1996) is show in Fig. 1.4. A wealth of cosmological information can be obtained from CMB power spectrum and below I discuss three main features (it closely follows Scott and Smoot (2010)):

Sachs-Wolfe Plateau:

The horizon scale at last scattering surface corresponds to multipole $l \approx 100$.

[2]It must be noted that most of the inflationary models predict a small amount of non-Gaussianity.

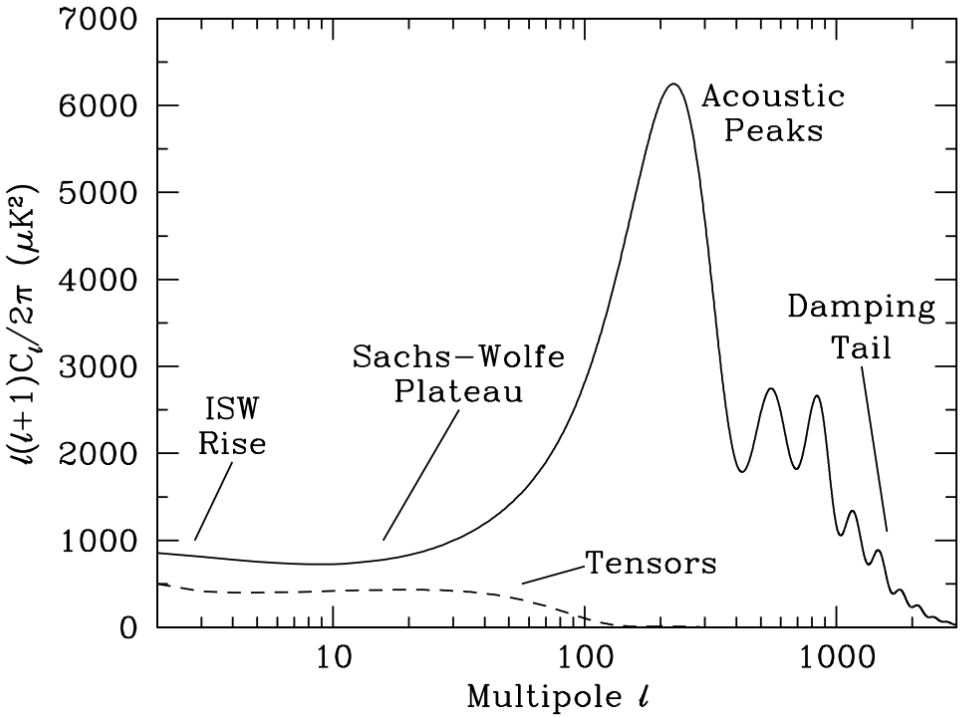

Figure 1.4: The theoretical CMB power spectrum as obtained from CMBFAST (Seljak and Zaldarriaga, 1996)

At these scales the anisotropies have not evolved significantly and hence faithfully trace initial condition. $\delta T/T \approx 1/3\delta\phi c^2$, where $\delta\phi$ is the perturbation to the gravitational potential evaluated on the last scattering surface (LSS) (Sachs and Wolfe, 1967).

Acoustic oscillations:

On sub-degree scales, corresponding to multipole range $100 \leq l \leq 1000$, the rich structure in the power spectrum is due to gravity-driven acoustic oscillations occurring before the atoms in the Universe became neutral. Perturbations inside the horizon at last scattering have been able to evolve causally and produce anisotropy at the last scattering epoch, which reflects this evolution. The frozen-in phases of these sound waves imprint a dependence on the cosmological parameters, which gives CMB anisotropies their great constraining power. Location and height of acoustic peaks are sensitive to various cosmological parameters especially curvature of the Universe, dark energy, amount of baryons, optical depth, and dark matter (Hinshaw et al., 2013; Planck Collaboration et al., 2018).

Damping tail:

The recombination process is not instantaneous, giving a thickness to the last scattering surface. This leads to a damping of the anisotropies at the highest ls, corresponding to scales smaller than that subtended by this thickness. One can also think of the photon-baryon fluid as having imperfect coupling, so that there is diffusion between the two components, and hence the amplitudes of the oscillations decrease with time. These effects lead to a damping of the C_ls, sometimes called Silk damping (Silk, 1968), which cuts off the anisotropies at multipoles above about 2000 (Keisler et al., 2011; Story et al., 2013; Das et al., 2011a; Reichardt et al., 2009).

The CMB interacts with the intervening medium (between last scattering surface and us) and this imprints secondary anisotropies. Secondary anisotropies also provide wealth of cosmological information especially on structure formation and epoch of reionisation (Lueker et al., 2010; Shirokoff et al., 2011; Fowler et al., 2010; Das et al., 2011b).

1.6 CMB polarisation

The CMB is partially polarised linearly at the 10% level due to the Thompson scattering of photons by electrons at the surface of last scattering. Only quadrupole anisotropy is responsible for CMB polarisation as shown in Fig. 1.5. The Fig. 1.5 represents important scenarios experienced by electron at the time of recombination. Red and blue represent relatively hot and cold photons respectively; green represents the average temperature. Image on the top left represents the isotropic scenario which results in no net anisotropy. On the top right is that of dipole anisotropy which also results in no net polarisation. Only the quadrupole anisotropy which is shown in the bottom panel results in net linear polarisation.

The polarisation pattern on the CMB sky can be decomposed into curl-free E-modes, and divergence-free B-modes. This is similar to Maxwell?s equation where the curl of the electrostatic field, and the divergence of the magnetic field are zero. The reason the polarisation patterns are called E, B modes is because of this similarity to electromagnetism.

$$\vec{\nabla} \times \vec{E} = 0 \tag{1.32}$$

$$\vec{\nabla}.\vec{B} = 0 \tag{1.33}$$

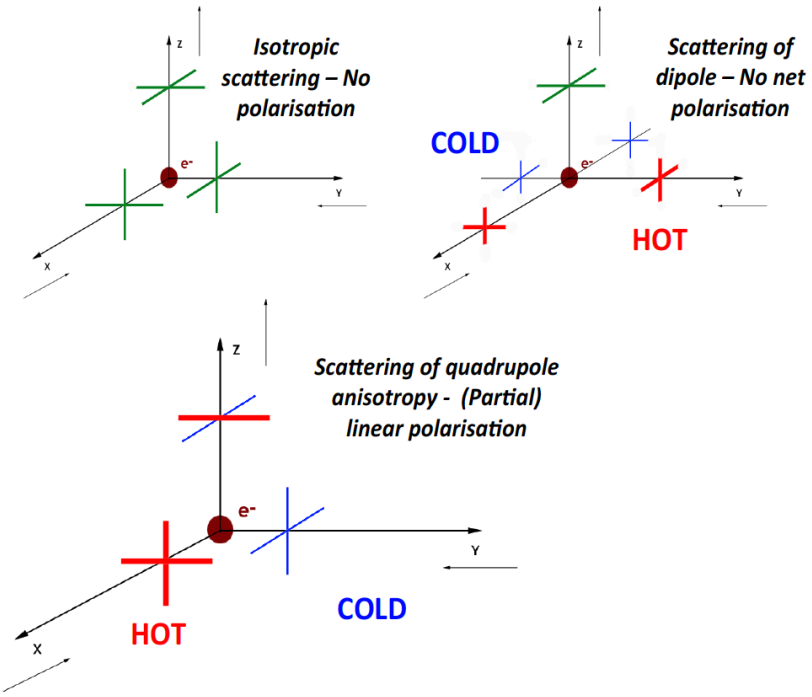

Figure 1.5: The above figure depicts important scenarios as experienced by an electron at the time recombination; it is adopted from the works of Hu and White (1997) and Dodelson (2003).

The most important reason for this decomposition is that the scalar perturbations only generate E-modes but does not generate B-modes, and the tensor perturbations generate both E, and B-modes in equal amounts. Though CMB polarisation signal is weak compared to its temperature counterpart, it provides invaluable information on inflation and on late time evolution of universe through its lensing effects and the imprint of primordial gravitational waves on tensor B-modes In addition to that, foregrounds are only partially polarised. The CMB polarisation was first detected observationally by Degree Angular Scale Interferometer (DASI) in 2002 (Kovac et al., 2002). Since then measurement of CMB polarisation has been done by SPT (Henning et al., 2018; Sayre et al., 2019; Keisler et al., 2015), ACT (Louis et al., 2017; Naess et al., 2014), *Planck* (Planck Collaboration et al., 2019), BICEP2/Keck (BICEP2 Collaboration et al., 2018; BICEP2 and Keck Array Collaborations et al., 2015), and POLARBEAR (PO-

LARBEAR Collaboration, 2014; Adachi et al., 2019).

1.7 Other cosmological probes

In addition to CMB there are other cosmological probes which provide invaluable and complementary insight into the standard model of cosmology. Below I provide a very brief discussion of other cosmological probes.

Supernovae:

Type Ia supernovaes are excellent standard candles for measuring the expansion history of the Universe and provided the first direct evidence of dark energy (Riess et al., 1998; Perlmutter et al., 1999; Perlmutter et al., 1999). Theoretical models suggest that these "standard candles" arise because of thermonuclear explosion of a carbon-oxygen white dwarf that has grown to the Chandrashekar mass. These events have well defined Hubble diagram whose intercept provides a robust measurement of Hubble constant. The value of hubble constant measured using Type Ia supernovae data from Dark Energy Survey is $H_O = 67.8 \pm 1.3\,\mathrm{km\,s^{-1}Mpc^{-1}}$ (Macaulay et al., 2019).

Baryon Acoustic Oscillations:

While supernovae acts as "standard candles", Baryon Acoustic Oscillations (BAO) acts as standard rulers in cosmology. They are the frozen relics left over from the pre-decoupling universe. As such, probing the BAO scales at different times provides valuable cosmological information. The best measurement BAO scale comes from CMB anisotropy measurements at redshift $z \approx 1100$ (Planck Collaboration et al., 2018). BAO are also present in the distribution of matter, and there are measurements at low redshifts using the clustering of galaxies (Beutler et al., 2011; Ross et al., 2015; Alam et al., 2017). BAO data can only constrain a combination of the size of the sound horizon and the expansion rate of the Universe (H_o). Usually CMB anisotropy measurements are used to break this degeneracy. Using the Big Bang Nucleosynthesis prior and latest data from eBOSS DR14, Cuceu et al. (2019) measured $H_O = 67.6 \pm 1.1\mathrm{km\,s^{-1}Mpc^{-1}}$.

Chapter 2

Cluster Cosmology

2.1 Overview

In the last chapter, I introduced the CMB anisotropies which are sourced by small pertrubations of density in the early Universe. With time and gravity, these initially tiny perturbations grow to become structures such as galaxies, galaxy clusters. This process of structure growth yields a plethora of tests of the cosmological model.

2.2 Linear theory of structure formation

In this section, I will describe the evolution of matter density perturbations in the linear regime. This section closely follows Ryden (2003). Assuming that universe is filled with pressure less matter with mean mass density $\rho_m(t)$. By inducing a small density fluctuation ($\delta \ll 1$) within a region of spherical radius 'R'

$$\rho(t) = \rho_m(t)(1+\delta). \tag{2.1}$$

The gravitational pull on the outer shell of the sphere is given by

$$\ddot{R} = -\frac{GM}{R^2} \tag{2.2}$$

where $M = 4\pi/3\,\rho R^3$ is the total mass within the sphere, we can rewrite Eqn. 2.2

$$\frac{\ddot{R}}{R} = -\frac{4\pi}{3}G\rho_m - \frac{4\pi}{3}G\rho_m\delta. \tag{2.3}$$

As the sphere expands the mass within the sphere is conserved

$$M = \frac{4\pi}{3}\rho_m(t)[1+\delta(t)]R(t)^3. \tag{2.4}$$

From which we get

$$R(t) \propto \rho_m(t)^{-1/3}[1+\delta(t)]^{-1/3}. \tag{2.5}$$

Since $\rho_m \propto a^{-1/3}$ in an expanding universe,

$$R(t) \propto a(t)[1+\delta(t)]^{-1/3}. \tag{2.6}$$

Taking two time derivatives of the above equation we get

$$\frac{\ddot{R}}{R} = \frac{\ddot{a}}{a} - \frac{1}{3}\ddot{\delta} - \frac{2\dot{a}}{3a}\dot{\delta}. \tag{2.7}$$

Rearranging the above equations we get

$$\frac{\ddot{a}}{a} - \frac{1}{3}\ddot{\delta} - \frac{2\dot{a}}{3a}\dot{\delta} = -\frac{4\pi}{3}G\rho_m(1+\delta). \tag{2.8}$$

We now want to split this up between the dynamics of the unperturbed universe ($\delta = 0$) and perturbation

$$\frac{\ddot{a}}{a} = -\frac{4\pi}{3}G\rho_m. \tag{2.9}$$

Substituting the above relation in Eqn. 2.8 yields

$$-\frac{1}{3}\ddot{\delta} - \frac{2\dot{a}}{3a}\dot{\delta} = -\frac{4\pi}{3}G\rho_m\delta, \tag{2.10}$$

or

$$\ddot{\delta} + 2H\dot{\delta} = 4\pi G\rho_m\delta. \tag{2.11}$$

In the early radiation dominated phase of the universe $\Omega_m \ll 1$ and $H = 1/(2t)$ which results in

$$\ddot{\delta} + \frac{1}{t}\dot{\delta} \approx 0, \tag{2.12}$$

solving which we get,

$$\delta(t) \approx C_1 + C_2 \ln t \tag{2.13}$$

During the radiation dominated epoch, baryon density oscillated as baryons and photons were tightly coupled. Whereas the dark matter density grew at a logarithmic rate as predicted by the above equation. Similarly, during the dark energy dominated epoch Eqn. **??** takes the form

$$\ddot{\delta} + 2H_\Lambda\dot{\delta} \approx 0 \tag{2.14}$$

which results in

$$\delta(t) \approx D_1 + D_2 e^{-2H_\Lambda t}. \tag{2.15}$$

Dark matter density perturbation exponentially decays off in dark energy dominated epoch.

During the matter dominated epoch, density perturbations follow

$$\ddot{\delta} + \frac{4}{3t}\dot{\delta} - \frac{2}{3t^2}\delta = 0. \tag{2.16}$$

Assuming a power law solution of the form Dt^n and plugging it in above equation we get

$$\delta(t) \approx D_1 t^{2/3} + D_2 t^{-1}. \tag{2.17}$$

Thus during matter domination matter perturbation grow as $t^{2/3}$. Given these different dynamics, studying how density perturbations grow can yield strong tests of cosmology and the constituents of the Universe.

2.3 Power spectrum

In Fourier space the perturbations can be written as

$$\delta(k) = \frac{1}{V}\int_0^\infty \delta(x) e^{ik.x} d^3x. \tag{2.18}$$

The matter power spectrum and auto correlation are related as follows:

$$\langle \delta(x)\delta^*(x)\rangle = \int_0^\infty \frac{dk}{k}\frac{k^3|\delta^2(k)|}{2\pi^2} = \int_0^\infty \frac{dk}{k}\frac{k^3 P(k)}{2\pi^2} \tag{2.19}$$

where by definition $P(k) = |\delta^2(k)|$ is the matter power spectrum. In the inflationary paradigm, the primordial fluctuations are quantum fluctuations that have been blown up to macroscopic scale by inflation. In inflationary models, this primordial fluctuations are nearly scale invariant, since inflation has no preferred scale,

$$P_{primordial}(k) \propto k \tag{2.20}$$

The primordial densities grow in a complicated way as explained in the previous section; the evolved matter power spectrum can be written as fucntion redshift and wave number as

$$P(k,z) = P_{primordial}(k) D(z)^2 T(k,z)^2 \tag{2.21}$$

where $D(z)$ is the growth factor and $T(k,z)$ is the transfer function. Growth factor for cold dark matter is given by

$$D(z) = H(z) \int_z^\infty \frac{dz'(1+z')}{H^3(z')}. \tag{2.22}$$

The transfer function depends on the complex interactions between various components in the universe. While there are approximated expression for transfer function, however, the robust solution of the transfer function can only be obtained numerically. Numerical codes such as CAMB (Lewis et al., 2000), CLASS (Seljak and Zaldarriaga, 1996) etc., solve the multi -component Boltzmann equations to provide T(k,z) for a given set of parameters.

2.4 Statistics of spherically collapsed objects

In the previous sections we introduced equations for density perturbations in both real and Fourier space. However, in practice, we observe the density perturbation averaged over a given volume which we define as 'density contrast'. Mathematically, density contrast within a radius 'R' is given by

$$\Delta(x,R) = \int d^3x' W(|x'-x|)\delta(x') \tag{2.23}$$

$$\Delta(k,R) = W(k,R)\delta(k) \tag{2.24}$$

where W(x,R) (W(k,R) is its Fourier transform) is the window which weighs the density field,

$$W(x,R) = constant \ (x < R) \tag{2.25}$$

$$= 0 \ (x \geq R) \tag{2.26}$$

The variation in the observed density contrast in a sphere of radius R is given by

$$\sigma^2(R) = \langle \Delta^2(x,R) \rangle = \int d\ln k \nabla^2(k) |W(k,R)|^2 \tag{2.27}$$

where $\nabla(k) = \sqrt{k^3 P(k)/2\pi^2}$ is the dimensionless power spectrum. Assuming that the density field follows Gaussian random distribution, which is well supported by observation. The probability that the sphere of radius, R, has density contrast

δ is given by

$$P(\Delta, R) = \frac{1}{\sqrt{(2\pi\sigma^2(R))}} \exp\left(-\frac{\delta^2}{2\sigma^2(R)}\right) d\delta. \tag{2.28}$$

It is important to note here that we can also express $P(\Delta, R) = P(\Delta, M)$, where R is related to M as $M = \frac{4\pi}{3}\rho R^3$. Also, σ_8, a standard cosmological parameter is nothing but the density contrast in a sphere of radius $8h^{-1}$ Mpc

2.4.1 The Press-Schechter Theory

In 1974, Press and Schechter came up with a simple model to predict the number of dark matter halos (Press and Schechter, 1974). The basic idea is that a sphere of radius 'R' with density contrast Δ will form a dark matter if Δ greater than a critical value Δ_c. The probability of finding dark matter halos with mass greater than M is given by

$$F(M) = \int_{\Delta_c}^{\infty} P(\Delta, M) d\Delta = \frac{1}{2} erfc\left(\frac{\nu}{\sqrt{(2)}}\right) \tag{2.29}$$

where $\nu = \Delta_c/\sigma(M)$. The halo mass function, i.e, the number density of halos between mass M and M+dM is given by

$$\frac{dn(M,z)}{dM} = -\sqrt{\frac{2}{\pi}} \frac{\rho_m}{M} \frac{\Delta_c}{\sigma^2(M,z)} \frac{d\sigma(M,z)}{dM} \exp\left(-\frac{\Delta_c^2}{2\sigma^2(M,z)}\right). \tag{2.30}$$

The above equation predicts too many low-mass halos and too few high-mass halos compared to the N-body simulations. For precise cosmological applications, current estimates of the halo mass function rely on some form of Eqn. 2.30 with some additional fitting parameters to achieve a better fit, for example Tinker et al. (2008); Jenkins et al. (2001).

2.5 Galaxy Clusters & Cosmology

2.5.1 Galaxy Clusters

According to the standard model of cosmology, galaxy clusters are the largest and most recent gravitationally collapsed objects to form because structure grows hierarchically. A galaxy cluster contains hundreds to thousands of galaxies that are bound together by gravity. These are very massive objects with typical masses ranging from $10^{14} - 10^{15}$ times the mass of Sun ($M_\odot$). The majority the mass is in

the form of invisible dark matter (80-87%), which on an average follows a spherically symmetric Navarro-Frenk-White (NFW) model (Navarro et al., 1997)[1]. On an average around 12% of the cluster mass is in the form of hot intracluster medium (ICM)- a sparse hot plasma that fills the cluster. The temperature of the ICM is of order ten million Kelvin and thus the ICM predominantly emits X-rays. The remaining 2% (on average) of the cluster mass is in the form of stars, cold gas, and dust in galaxies. [2]

[1]There is considerable deviation from NFW for individual clusters due to asphericity, substructure, recent merger activity etc.,

[2]Note that the percentage contribution of ICM and stars may considerably deviate for individual clusters

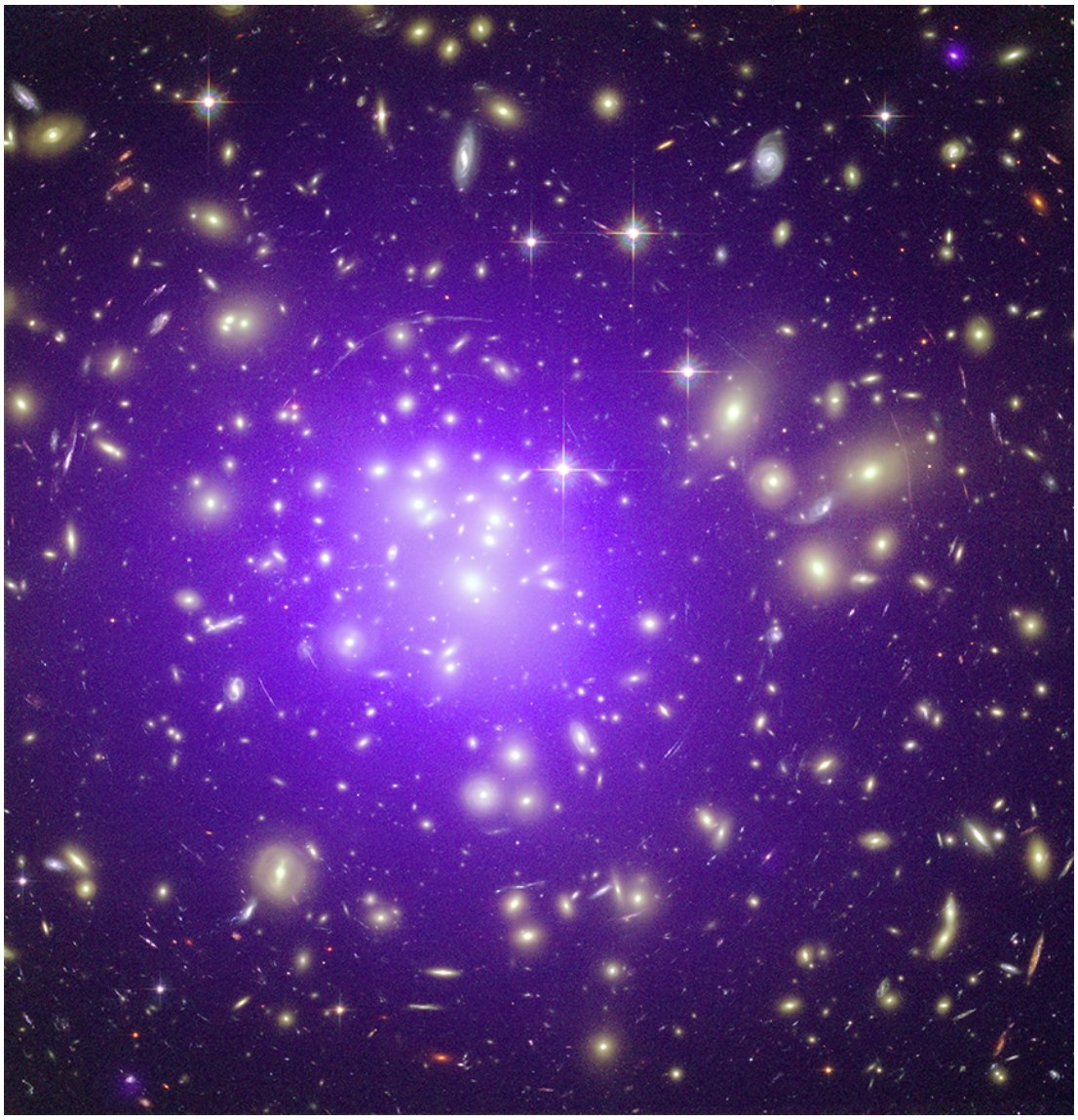

Figure 2.1: Galaxy cluster Abell 1689. Galaxy clusters produce a range of measurable signals and are often studied using a combination of radio, mm-wave, IR, optical, UV, and/or X-ray observations.Credits: HST/Chandra X-ray observatory.

Fig. 2.1 shows the image of a galaxy cluster Abell 1689 which is in constellation Virgo. The X-ray emission due to hot ICM is shown as purple in the image; galaxies from the optical data are coloured yellow. The long arcs in the optical image is caused by distortion due to strong gravitational lensing.

2.5.2 Cluster cosmology

Clusters have long provided crucial information about the cosmological model. Dark matter was discovered in Coma cluster in 1930s, when Fritz Zwicky observed that galaxies in cluster were moving too fast to be held by the gravitational pull of the visible galaxies (Zwicky, 1933). In the 1990s clusters provided evidence for low matter density universe (White et al., 1993).

Using the 'f_{gas}' test which is based on the fair sample hypothesis: since clusters are so large and have so deep gravitational potential wells their baryonic and dark matter content should be a fair sample of the Universe as a whole. In detail, this is not exactly fair; simulations place the depletion of baryons in clusters relative to the cosmic mean at ~10% within the virial radius. At smaller radii that present X-ray observations can reliably probe, the depletion is closer to 15- 20 per cent. Because the X-ray emissivity of the ICM depends on the square of the density (and weakly on the temperature) of the gas, X-ray observations can measure the gas mass very precisely. In dynamically relaxed systems, the assumption of hydrostatic equilibrium can also be used to determine the total mass, based on the gas temperature and density profiles. Hence, X-ray observations of dynamically relaxed systems can determine the gas mass fraction, $f_{gas} = M_{gas}/M_{tot}$. With a rudimentary estimate of the baryon depletion, measurements of the total mass, mass in stars, and mass in hot gas for a cluster, and an estimate of the cosmic mean baryon density based on big bang nucleosynthesis data, one can constrain the mean matter density in the Universe.

More recently, the community has been interested in using galaxy clusters to probe dark energy, neutrinos and cosmic growth of structure (Allen et al., 2011; Mantz et al., 2008, 2010, 2015; de Haan et al., 2016; Hasselfield et al., 2013; Planck Collaboration et al., 2016c; Bocquet et al., 2018; Rozo et al., 2010; Vikhlinin et al., 2009; Salvati et al., 2018; Zubeldia and Challinor, 2019).

Galaxy clusters are powerful probes of dark energy. The dark energy effects the evolution of universe in two different ways. First, it accelerates the expansion of the universe and thus slowing down the structure formation. Second, it affects the volume of the survey. Cluster number counts is sensitive to both of these effects: the abundance and the correlation function of galaxy clusters depend on the volume surveyed and rate of structure growth. Fig. 2.2 shows the cluster number count as a function of redshift for various dark energy equation of state

parameters, w, and for fixed dark energy density parameter, Ω_E. For fixed dark energy density, Ω_E, and less negative w implies less acceleration and thus higher velocity in the past. This results in few clusters at low redshift due to decreased volume surveyed and more clusters at high redshift due to decreased structure growth (Mohr et al., 2003).

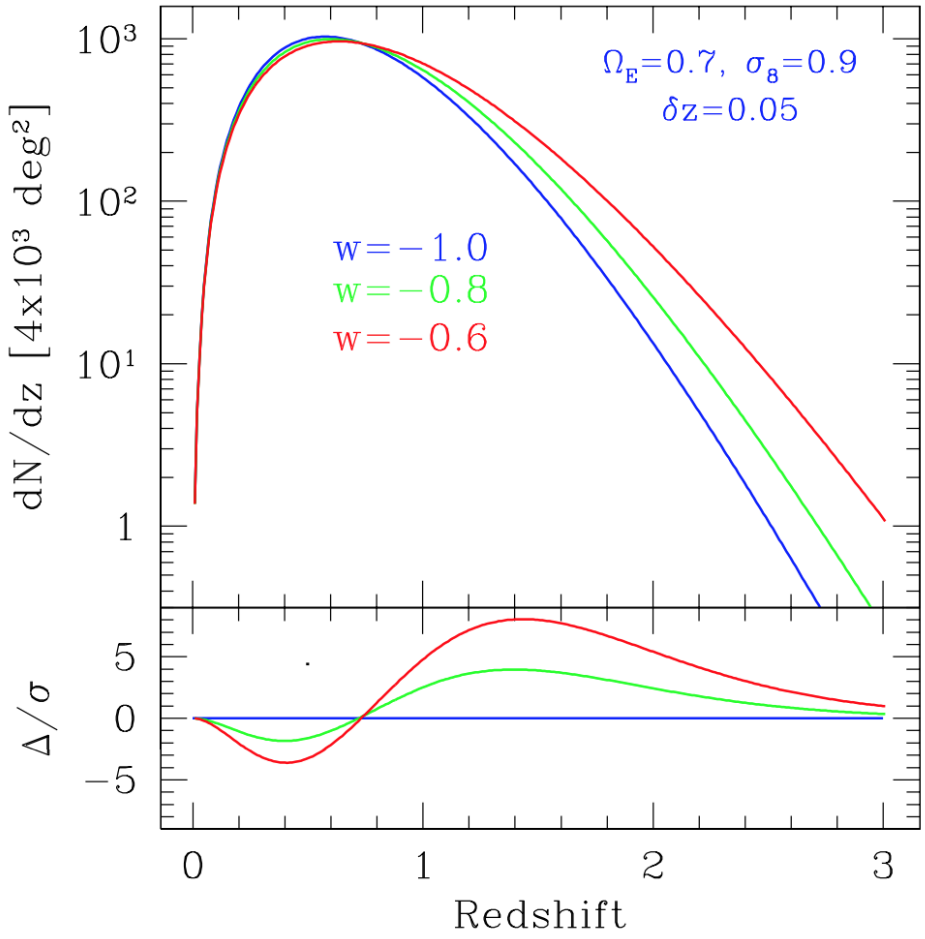

Figure 2.2: The cluster count redshift distribution for a simulated 4000 deg^2 survey. On the top panel three models with different dark energy equation of state parameters are shown and statistical differences are quantified in the bottom panel (Mohr et al., 2003).

As seen in §2.4.1, halo/cluster abundance as a function of mass is sensitive to cosmological parameter such as Ω_m and σ_8. Constraints obtained on Ω_m, σ_8, and dark energy equation of state parameter, w, is shown in Fig 2.3. As can be inferred from the plot, cluster constraints are complementary to that of CMB

anisotropies. For the above constraints, only 241 clusters from ROSAT all sky survey were used (Mantz et al., 2015). Given that ongoing and future surveys will detect tens to hundreds of thousands of galaxy clusters, clusters will become indispensable probes of cosmology (The Simons Observatory Collaboration et al., 2019; Bender et al., 2018; LSST Science Collaboration et al., 2009; Merloni et al., 2012; CMB-S4 Collaboration et al., 2016).

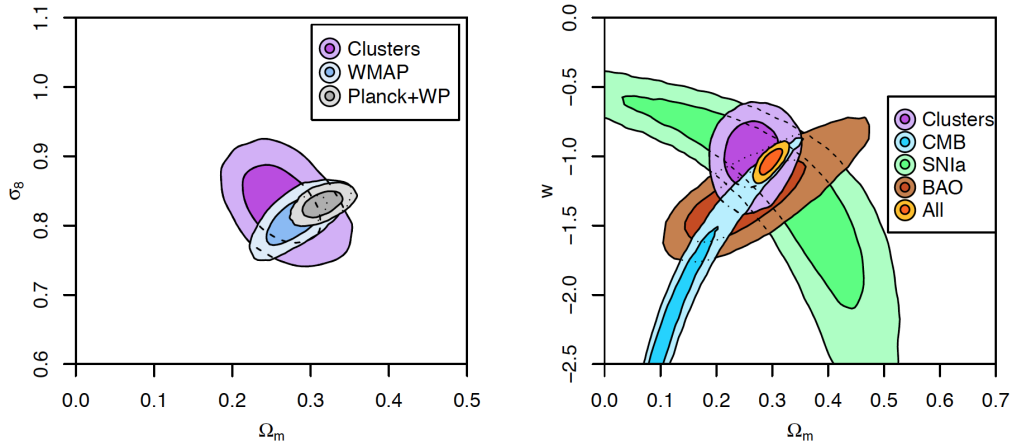

Figure 2.3: On the left is flat ΛCDM model: constraints on Ω_m and σ_8 from clusters in purple, from CMB observations in blue (*Planck*) and grey (*Planck* and WMAP). On the right we have flat wCDM: constraints on w and Ω_m for various cosmological probes. Cluster (purple) provide the tightest single-probe constraints (Mantz et al., 2015) (with standard prior on h and $\Omega_b h^2$).

2.5.3 Cluster cosmology is limited by mass estimation

While clusters are powerful probes of cosmology, the use of clusters for cosmology is currently limited by the accuracy of the mass estimation. Many ways to measure the cluster mass relate a cluster observable $'O'$ to the cluster mass through a parametric relation

$$O = AM^B f(z)^C \tag{2.31}$$

where A is the normalisation parameter, D is the intrinsic scatter, B and C are the mass and redshift evolution parameters respectively. The trouble is that these depend on complicated baryonic physics which is not well understood and any scatter in the estimated mass will affect the inferred constraints from cluster cosmology.

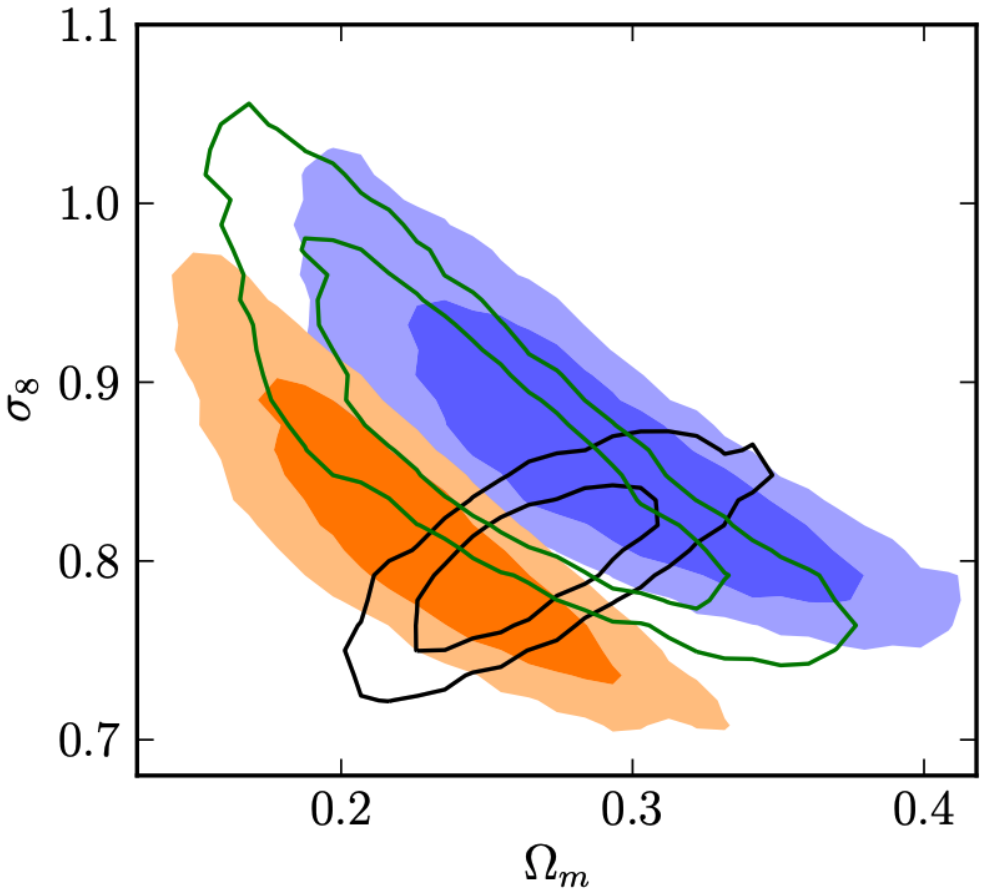

Figure 2.4: Effects of systematics in mass estimation on cluster cosmology. Constraints on matter fluctuation amplitude parameter (σ_8) and matter density parameter (Ω_m) from CMB data is shown in black contour. The coloured contours (orange, green, and blue) are the constraints obtained using cluster counts (excluding CMB information) for three different SZ-mass scaling relations. While constraint obtained by any one of the scaling relations would complement the information obtained from CMB, the results from three different scaling relations span the range of parameters allowed by CMB data.

Fig. 2.4 shows the systematic effects of cluster mass estimation on cosmological parameters Ω_m and σ_8. The black contour represents the cosmological constraints obtained using CMB. The green, blue, and orange contours represent constraints due to cluster number count for three different SZ-mass scaling relations. The three colored contours assume different cluster gas physics. The orange contour represents the Arnaud et al. (2010) profile. In the green contour the SZ-mass scaling relation is calibrated using Bode et al. (2012) simulations and the blue contour represents the calibration using Nonthermal20 models de-

scribed in Trac et al. (2011). While cluster number counts provide complementary constraints to that of CMB, however, any systematic in mass estimation will eventually lead to uncertainties in cosmological parameters (Hasselfield et al., 2013).

Accurate cluster mass estimates are essential to fully realise the potential of cluster cosmology. One of the ways to obtain robust cluster masses is through weak gravitational lensing (Becker and Kravtsov, 2010). Unlike the mass observable scaling relation, cluster mass estimation through gravitational lensing of a background source is independent of baryonic physics and directly probes the total mass distribution in the galaxy cluster. Lensing measurements provide a low-bias measurement of cluster mass that can be used to improve the accuracy of the mass-scaling relation 2.31. Below I provide brief formalism of gravitational lensing.

Gravitational lensing formalism:
In this section, I provide a very brief introduction of gravitational lensing formalism and strongly recommend the reader to refer (Bartelmann and Schneider, 2001) for a detailed review. According to General Relativity, a point mass M deflects the light ray with impact parameter b by an angle approximately equal to

$$\hat{\alpha} = \frac{4GM}{c^2 b} \tag{2.32}$$

where G is the gravitational constant, M is mass of the deflection source, and c is the speed of light.

Under linear approximation, the deflection due to a spatially extended mass can be written simply as a vector sum over point masses, which is given by

$$\vec{\hat{\alpha}}(\vec{\xi}) = \frac{4G}{c^2} \int d^2\xi' \int dz \rho(\vec{\xi}', z) \frac{\vec{b}}{|\vec{b}|^2} \tag{2.33}$$

where z is the line-of-sight coordinate, and $\vec{b} = \vec{\xi} - \vec{\xi}'$ is the vector impact parameter of the actual ray path from the infinitesimal mass $d^2\xi' dz \rho(\vec{\xi}', z)$ located at the coordinates $(\vec{\xi}', z)$.

In the case of thin lens where the distance between the source, lens, and the observer is much larger than the physical size of the lens, we can define the

projected mass density as

$$\Sigma(\vec{\xi}') = \int \rho(\vec{\xi}', z)dz \tag{2.34}$$

where $\vec{\xi}'$ is a vector in the plane of the sky. The deflection angle is then

$$\vec{\hat{\alpha}}(\vec{\xi}) = \frac{4G}{c^2} \int \frac{(\vec{\xi} - \vec{\xi}')\Sigma(\vec{\xi}')}{|\vec{\xi} - \vec{\xi}'|^2} d^2\xi' \tag{2.35}$$

In the schematic representation shown in Fig. 2.5 the difference between the unlensed angular position $\vec{\beta}$ and the observed position $\vec{\theta}$ is this deflection angle, reduced by a ratio of distances, described as the lens equation

$$\vec{\beta} = \vec{\theta} - \vec{\alpha}(\vec{\theta}) = \vec{\theta} - \frac{D_{ds}}{D_s}\vec{\hat{\alpha}}(\vec{D_d\theta}) \tag{2.36}$$

where D_{ds} is the distance from the lens to the source, D_s is the distance from the observer to the source, and D_d is the distance from the observer to the lens. For extragalactic lenses, these must be angular diameter distances.

In strong gravitational lensing, this equation can have multiple solutions, because a single source at $\vec{\beta}$ can be lensed into multiple images.

The reduced deflection angle $\vec{\alpha}(\vec{\theta})$ can be written as

$$\vec{\alpha}(\vec{\theta}) = \frac{1}{\pi} \int d^2\theta' \frac{(\vec{\theta} - \vec{\theta}')\kappa(\vec{\theta}')}{|\vec{\theta} - \vec{\theta}'|^2} \tag{2.37}$$

where we define the convergence

$$\kappa(\vec{\theta}) = \frac{\Sigma(D_d\vec{\theta})}{\Sigma_{cr}} \tag{2.38}$$

and the critical surface density (not to be confused with the critical density of the universe)

$$\Sigma_{cr} = \frac{c^2 D_s}{4\pi G D_{ds} D_d} \tag{2.39}$$

We can also define the deflection potential

$$\psi(\vec{\theta}) = \frac{1}{\pi} \int d^2\theta' \kappa(\vec{\theta}') \ln|\vec{\theta} - \vec{\theta}'| \tag{2.40}$$

such that the scaled deflection angle is just the gradient of the potential and the

convergence is half the Laplacian of the potential:

$$\vec{\beta} - \vec{\theta} = \vec{\alpha}(\vec{\theta}) = \vec{\nabla}\psi(\vec{\theta}) \tag{2.41}$$

$$\kappa(\vec{\theta}) = \frac{1}{2}\nabla^2\psi(\vec{\theta}) \tag{2.42}$$

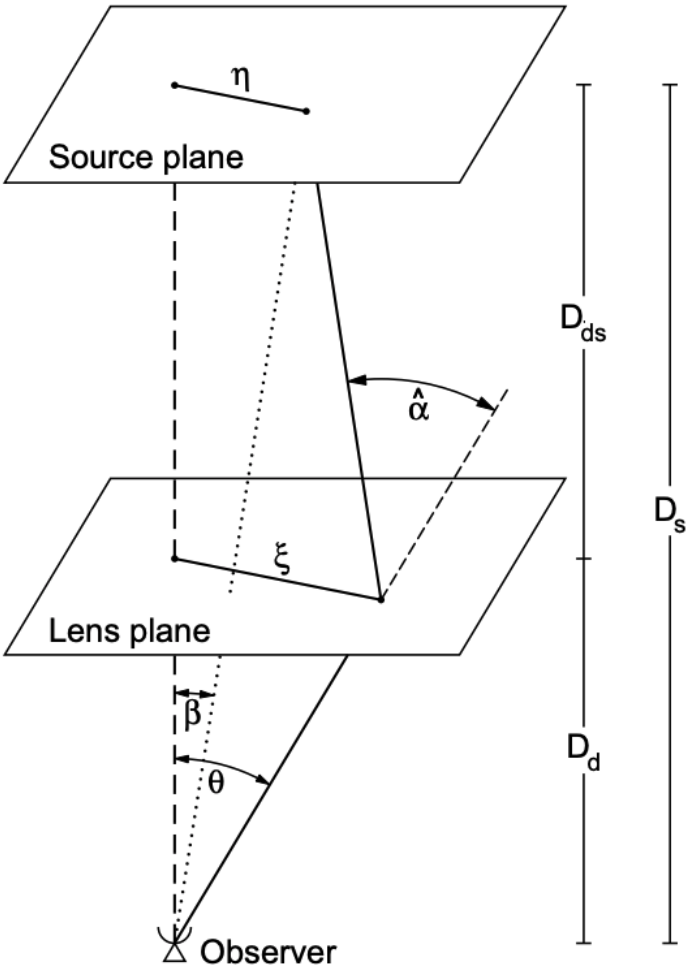

Fig. 11. Sketch of a typical gravitational lens system.

Figure 2.5

Source of Gravitational lensing:

The background source can either optical galaxies or CMB, with CMB having the following advantages over optical:

- CMB is at precise redshift of $z \approx 1100$
- CMB lensing signal remains uniform over with cluster redshift
- CMB has relatively less systematics
- the statistical properties of CMB are very studied and hence easy to model

The rest of the chapters focus on various methods we have developed to extract lensing signal from CMB data, the data used, and the results we have obtained.

Chapter 3

Maximum Likelihood Estimator

Overview

There are several methods in literature to extract cluster lensing signal from CMB data (Dodelson, 2004; Lewis and Challinor, 2006; Baxter et al., 2015; Hu et al., 2007; Melin and Bartlett, 2015; Yoo and Zaldarriaga, 2008; Horowitz et al., 2019; Raghunathan et al., 2017; Horowitz et al., 2019). I worked mainly on two methods during my thesis: the Maximum Likelihood Estimator (MLE) and Quadratic Estimator (QE). This chapter is organised as follows. In §3.1, I provide a brief overview of CMB-cluster lensing, followed by description of MLE in §3.2. The performance of MLE and QE is compared in §3.3 and several sources of systematics are quantified in §3.4. The forecasts for future surveys are provided in §3.5 and the conclusions in §3.6. This chapter closely follows Raghunathan et al. (2017).

3.1 CMB lensing overview

While passing through the intervening galaxy cluster, cosmic microwave background (CMB) photons are deflected due to the cluster's gravitational potential. The resulting distortion in the path of the CMB photons is called CMB-cluster lensing. The distortion pattern can be understood given what we know about the CMB and the cluster. Typically the angular size of galaxy cluster is of the order of a few arcminutes (at z>0.3). On these scales, CMB power is heavily suppressed due to diffusion damping (Silk, 1968). Thus the unlensed CMB can be approximated as a gradient. Gravitational lensing by a galaxy cluster induces a dipole structure on top of the background gradient with hot and clod spots swapped. As CMB is only polarised at the 10% level, the lensing signal in polarisation is an order of magnitude smaller than that in temperature.

Fig 3.1 shows the lensing signal for a cluster of mass $5 \times 10^{14}\ M_{\odot}$ at redshift of $z = 0.7$. In the left panels of Fig 3.1, we have the background CMB gradient for

the temperature and polarisation Stokes Q/U parameters, in the middle panel we have the corresponding lensed maps and in the right panel we have difference map which clearly shows the lensing dipole signatures.

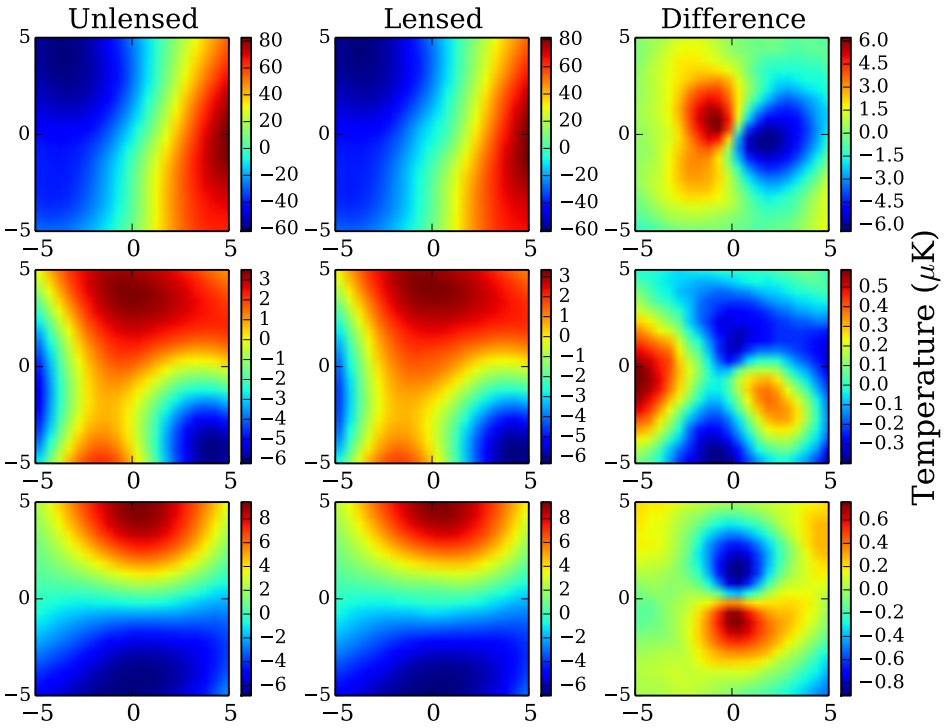

Figure 3.1: An illustration of the lensing effect on CMB due to a galaxy cluster of mass $5 \times 10^{14} M_{\odot}$ on a $10' \times 10'$ box centered around the cluster. The top panel shows the effect of cluster lensing on CMB temperature field. The bottom two panels are for the Stokes Q and U parameters. The amplitude of the lensing signal for temperature is a few μK and an order of magnitude smaller in polarisation. Note that these images have neither experimental noise nor foregrounds.

Gravitational lensing remaps the unlensed CMB temperature and polarisation fields by the gravitational deflection angle. Mathematically lensing can be expressed by the following equations

$$T(\hat{n}) = \widetilde{T}(\hat{n} + \vec{\alpha}(\hat{n})) \tag{3.1}$$

$$Q(\hat{n}) = \widetilde{Q}(\hat{n} + \vec{\alpha}(\hat{n})) \tag{3.2}$$

$$U(\hat{n}) = \widetilde{U}(\hat{n} + \vec{\alpha}(\hat{n})) \tag{3.3}$$

where~represents unlensed fields, T represents the temperature field, and Q and U are the Stokes polarisation parameters respectively. $\vec{\alpha}(\hat{n})$ is the deflection angle along the $\hat{n}$ direction.

Deflection angle:

The lensing induced deflection angles depend on the density profile of a galaxy cluster. Here we provide a detailed calculation of the deflection angle for a spherically symmetric Navarro-Frenk-White (NFW) density profile (Navarro et al., 1996). Lensing convergence, κ, is related to the deflection angle, $\vec{\alpha}$ as

$$\kappa = \frac{1}{2}\nabla.\vec{\alpha}. \tag{3.4}$$

For symmetric density profiles, the lensing convergence is equal to the ratio of surface mass density over the critical surface density of the Universe at the cluster redshift, $\kappa = \frac{\Sigma(x)}{\Sigma_{crit}}$. The surface mass density or the projected mass density of the halo is obtained by integrating the halo density profile along the line of sight.

$$\Sigma(x) = 2\int_0^\infty \rho(r)ds \tag{3.5}$$

where r is the radial distance, x is the corresponding two-dimensional planar distance and s is distance along the line of sight with $s = 0$ being the plane of the cluster. The critical surface density of the Universe at cluster redshift is given by

$$\Sigma_{crit} = \frac{c^2}{4\pi G}\frac{D_{cmb}}{D_{clus}D_{cmb,clus}} \tag{3.6}$$

where D_{cmb} is the comoving distance to the epoch of recombination ($z = 1100$), D_{clus} is the comoving distance to the cluster, $D_{cmb,clus}$ is the comoving distance between the CMB and the cluster, and c is the speed of light.

Unless otherwise mentioned, we define all the cluster quantities in this thesis with respect to R_{200}, which is defined as the radius within which the mean cluster density is 200 times the critical surface density of the Universe at cluster redshift $\rho_{crit}(z)$. By definition M_{200} is given by

$$M_{200} = \int_0^{R_{200}} 4\pi r^2\rho(r)dr, \tag{3.7}$$

M_{200} can also be written as

$$M_{200} = \frac{800\pi}{3} R_{200}^3 \rho_{crit}. \tag{3.8}$$

The above mathematical equations hold for any spherically symmetric halo. Here we consider a specific case of Navarro Frenk White (NFW) halo density profile. In the NFW profile, the density of the dark matter halo as a function of radius is given by:

$$\rho(r) = \frac{\delta_c \rho_{crit}(z)}{(\frac{r}{R_s})(1+\frac{r}{R_s})^2} \tag{3.9}$$

where δ_c is the characteristic over-density and R_s is the characteristic scale radius. The dimensionless over-density is given by $\delta_c = \rho_0/\rho_{crit}(z)$, where ρ_0 is the cluster central density and $\rho_{crit}(z)$ is the critical density of the universe at cluster redshift. Plugging the above equation in 3.5, we can get the surface density for the NFW halo. By changing the variables of integration to $s = \sqrt{r^2 - x^2}$ and $ds = \frac{rdr}{\sqrt{r^2-x^2}}$ we obtain:

$$\Sigma(x) = 2\delta_c \rho_{crit}(z) R_s^3 \int_x^\infty \frac{1}{r(R_s+r)^2} \frac{rdr}{\sqrt{r^2-x^2}} \tag{3.10}$$

The scale radius is related to the dimensionless concentration parameter, c, as follows:

$$c = \frac{R_{200}}{R_s}, \tag{3.11}$$

we have set $c = 3.0$ following Bhattacharya et al. (2013).

Eqn.3.10 can be solved analytically and the explicit closed-form expression for the NFW case is given by Bartelmann (1996). With $\Sigma(x)$ and Σ_{crit} in hand we can use Eq. 3.4 to get the lensing deflection angle as function of cluster mass and redshift. Unless otherwise mentioned we assume the galaxy clusters follow the NFW profile. However, the mathematical framework described above can be applied to any halo density profile.

3.2 Maximum Likelihood Estimator

We developed a maximum likelihood estimator to constrain the CMB cluster lensing signal. The unlensed CMB is a Gaussian random field to a very good approximation (Planck Collaboration et al., 2014b). CMB-cluster cluster lensing remaps this Gaussian random field based on the deflection angle. The remapping leads to a non-zero covariance between different map pixels that had formerly

been independent. First, we describe the likelihood estimation in §3.2, followed by covariance matrix calculation in §3.2.1.

Likelihood Estimation

The likelihood of observing a particular map, d, is given by

$$-2\ln L(d|\Sigma_{lens}) = \ln|\Sigma_{lens}| + d^T\Sigma_{lens}^{-1}d, \tag{3.12}$$

where Σ_{lens} is the covariance matrix which acts as a model, d is the map vector of pixel values for temperature or polarisation.

The lensing signal of a single cluster is too weak compared to the intrinsic variations in CMB. For example, the lensing signal of a massive galaxy cluster $M_{200m} = 5\times10^{14}M_\odot$ at redshift $z = 0.7$ is of the order of 5 μK, whereas the background gradient is an order of magnitude greater ($50\mu K$). So we stack many clusters to increase signal to noise ratio (SNR) to a reasonable level

$$-2\ln L(d|\Sigma_{lens})_{tot} = \Sigma_{i=0}^{n} w_i[\ln|\Sigma_{lens}| + d_i^T\Sigma_{lens}^{-1}d_i] \tag{3.13}$$

where n is the total number of clusters in the sample, w_i is the weight assigned to the i^{th} cluster. Here we assign equal weights to all clusters ($w_i = 1$) as we are using simulations and it is not the case while using real data.

3.2.1 Covariance matrix calculation

We calculate the covariance matrix using a set of simulated skies [1]. To simulated the lensed CMB sky, we first generate the large-scale structure lensed CMB power spectra ($C_l^{TT}, C_l^{TE}, C_l^{EE}$, and C_l^{BB}) from CAMB for the *Planck* cosmology (Planck Collaboration et al., 2016b). We generate Gaussian random realisations of these power spectra on a $50'\times50'$ box at $0.25'$ resolution. The generated E and B maps are converted to Q and U maps using:

$$E_l \pm iB_l = -\int d^2\hat{n}\, e^{-i\hat{n}.l}\,[Q\pm iU](\hat{n})\, e^{\mp2i\phi_l} \tag{3.14}$$

where ϕ_l is the angle of l as measured from stokes Q axis (Leistedt et al., 2017).

These Gaussian realizations are then lensed by the deflection field (which is obtained as explained in 3.1). We use the central $10'\times10'$ to calculate the

[1] more details about simulations are provided in Appendix A.1

covariance matrix.[2] The lensing signal is of the order of few arcminutes even for a massive cluster and most of the lensing signal is within a radial distance of $10'$ from the cluster center. For a cluster of mass $M_{200m} = 2 \times 10^{14} M_{\odot}$ at redshift $z = 0.7$, increasing the boxsize to $14' \times 14'$ increases the SNR by $\leq 1\%$, while increasing the computational complexity several fold.

With simulated lensed CMB maps in hand, we calculate the covariance matrix as follows

$$\Sigma_{lens}(M, z) = \left\langle (\mathbf{G} - \langle \mathbf{G} \rangle)(\mathbf{G} - \langle \mathbf{G} \rangle)^T \right\rangle \quad (3.15)$$

$$= \frac{1}{n-1} \sum_{i=0}^{n} (\mathbf{G}_i - \langle \mathbf{G} \rangle)(\mathbf{G}_i - \langle \mathbf{G} \rangle)^T \quad (3.16)$$

where the vector G_i is either the polarisation or temperature simulated data for the i^{th} sky realisation and $\langle\rangle$ represents the ensemble average. The number of simulated skies depend on the number of degrees of freedom in the covariance matrix. In our case, the maximum number of degrees of freedom is for the polarisation estimator (concatenated Q/U or E/B maps), for which the covariance matrix is an 800×800 matrix. The number of simulations should scale with the number of elements in the covariance matrix. We find that 130,000 simulations are sufficient to recover cluster masses without any detectable bias. We then multiply the covariance matrix with Hartlap correction term $\frac{(n_{sims} - n_d - 1)}{n_{sims}}$, where n_{sims} is 130,000 and n_d is the length of the data vector 400(800) for T(QU), to remove any possible bias in Σ^{-1}_{lens} due to the finite number of simulations (Hartlap et al., 2007).

We also use these simulated skies to quantify the effects of statistical and systematic uncertainties. There are several astrophysical sources which act as a systematic bias for the CMB-cluster lensing analysis. In this work we consider clusters own SZ effects such as thermal Sunayev-Zel'dovich (tSZ) and kinematic Sunayev-Zel'dovich effects. Along with these SZ effects, we have also considered sources which are uncorrelated with cluster, such as tSZ effect from other halos, dusty star forming galaxies (DSFGs), and radio galaxies. In appendix, we provide more details about the addition of these foregrounds to simulated skies.

Here we have used simulations to check the performance of MLE and also to quantify the effect of systematics. Unless otherwise mentioned all the clusters are

[2]The lensing maps are generated on $50' \times 50'$ to take into account the large scale gradient, however, the lensing signal is concentrated in the center.

simulated at a mass of $M_{200} = 2 * 10^{14} M_{\odot}$ and at redshift of 0.7. For covariance matrix calculation we simulate the clusters at redshift of 0.7 with mass resolution of $2 * 10^{12} M_{\odot}$ Note that such fine gridding might not be computationally feasible for data where the clusters span a wide range of masses and redshifts. An optimal solution would be to generate the covariance matrices on coarser grid of mass and redshift and then interpolating it on a finer grid.

3.3 Results

In this section, we first validate our pipeline using simulations and we report the expected mass uncertainties for the polarisation and temperature MLE. Then we compare the performance of MLE and QE for ideal simulations by varying only the experimental noise levels and not including any galactic or extra galactic foregrounds. Later, we compare the performance of the estimators in the presence of foregrounds. In this chapter all the results are for a set of 100,000 simulated clusters (expected number of clusters for CMB-S4) each at a mass of $2 \times 10^{14} M_{\odot}$ and at redshift of 0.7.

3.3.1 Idealised simulations

Our baseline simulations include only experimental white noise level. These idealised simulations serve two purposes:

- serve as benchmark to estimate the effect of different systematic and statistical sources of uncertainties on lensing analysis.
- in addition to that, it provides equivalent conditions to allow for a fair comparison between MLE and QE.

To validate the pipeline we simulate 100,000 galaxy clusters each at a mass of $2 \times 10^{14} M\odot$ and at redshift of $z = 0.7$. These simulations convolved by a beam of FWHM $1'$ we then add a white noise realisation of rms $1\mu K$-arcmin for temperature maps and rms $\sqrt{2}\mu K$-arcmin to polarisation maps. The results are shown in the top panel of Fig. 3.2, the black solid line represents the combined likelihood for temperature MLE estimator and solid (dashed) orange curve is that for the polarisation QU (EB) estimator.We calculate the detection significance as mentioned above and measured a lensing significance of 400σ and 110σ for temperature and polarisation MLE respectively. Null test results are shown in the bottom panel of Fig. 3.2, for which we turned off lensing in our pipeline. As

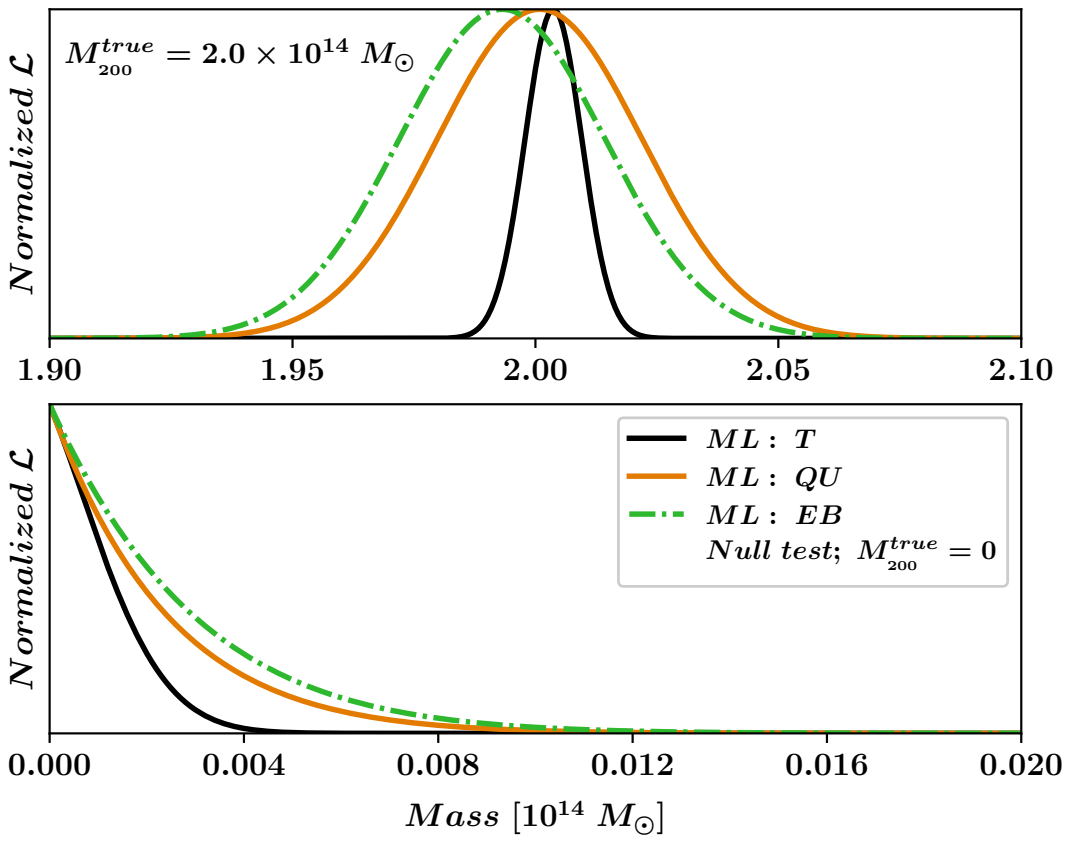

Figure 3.2: In the top panel we show the combined likelihood of 100,000 clusters each at redshift of 0.7 and at mass of $2\times10^{14}M_\odot$ for temperature and polarisation MLE estimators. The difference between QU and EB estimator isn't statistically significant. In the bottom panel we show the results of null test and as expected the likelihood peaks at zero for all three estimators

expected likelihoods for all the three MLE estimators (T, QU, and EB) peak at zero mass.

In the left panel of Fig.3.3, we compare the performances of the three MLE estimators and the temperature QE estimator as a function of experimental noise levels. It is evident from the Fig.3.3 that in the absence of foregrounds, temperature estimator outperforms polarisation above noise-level of 0.075 μK-arcmin. So even for future experiments temperature estimator has to be the primary channel from pure SNR perspective. Only below the noise-level of 0.075 μK-arcmin do polarisation estimator begin to be competitive with temperature. The relative performance of the temperature and the polarisation estimators can be understood as:

- lensing signal scales the amplitude of the background gradient which is ~10× brighter in temperature, but

- as the experimental noise levels drop, the background CMB acts as an additional source of noise for the temperature estimator.

The Orange squares and green circles in Fig. 3.3 represent MLEs using polarisation QU and EB maps respectively. As expected from theoretical standpoint there is no significant difference between their performance. The small difference at higher experimental noise levels is not statistically significant. However, using the QU maps simplifies the analysis as these modes are directly measured by the experiment and doesn't require a coordinate transformation.

Lastly, we compare the performance of the temperature MLE (solid black triangles) and QE (orange solid squares) in Fig. 3.3. The QE is a first order approximation of MLE (as we will see in next chapter 4). At higher noise levels (low SNRs) the effect of higher order terms is negligible resulting in no difference between the performance of MLE and QE estimators. However, at low noise levels (high SNRs) the MLE outperforms the QE. We find that the MLE's performance improves over that of the QE by a factor of 2 at a noise level of 0.1 μK-arcmin for our fiducial cluster sample. The performance of QE can be improved by using an iterative version as shown by Yoo and Zaldarriaga (2008).

Both the MLE and QE share a common difficulty in that they requrire a knowledge of cluster density profile. This dependence shows up in different places in each estimator:

- In the MLE, as explained in 3.2, we fit the lensed CMB pixel covariance templates to the observed data pixel covariance. The lensed CMB pixel covariance templates depend on the assumed cluster density profile.

- The QE works by exploiting the correlation between the background CMB gradient and lensing dipole to obtain lensing convergence profile. We fit models to these lensing convergence profile to extract the mass of the cluster.

While the MLE outperforms the QE at low experimental noise levels, the QE can be more easily modified to make it robust to the major foreground in lensing analysis as we will see in the next chapter.

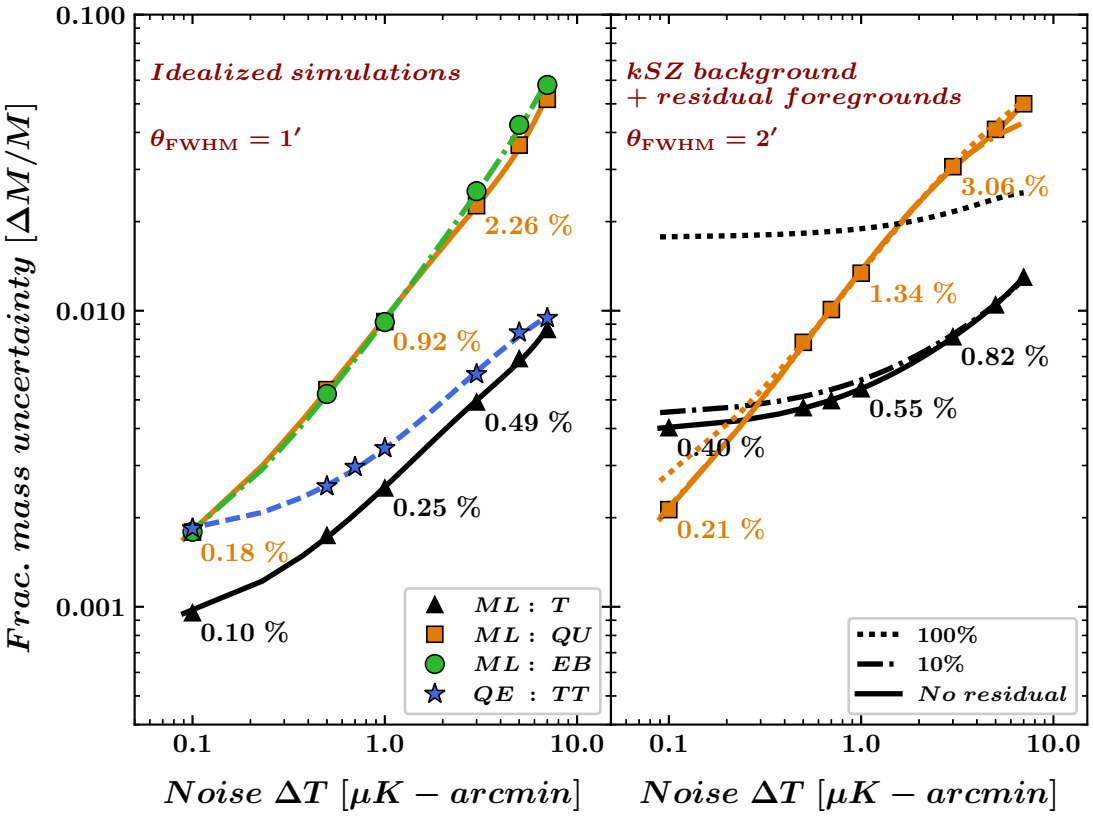

Figure 3.3: In the left hand panel, we show the performance of the MLE and QE for idealised simulations (no foregrounds) as function of experimental noise levels. In the right panel, we consider the effects of various foregrounds on the estimators. All the curves are for a set of 100,000 clusters each at mass of $2 \times 10^{14} M_{\odot}$ and at redshift of 0.7.

3.3.2 *Effects of extragalactic foregrounds on lensing analysis*

In this section, we look into the effects of extragalactic foregrounds on CMB-cluster lensing analysis. While galactic foregrounds also affect the CMB-cluster lensing analysis, we can exploit their frequency dependence to suppress galactic contamination. Here we consider the effect of extra galactic foregrounds on the final mass uncertainties. Some of these foregrounds such as cluster's own SZ effect, will also bias the analysis these biases will be explored in the next section. The level of foregrounds relative to the CMB is much higher in temperature than in polarisation channel, thus the effect of foregrounds is higher in temperature estimator than polarisation. We consider the impact of tSZ, kSZ, radio galaxies

and dusty galaxies on lensing analysis.

The impact of foregrounds on the fractional mass uncertainty of lensing estimators as function of experimental noise level can be seen by comparing the left and right panels in Fig. 3.3. As expected foregrounds have negligible effects on the polarisation channel (orange squares) due to their low level of polarisation. For the temperature estimator, the extragalactic foregrounds (tSZ effect, kSZ effect, radio galaxies, and dusty galaxies) set an effective noise level of $\sim 5\mu K$-arcmin if not cleaned, this results in plateauing at 1.8% in mass uncertainty (black dotted line). Without any foreground cleaning polarisation QU estimator outperforms the temperature channel at 1.5 μK-arcmin noise level. However, we can exploit the frequency dependence of various extragalactic foregrounds to reduce their effect. While combining multiple frequency channels we assume that the beam size is $1'$ FWHM Gaussian irrespective of the frequency channel to simplify the analysis [3]. Using different spectral dependence of background CMB and tSZ we can completely eliminate the tSZ power. While tSZ can be eliminated, kSZ has the same spectral dependence as that of the CMB and cannot be eliminated using linear combination of different frequency channels.

Furthermore we assume that the frequency cleaning will behind some radio and dusty galaxy power [4]. The black solid line in Fig. 3.3 correspond to 100% removal of radio and dusty galaxy power. The dot-dashed (dashed) line corresponds to 90% (0%) removal of radio and dusty galaxy power. With 90% cleaning of foreground (dashed black curve), temperature estimator becomes the main channel for estimating lensing signal even for future surveys (CMB-S4 Collaboration et al., 2016). There is only a fractional improvement in the performance above 90% of cleaning. The foreground cleaning using Internal Linear Combination technique results in an effective resolution equal to that of the lowest frequency channel. It is important to note here that the enlargement of beam due to foreground cleaning if taken into account will further degrade the mass uncertainties.

To summarize, the extragalactic foregrounds have almost no effect on the performance of polarisation estimators. On the other hand, temperature estimators will have effective noise floor of $5\mu K$-arcmin if the foregrounds aren't taken into account.

[3] this may not be a very good assumption, but here we just want to build an intuition for future surveys.

[4] note that in all the curves we have assumed 100% kSZ power and 0% tSZ power

3.4 Systematic bias checks

From Fig 3.3, it is evident that we will achieve unprecedented statistical uncertainties for future low noise surveys. However, in order to fully utilise this statistical power, we need to account for all the systematic biases involved in lensing analysis. In this section, we quantify various sources of systematics that could bias our final results. We examine the following sources:

- cluster center - for example, typical offset between SZ and X-ray centroid or the location of brightest central galaxy is 0.5 $'$ (Saro et al., 2015; Song et al., 2012)
- cluster density profile - the assumed NFW profile may not match the true density profile
- lensing by other halos - in addition to the galaxy cluster CMB is also lensed by other halos along the line of sight
- redshift - misestimation of cluster redshit
- cluster's tSZ effect
- cluster's kSZ effect
- dusty galaxies

The last three sources have negligible effect on the polarisation estimators as they are partially polarised. Note that all these sources may effect polarisation and temperature estimators to different extents as the angular scales are weighed differently in both estimators.

The baseline simulations for bias calculations include $1'$ FWHM Gaussian beam, experimental noise level of $1\mu K$-arcmin in temperature (which corresponds to a noise level of $\sqrt{2}\mu K$-arcmin in polarisation) and no foregrounds unless otherwise stated. While the precise amount of bias depends on experimental beam size, noise-level, and foregrounds as they define the weighing of different angular scales of MLE, here we roughly quantify the magnitude of bias and give a direction to pursue future work in CMB-cluster lensing to reduce the systematic uncertainties. We report the systematic bias for a sample of 1,000,000 clusters

each with a mass of $2\times10^{14}M_{\odot}$ and redshift of 0.7 (except for redshift uncertainty case). The bias is calculated as follows:

$$b = \frac{M_{bias}}{M_{true}} - 1. \tag{3.17}$$

where M_{bias} is the final recovered mass when the bias source is included in the lensing analysis and M_{true} is the input mass. Error on the bias is obtained by calculating the scatter in 100 subsamples.

We report bias for all the sources considered in Table 3.1. Other than errors in redshift, all other sources of bias should be considered carefully to achieve sub-percent uncertainty as claimed for future CMB surveys (CMB-S4 Collaboration et al., 2016).

Bias source	Bias % at ΔT = 1.0 μK – arcmin			
	Temperature $T_{\rm ML}$		Polarization $QU_{\rm ML}$	
	% bias	error	% bias	error
tSZ cleaning (1% residual signal)	-6.3	0.50	0	-
kSZ fitting (20% uncertainty)	-7.3	0.31	0	-
DG in the cluster	-4.5	1.70	-1.3	1.20
Redshift uncertainty	0.2	0.25	-0.3	0.90
Cluster positions	-7.5		-1.5	
Presence of undetectable haloes	2.5	0.25	6.3	0.92
Uncertainties in cluster mass profile				
$\kappa_{\rm NFW} + \kappa_{sub}$	3.1	0.25	-0.6	0.92
$\kappa_{Einasto}$	-2.4		-2.5	
$\kappa_{\rm NFW}^{mod}$	2.2		0.6	

Table 3.1: The percentage mass biases from various systematic uncertainties. A positive (negative) number means the recovered mass is over- (under-)estimated. The first three lines reflect the expected biases from astrophysical foregrounds; these are serious for the temperature estimator, but not the polarization estimator. The next two lines deal with uncertainties in where the cluster is located (whether in redshift or on the sky); these are likely to be manageable for both estimators. The last four lines relate to uncertainties in how the mass is distributed, whether due to projection effects from nearby, lower-mass haloes, or due to uncertainties in the average mass profile for galaxy clusters. These questions about the mass distribution are a concern for both temperature and polarization. Note that here we have considered only dusty galaxies in the cluster (tSZ X CIB correlation) and not the field galaxies.

3.4.1 Halos along the line of sight

In addition to galaxy cluster, the lensing signal also depends on other halos present along the line of sight as well as the correlated halos. If the effect due to these halos isn't taken into account then the final results will be biased high. This is particularly a major concern for low mass haloes as they won't be detected by the survey. To quantify the effect of this bias we use Flender et al. (2016) simulations. The Flender et al. (2016) simulation is an N-body cosmological simulation with 17 million objects. For each cluster we randomly select a halo within a mass range of $M_{200} \in [1.8, 2.2]\ 10^{14} M_{\odot}$ and redshift range of [0.6,0.8]. We simulate the CMB maps as explained earlier, however, instead of lensing the CMB with just the cluster convergence profile we lens it with all the convergence profiles which are within the $50'$ from the cluster center. This includes correlated halos. Analysis proceeds normally after this - these lensed CMB maps are convolved by Gaussian beam after which specified white experimental noise is added. As expected both polarisation and temperature estimators are biased high : 2.5 ± 0.3% for temperature MLE and 6.3 ± 1.1% for polarisation QU estimator. We can reduce the bias by taking two halo term into account, however, that will include more nuisance parameters increasing the statistical uncertainty of the final results.

Along with the correlated halos and halos along the line of sight, large scale filaments also bias the lensing analysis which is not considered here. Galaxy clusters are not isolated objects, they are generally found in large scale filaments. Also, clusters with ellipticity along the line of sight have higher tSZ increasing the probability of their detection in tSZ surveys. The scope of finding the bias due to the large filaments and selection function is outside the scope of this thesis. Its worth noting that in order to fully realise the potential of future surveys in obtaining sub-percent mass uncertainties, we need to work bias due to large scale filaments and cluster ellipticity. Accurate and reliable simulations of structure formation on large volumes are needed in order to handle this source of systematic error at the sub-percent level.

3.4.2 Cluster mass profiles

As mentioned the lensing estimators assume a density profile which will certainly differ from the true cluster profile. Any difference between the assumed mass profile and true cluster profile will bias the final results. In this work we assume

the clusters to follow an NFW profile. However, studies have shown that for massive clusters the density profile deviates significantly from NFW at radius $r \geq 0.5 \times R_{200}$ (Diemer and Kravtsov, 2014). It is unknown whether these deviations will be larger or smaller for lower mass clusters. Also a recent study has shown that for analysis involving stacked halos Einasto profile (Einasto and Haud, 1989) provides a better estimate (Child et al., 2018). Here we consider three density profiles in order to estimate the bias.

- A modified version of the NFW profile which drops off more rapidly with radius

$$\kappa^{mod}_{\rm NFW}(x) = \begin{cases} \kappa_{\rm NFW} & ; x \leq 0.75\theta_{200} \\ \kappa_{\rm NFW} \times m(i,j) & ; 0.75\theta_{200} < x \leq 1.5\theta_{200} \\ 0 & ; otherwise \end{cases} \tag{3.18}$$

  where $m(i,j)$ is a Hanning two-dimensional (2D) apodization kernel. We create the 2D apodization kernel as $m(i,j) = m(i) \times m(j)$ with $m(i) = \frac{1}{2}\left[1 - cos\left(\frac{2\pi(i-n/2)}{n}\right)\right]$, where i and j are pixel indices in the $n \times n$ map.

- A change to the cuspiness of cluster core in the NFW profile following King and Schneider (2001)

$$\kappa^{sub}_{\rm NFW}(x) \;=\; \begin{cases} \kappa_{\rm NFW} \; + \sum_{i=1}^{3} \kappa^{i}_{sub} & ; x \leq 1' \\ \kappa_{\rm NFW} & ; otherwise; \end{cases} \tag{3.19}$$

  where κ_{sub} is the convergence due to substructure.

- The Einasto profile (Einasto and Haud, 1989)

$$\rho(r)_{Ein} \;=\; \rho_0 \; exp\left(-\frac{2}{\alpha}\left[\left(\frac{r}{R_s}\right)^{\alpha} - 1\right]\right) \tag{3.20}$$

  with the shape parameter $\alpha = 0.18$ (Ludlow et al., 2013). The Einasto convergence profile is obtained by inserting this into Eq.(3.5).

In each of the three cases we lens CMB by the assumed cluster profile, however, we use NFW profile to calculate our model. Assuming the wrong cluster profile biases the results from -2.5% to 3.8% as shown in Table 3.1. A similar study

was done on optical weak-lensing analysis by Sereno et al. (2016) who used NFW profile in the model and Einasto profile in the simulated data; Sereno et al. (2016) found a bias of -2 to 7 % depending on the cluster mass. This level of bias is larger than the statistical mass uncertainties expected for the proposed future experiment (CMB-S4 Collaboration et al., 2016), and a significant challenge for upcoming experiments. More work will be required to accurately measure the cluster mass profiles as a function of radius if we are to achieve the full potential of galaxy cluster cosmology.

3.4.3 Cluster miscentering

Any difference between the true cluster center and the model will result in a bias. Misestimation of the cluster center even by a small amount results in underestimation of cluster mass as we lose some of the lensing signal. To quantify the effect of miscentering, we draw an offset from a normal distribution N(0, σ^2) and lens the CMB with offseted clusters to obtain simulated data, however, model doesn't take the offset into account. Fig. 3.4 shows the bias in the final results as a function of offset for both temperature (orange squares) and polaristion estimators (black triangles). As expected the bias increases with the rms offset, 'σ'. The bias in temperature estimator is smaller than polarisation is because the temperature estimator draws more information from smaller angular scales than the polarisation estimator. Note that here we haven't considered foregrounds, considering foregrounds would decrease the weight of smaller angular scales. For survey with higher experimental noise, larger beams and foregrounds the bias due to miscentering will be smaller.

The typical offset between the SZ-centroid and the X-ray or brightest central galaxy (BCG) is of the order of $0.5'$ (von der Linden et al., 2014; Song et al., 2012; Saro et al., 2015). For $0.5'$ offset the mass is underestimated by 7.5 ± 0.3% for temperature estimator and 1.5 ± 1.3 % for polarisation estimator. For a given constraint on the offset, a correction could be easily applied to eliminate the bias, however, that will result in a slight decrease of SNR. Neglecting the foreground power, one would need to know the rms offset σ by 2% (8%) in order to achieve sub-percent uncertainty for the temperature (polarisation) MLE. However, adding foregrounds will reduce the weight of the information from smaller angular scales and lessen the requirement of how well the positional uncertainty must be known.

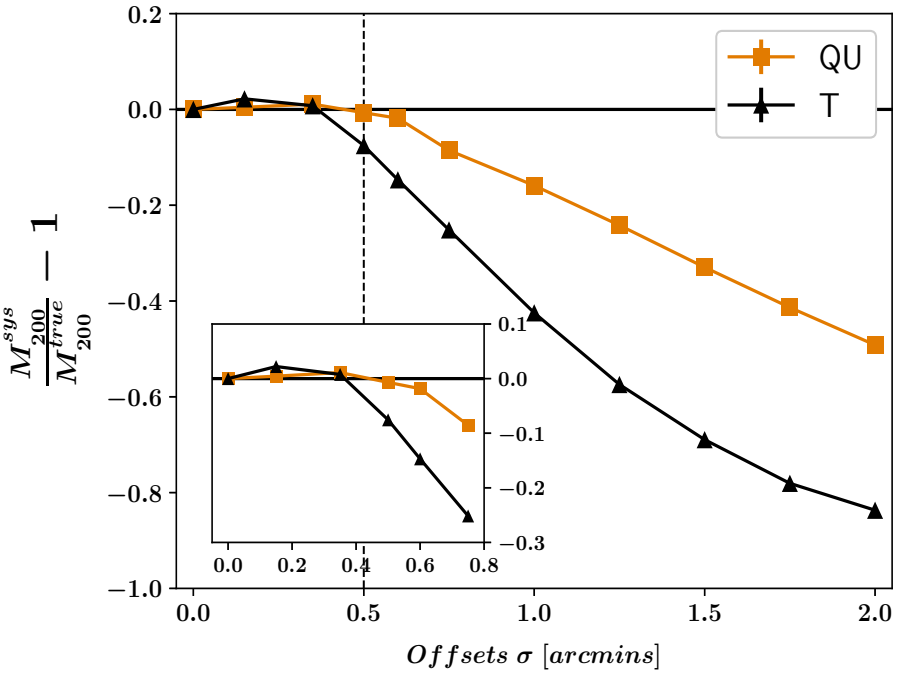

Figure 3.4: The positional offset between the assumed and true cluster centroid will bias the estimate low for $T_{\rm ML}$ (black triangles) and $QU_{\rm ML}$ (orange squares) estimators. The typical positional offset of $0.5'$ (von der Linden et al., 2014; Song et al., 2012; Sereno et al., 2016) is marked with the vertical dashed line. The error bars are derived using estimates gathered by repeating the test 100 times.

3.4.4 Bias due to redshift uncertainty

Upcoming surveys such as (Benson et al., 2014; The Simons Observatory Collaboration et al., 2019; CMB-S4 Collaboration et al., 2016) are expected to return tens to hundreds of thousands of clusters. At these numbers obtaining spectroscopic redshift for each cluster will be infeasible. Instead we likely rely on red sequence redshifts up to a redshift ~ 1.5 and lower limits on the redshift for clusters at even higher redshifts. The current state of the art for red sequence redshifts can be seen in the DES `redMaPPer` catalog, where the *photo-z* errors are $\sigma_z = 0.01(1+z)$ for $z \leq 0.7$ and $\sigma_z = 0.02(1+z)$ for $z \sim 0.9$ (Rykoff et al., 2016). We examined the effect of the expected redshift uncertainty by considering a redshift scatter for individual clusters. We conservatively take the redshift errors to be

$$\sigma_z = \begin{cases} 0.02(1+z); & z < 1 \\ 0.06(1+z); & z > 1 \end{cases}$$

We create mock lensed CMB maps for four sets of redshifts redshifts $z \in [0.5, 1, 1.5, 2]$. While constructing the pixel-pixel covariance matrix we use the 'measured' redshift, $z + \sigma_z$, for each cluster. The resulting bias is listed in Table 3.1. We do not detect a mass bias at any redshift.

3.4.5 Bias due to the kinematic SZ signal

CMB photons get doppler shifted due to the relative motion of the galaxy cluster with respect to the CMB rest frame, this is known as kinematic Sunyaev-Zel'dovich effect (kSZ) (Sunyaev and Zel'dovich, 1972). While the kSZ effect is an order magnitude smaller than the tSZ, unlike tSZ effect, the kSZ effect has the same spectral dependence as that of CMB. We cannot combine multiple frequency channels to eliminate the kSZ effect. However, we can use polarisation information as the kSZ effect is largely unpolarised (Sazonov and Sunyaev, 1999).

To quantify the kSZ bias on the temperature estimators we consider the publicly available kSZ maps and halo catalog from Flender et al. (2016) simulations. These are full sky simulations in the healpix (Górski et al., 2005) pixelisation scheme with nside of 8192 correpsponding to 0.42 arcminute resolution. Within the mass range of $M_{200} \in [1.8\times10^{14}, 2.2\times10^{14}]$ $M_\odot$ and $z \in$ [0.6,0.8] the catalog has 20,000 halos. For each cluster in the simulated data we randomly pick clusters from this set of 20,000 halos. For each cluster we take a $50' \times 50'$ cutout centered around the halo, smooth it with experimental Gaussian beam of FWHM = $1'$ and add it to the lensed cluster cutout.

Final results are significantly biased low at 41% level if the kSZ effect is not taken into account while modeling the pixel-pixel covariance matrix. We get similarly large levels of bias when we use an analytical model for the cluster kSZ signal instead of extracting them from N-body simulations. Modelling the optical depth of the clusters using the Battaglia (2016) profile and drawing the cluster velocities from a normal distribution $N(0, \sigma^2)$ with scatter σ = 350 km/s, we obtained a 32% bias in the recovered lensing mass.

If we take the effect of kSZ while modeling the pixel-pixel covariance matrix then as expected we eliminate the bias. However, we don't exactly know the kSZ effect of a single cluster. According to current estimates the uncertainty in kSZ prediction is 20% for a single galaxy cluster. The reason for the uncertainty is the complex cluster baryonic physics which is not very well understood. To determine the bias that would result due to the uncertainty in kSZ effect, we test including

20% uncertainty in the kSZ modeling for the pixel-pixel covariance matrix. This results in a low bias of 7.5 ± 0.4 %, the stated bias can either be low or high depending on underestimation or overestimation of kSZ. Interpolating linearly between the kSZ uncertainty and the bias, we find that 2-3% uncertainty in kSZ would lead to sub-percent systematic uncertainty. Given the current uncertainties in kSZ estimation, it acts as a serious obstacle in using temperature information of CMB-cluster lensing for future CMB surveys.

3.4.6 Thermal Sunayev-Zel'dovich effect

Here we give a brief review of thermal Sunayev-Zel'dovich (tSZ) effect and is explained in detail in the next chapter. CMB photons while passing through galaxy cluster are inverse compton scattered of high energetic electrons present in the cluster's hot intra cluster medium. This results in excess of photons at higher frequency and deficit of photons at lower frequency. This is known as tSZ effect. tSZ effect is an order of magnitude greater than lensing signal and will induce significant statistical and systematic uncertainties if not taken into account. In the next two chapters we discuss in detail about the methods through which we eliminate the tSZ bias in QE estimator. Here, we quantify the tSZ bias in the MLE and discuss the methods that can be used to reduce the bias. We consider two different approaches:

- use frequency channels to eliminate the tSZ
- model the tSZ effect in the pixel-pixel covariance matrix

Either approaches has the potential to completely eliminate the bias, however, due to imperfect knowledge of the instrument calibration or the tSZ profile may leave residual bias.

To evaluate the performance of each approach, we use Compton y maps produced on a 5°×5° box at resolution 2.′5 from the smoothed-particle hydrodynamics (SPH) simulations of McCarthy et al. (2014). Neglecting relativistic corrections, we convert the Compton y maps into temperature at an observing frequency according to:

$$\Delta T = y T_{\rm CMB} \left[x \left(\frac{e^{x/2} + e^{-x/2}}{e^{x/2} - e^{-x/2}} \right) - 4 \right] \tag{3.21}$$

where $x = \frac{h\nu}{k_B T_{CMB}}$, ν is the frequency in GHz, $T_{CMB} = 2.73\ K$, κ is the Boltzmann constant, and h is the Planck constant.

tSZ frequency cleaning

Using the spectral dependence of tSZ we can eliminate it by using CMB maps observed at different frequency channels. In this chapter we assume the CMB is observed at 90 GHz and 150 GHz channels with Gaussian beam of FWHM $1.7'$ and $1'$ respectively. Using a linear combination 90 and 150 GHz channels, we obtain tSZ free map as follows:

$$\widetilde{T}(\hat{\mathbf{n}}) = \frac{f\widetilde{T}_{150}(\hat{\mathbf{n}}) - T_{90}(\hat{\mathbf{n}})}{f-1} \tag{3.22}$$

where

$$\widetilde{T}_{150}(\hat{\mathbf{n}}) = T(\hat{\mathbf{n}})_{150} * \frac{B_{90}(\hat{\mathbf{n}})}{B_{150}(\hat{\mathbf{n}})} \tag{3.23}$$

is the 150 GHz map convolved by the ratio of the 90 and 150 GHz beam functions. The factor 'f' is ratio of tSZ amplitude in 90 and 150 GHz.

We also assume that the experimental noise level in both 90 and 150 GHz channels is 1 μK-arcmin. Under these assumptions using a tSZ free map will eliminate the bias (b = 0.0 ± 0.7%). However, it degrades the final SNR by a factor of three as shown in Baxter et al. (2015). In practice, it is unlikely to obtain a precise value of factor 'f' due the uncertainties in frequency band widths or errors in relative calibration of frequency bands. To evaluate the bias in the final results due to the uncertainties in the factor 'f', we use simulations. We assume an uncertainty of 1% in f, which is overly conservative for future CMB surveys but comparable to that of current surveys. An error in f will result in leakage of tSZ in the final tSZ free maps and will bias the results. For 1% uncertainty in 'f' we find the final results to be biased low by -6.3 ± 0.7 percent. The bias can shift depending on whether the SZ leakage is over estimated or under estimated.

tSZ has no power at 217 GHz and one might consider of using 217 GHz frequency channel instead of creating tSZ free maps. However, the power of dusty galaxies increase significantly with frequency. So, the foreground power in 217 GHz channel is much more than 90 or 150 GHz channels. In addition to that, we should also take into account the contamination due to the correlation between the tSZ and cosmic infrared background due to these dusty galaxies.

Current estimates find the correlation coefficient to be $0.113^{+0.057}_{-0.054}$ (George et al., 2015); estimating the tSZ-CIB signal at 220 GHz would yeild a signal nearly three quarters of the tSZ signal at 150 GHz. In order to use 217 GHz channel, more work needs to be done in constraining the tSZ-CIB correlation.

tSZ fitting

Another way to tackle tSZ signal is by modeling it in pixel-pixel covariance matrix. We calculate the expected tSZ contribution using SPH simulations from McCarthy et al. (2014). As one expects, with perfect knowledge of tSZ we get a bias consistent with zero ($b = 1.0 \pm 0.6\%$). However, similar to tSZ frequency cleaning the bias increases quickly if the tSZ contribution is mis-estimated. Misestimating the tSZ signal by 1% leads to significant (order 6%) shifting the recovered mass. Given that the current uncertainties in modeling the tSZ signal from galaxy clusters are at least an order of magnitude larger, it will be extremely challenging to achieve the sub-percent precision necessary to make this approach viable.

3.4.7 Dusty galaxies in the cluster and other foregrounds

Galaxy clusters are known to host overdensities of dusty galaxies, with several papers measuring the resulting tSZ-CIB correlation (Dunkley et al., 2013; George et al., 2015; Planck Collaboration et al., 2016d). We describe our modeling of these DG overdensities[5] in the Appendix A.1.3. If ignored, the tSZ-CIB correlation may substantially bias the recovered masses from temperature estimators, especially at higher frequencies. The emission from dusty galaxies rises sharply with frequency, by an order of magnitude in $\mu K^2_{\rm CMB}$ from 90 to 150 GHz and again from 150 to 220 GHz. Polarization estimators (at least at 150 GHz and lower frequencies) are essentially unaffected due to the lower polarization fraction of dusty galaxies (expected to be less than 4% (Manzotti et al., 2017; Seiffert et al., 2007)). The tSZ-CIB correlated power could be handled analogously to either the tSZ fitting or cleaning approaches in §3.4.6. However, a multi-frequency cleaning scheme will be less effective than for the tSZ effect since the spectral dependence of thermal dust emission varies between individual galaxies. Here we look only at bias for the fitting approach where the pixel-pixel covariance due to the clustered dusty galaxies is folded into the likelihood. The recovered mass is somewhat low: $b = 4.5 \pm 1.7\%$. The existence of a bias (higher than 2σ) is slightly

[5]For implementation reasons, in this section, we include all foregrounds mentioned in the Appendix A.1, even ones that are not correlated with the cluster itself, such as radio galaxies.

surprising since one would expect zero bias in the perfect information limit, and the significance is low enough that it may be a statistical fluke. The dramatic increase in the uncertainty – from 0.25% to 1.7% – reflects the plateauing of the dotted line in right panel of Fig.3.3. Unsubtracted foreground power effectively sets a lower bound on the instrumental noise. Note that here we have considered only dusty galaxies in the cluster (tSZ X CIB correlation) and not the field galaxies.

For stacking analysis we think that cluster asphericity will have negligible impact and so was considered in this thesis. However, future studies should carefully look into the impact of cluster asphericity of CMB cluster lensing.

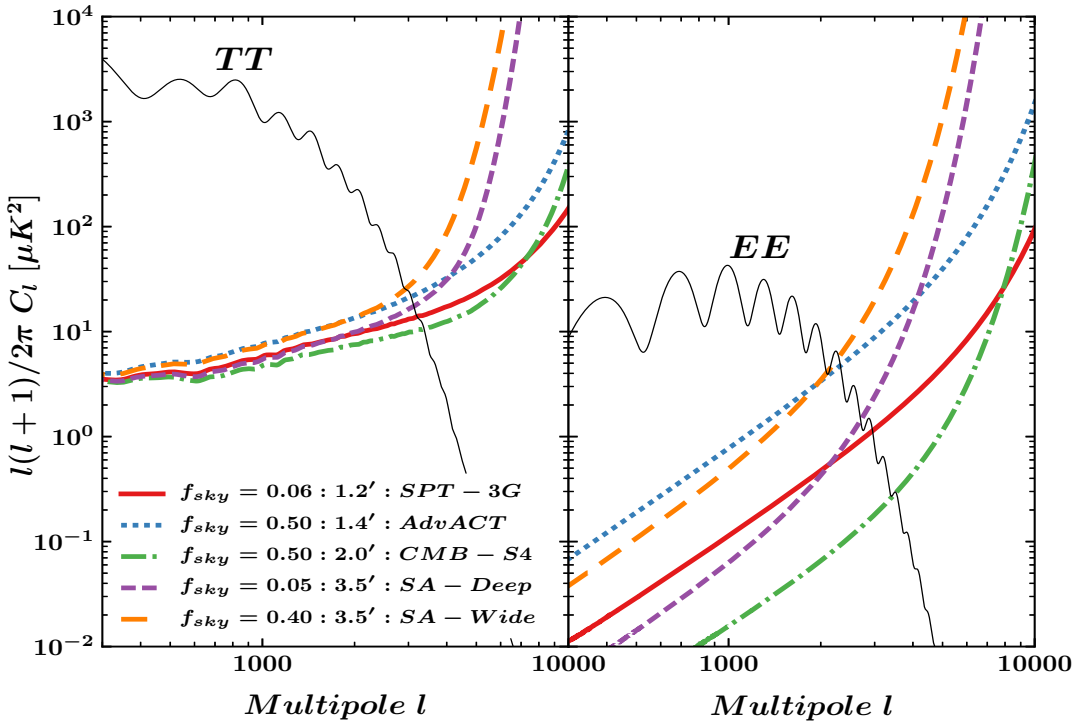

Figure 3.5: The expected residual foreground and noise power spectrum for the future CMB experiments. The 90, 150, and 220 GHz channels have been combined using a constrained ILC technique to remove the tSZ effect while minimizing other extragalactic foregrounds and instrumental power. The left and the right panels correspond to temperature and polarization respectively. The plateauing of the residual temperature spectrum reflects the limited foreground removal possible with three frequency channels. Specifications about each experiment are listed in Table 3.2.

Experiment	ΔT [μK-arcmin]			f_{sky}	Effective beam [$\theta_{\rm FWHM}$]	# of clusters (N_{clus})	$T_{\rm ML}$ (ILC)	$QU_{\rm ML}$ (ILC)
	90	150	220					
CMB - S4	1.0	1.0	1.0	0.50	1.0′	100,000	0.87%	0.83%
					2.0′		0.95%	0.98%
					3.5′		1.20%	1.60%
SPT-3G	4.5	2.5	4.5	0.06	1.2′	10,000	3.28%	6.12%
AdvACT	8.0	7.0	25.0	0.50	1.4′		4.35%	>15%
Simons Array - Deep	1.5	1.5	4.7	0.05	3.5′		4.41%	8.45%
Simons Array - Wide	5.5	5.5	20.0	0.40			5.86%	>15%

Table 3.2: The forecasted mass uncertainties for large-aperture future CMB experiments. We combine data from 90, 150, and 220 GHz to clean the extragalactic foregrounds using a constrained ILC method designed to remove the tSZ signal while minimizing the residual foreground power and instrumental noise. For polarization, the ILC is essentially optimal weighting of the bands for minimum noise. For simplicity we have assumed all the clusters to have a mass of $2\times10^{14}M_{\odot}$ and at redshift $z = 0.7$.

3.5 A look into the future

In this final section we forecast the cluster mass uncertainties from CMB-cluster lensing for the AdvACT , Simons Array, and SPT-3G experiments, which we will collectively refer to as the Stage III experiments, as well as the proposed CMB-S4 experiment. In addition to presenting estimated mass uncertainties for the fiducial versions of these experiments, we examine how the mass uncertainty depends on the beam size and map noise levels. This information can be used to evaluate design tradeoffs while planning future experiments. Note that for the forecasts we have assumed all clusters at mass $M_{200} = 2\times10^{14}M_{\odot}$ and at a redshift of 0.7.

3.5.1 Expected lensing mass uncertainties for future CMB experiments

We expect the next generation of CMB experiments, which will have substantially more detectors and a concomitant reduction in map noise levels, to dramatically improve the cluster mass calibration possible from CMB-cluster lensing. The experimental configuration of all the experiments considered is given in Table 3.2. Three options for telescope size (and therefore beam sizes) are listed for the proposed CMB-S4 experiment. While current results have mass uncertainties of

order ≥ 20% (Baxter et al., 2015; Madhavacheril et al., 2015; Planck Collaboration et al., 2016a), we will show that stage III experiments to reach 3% and CMB-S4 to approach 1%.

There are two reasons for the improvements. First, with more detectors comes lower map noise levels (and larger survey areas). The deepest current experiments reach approximately 5 μK-arcmin in temperature; the Stage III surveys (AdvACT (Henderson et al., 2016); Simons Array (Suzuki et al., 2016), and SPT-3G (Benson et al., 2014)) forecast a few μK-arcmin; and projections for CMB-S4 are $\sim 1\,\mu$K-arcmin. Lower noise improves the lensing significance on any individual galaxy cluster. Second, lower noise levels and larger survey areas translate into substantially more galaxy clusters. Current ground-based SZ cluster catalogs have fewer than 1000 clusters (Hasselfield et al., 2013; Bleem et al., 2015), but SPT-3G is forecast to find 8000 clusters (Benson et al., 2014), AdvACT 10,000 clusters (Henderson et al., 2016) and we assume ad-hoc that CMB-S4 will find 100,000 clusters. In addition to the internally discovered clusters, optical surveys like DES (Rykoff et al., 2016), and in the future LSST (LSST Science Collaboration et al., 2009) and Euclid (Refregier et al., 2010), will yield extremely large numbers of galaxy clusters within the CMB survey regions, as will the X-ray satellite eROSITA (Merloni et al., 2012). This method is perfectly suited to determining the mass calibration for these external cluster catalogs as well.

To provide realistic estimates of the mass uncertainties, we perform a constrained internal linear combination (ILC) of data from 90, 150, and 220 GHz channels based on the `SMICA` (Spectral Matching Independent Component Analysis) algorithm (Cardoso et al., 2008; Planck Collaboration et al., 2014a) to eliminate the tSZ signal from the temperature data and minimize the residual power in other extragalactic foregrounds and instrumental noise in both temperature and polarization.[6] The resulting power spectra of the instrumental noise and residual foregrounds for different CMB experiments are shown in Fig.3.5. At $\ell \leq 2000$, the temperature curves are dominated by residual foreground power as three frequency bands are insufficient to completely eliminate the foreground power in the assumed model (see Appendix). As a result, the temperature noise curves converge at $\ell \leq 2000$ despite the very different noise levels of the experiments. During this process, we convolve the 90 and 220 GHz spectra by the ratio of 150

[6]Note that unlike in Fig3.3 we consider the effect of relative beam and noise levels of different frequency channles

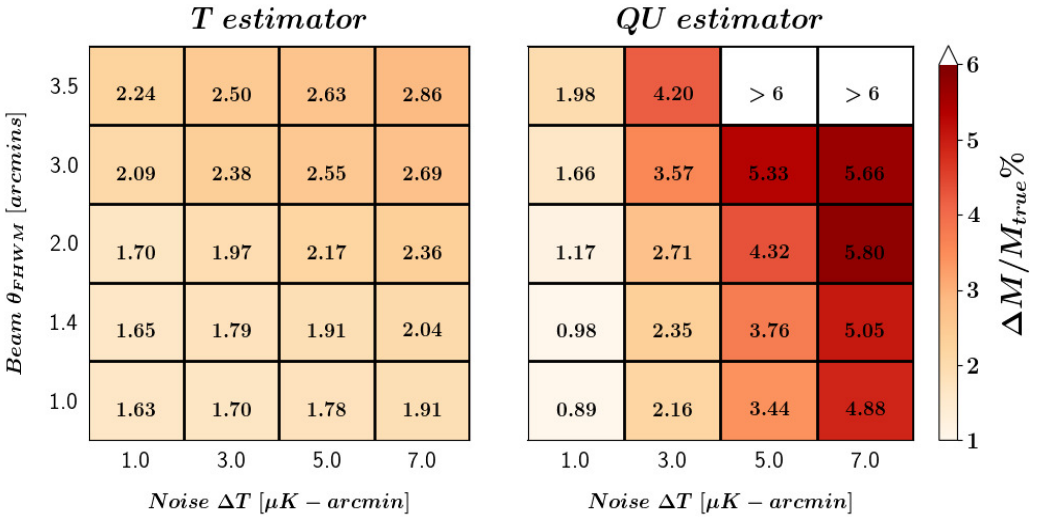

Figure 3.6: The performance of the polarization MLE is very sensitive both to the angular resolution and map noise level of an experiment; the gains for the temperature MLE are much smaller. The numbers correspond to the CMB-cluster lensing mass uncertainty (in percent) of the cluster sample containing 100,000 clusters after the addition of foregrounds (dotted lines in right panel of Fig. 3.3). Improving the beam from 3.′5 to 1′ enhances the SNR by a factor of two for the CMB-S4 noise levels. The saturation of $T_{\rm ML}$ is due to the larger impact of foregrounds on the temperature maps.

GHz beam and their native beams, so that the final effective beam size matches 150 GHz.

The expected performance of each experiment is given in Table 3.2. One significant uncertainty is the number of clusters to assume for each experiment. As accurately modeling the survey selections functions for SZ, optical, and X-ray surveys is beyond the scope of this work, we make the simplifying assumption that all Stage III experiments will have 10,000 clusters and the CMB-S4 experiment will have 100,000 clusters. This is of order the number expected to be discovered through the tSZ effect by the SPT-3G (8000 clusters; Benson et al. (2014)) or AdvACT (10,000 clusters; Henderson et al. (2016)), but likely an over-estimate for the Simons Array due to its larger 3.5′ beam size. On the other hand, the experimental beam size is irrelevant when predicting the size of cluster samples from optical or X-ray surveys that overlap with the CMB surveys. The DES or LSST surveys should provide samples with more than 50,000 clusters for all of the Stage III CMB experiments (Rykoff et al., 2016; LSST Science Collaboration

et al., 2009). Given a specific sample size, the mass uncertainty can be obtained by rescaling the numbers provided in Table 3.2 by $\sqrt{\frac{N_{sample}}{N_{clus}}}$.

Even considering concerns about potential biases from astrophysical signals, the temperature channel will be extremely important for the cluster mass estimates from the Stage III CMB experiments. The mass uncertainty on the fiducial 10,000 cluster sample is similar in temperature from all three experiments, with a range from 3.3% (SPT-3G) to 5.9% (the Simons Array wide survey). These uncertainties are as large as the likely systematic uncertainties, and the statistical uncertainties on polarization are higher by a factor of two or more. As an example of scaling the results with sample size, we replace the fiducial sample size by the expected number counts for SZ-discovered clusters with SPT-3G (8000) and optically detected clusters from the DES (50,000). SPT-3G would achieve a 3.6% mass uncertainty with a sample of 8000 SZ-selected clusters and a 1.5% uncertainty on a sample of 50,000 optically-selected clusters. The shallow portions of the Simons Array or AdvACT surveys cannot contribute much for the polarization estimator; lower noise levels are essential. The polarization estimator can be within a factor of two for the deep surveys of the Simons Array or SPT-3G. For instance, the polarization estimator for SPT-3G on 8000 clusters yields a 6.8% mass calibration, to be compared to the 3.6% mass calibration from temperature (ignoring systematic uncertainties).

The lower level of systematic uncertainty for polarization comes into play for the CMB-S4 experiment. First, for the extremely low noise levels of CMB-S4, the performance of the temperature and polarization channels is nearly identical (0.95% vs. 0.98%) for an instrument with $2'$ beam resolution. Second, the magnitude of the temperature-only systematic errors (primarily from the SZ effect) is now several times larger than the raw statistical uncertainties, and would dominate the temperature error budget. We can expect cluster mass calibrations from CMB-S4's polarization data at the 1% level.

The mass calibration forecasts in Table 3.2 are highly complementary to and competitive with the masses obtained by stacking optical weak lensing measurements. For example, LSST hopes to achieve a mass uncertainty of 1% by stacking few thousands of clusters at redshifts $z < 0.5$ (LSST Science Collaboration et al., 2009). At high redshifts, since the number density of background galaxies decrease rapidly, the constraints from optical lensing measurements tend to weaken. Calibrating the high redshift end of the mass function is the true power of CMB-

cluster lensing which will allow us to place important constraints on the redshift evolution of mass-observable scaling relations out to high redshifts $z \geq 1.5$.

3.5.2 Optimizing survey design: SNR as a function of beam size and map noise levels

There are plans underway to build a substantially more sensitive CMB experiment, CMB-S4 (CMB-S4 Collaboration et al., 2016), with work already underway both on design studies and planning for CMB-S4 and on pathfinder experiments to CMB-S4 such as the Simons Observatory. There is a wide spectrum of science drivers for these experiments, of which CMB-cluster lensing is only one. However, it is useful to consider what CMB-S4 design choices would be optimal for cluster mass calibration. In this section, we consider two lever arms: map noise levels and angular resolution (beam size). In all cases, we assume three frequency bands centered at 90, 150 and 220 GHz with equal noise levels and beam sizes that scale as the wavelength. We do not consider the number or relative weight of frequency bands, although these decisions will be important for handling astrophysics foregrounds in the temperature estimator.

In Fig.3.6, we present the mass uncertainties on a sample of 100,000 clusters from the temperature and polarization estimators for a grid of five different beam sizes $\theta_{\rm FWHM} = 1', 1.'4, 2', 3', 3.'5$, and four temperature map noise levels (1, 3, 5, or 7 μK-arcmin). We have simplified the problem by using only 150 GHz data with no foreground removal. As a result, the quoted uncertainties are likely to be too large for both temperature and polarization estimators. However, the qualitative conclusions are robust to this assumption as will be shown below by spot-checking the results with a full ILC analysis.

Notably, the temperature results show only a minor improvement ($< 20\%$) going from 7 to 1 μK-arcmin noise levels. The plateauing occurs because the instrumental noise is already smaller than the foreground power. Although the exact level may be off, these 150 GHz only results are consistent with the picture from the full, 3-frequency ILC analysis shown in Fig.3.5. In that figure, the residual foreground and noise power curves for temperature are essentially the same, whether from CMB-S4, from small and deep Stage III surveys, or from wide and shallow Stage III surveys. In short, foreground residual power dominates the results even at the lower sensitivities of the Stage III experiments. The temperature estimator also shows a fairly modest effect from reducing the beam

size: a factor of 3.5 reduction in beam size from 3.′5 to 1′ only improves the mass uncertainty by a factor of 1.35. This is because the foreground power floor limits the use of small-scale modes where the beam size matters most.

In contrast, as seen in the right panel of Fig.3.6, the fidelity with which the QU polarization estimator recovers cluster masses is strongly dependent on the experimental noise level and beam size. The clear improvements are because polarization estimator is still noise instead of residual foreground dominated. Improving map noise levels from 3 to 1 μK-arcmin improves the SNR on CMB-cluster lensing by a factor of 2.4 (the equivalent change for the temperature estimator is only 1.04). Similarly, reducing the beam size three fold from 3′ to 1′ leads to an improvement by a factor of 1.9. Both the beam size and instrumental noise levels matter for the performance of the polarized CMB-cluster lensing estimator.

Finally, we confirm this picture by extending these 150 GHz-only predictions to 3-band data using the ILC method. We assume equal temperature map noise levels of 1μK-arcmin at 90, 150 and 220 GHz, with a beam size that scales with the wavelength. We consider three 150 GHz beam sizes, $1', 2'$, and 3.′5, with the results tabulated in Table 3.2. The improvement as a function of the beam size is consistent between the 150 GHz and ILC cases. While the improvement is only marginal for the temperature channel, the mass uncertainty from the polarization estimator drops to 0.83% for a 1′ beam, a factor of 1.9 better than the results for a 3.′5 beam. The corresponding improvement for 150 GHz only is slightly better, at a factor of 2.2.

3.6 Conclusion

We have developed MLEs to optimally extract lensing information from the temperature (T) and polarization (Q/U) maps of the CMB. We show a Q/U based MLE recovers as much information as an estimator using E and B mode maps. We also show that the temperature MLE performs better than the standard QE by a factor of two at very low noise levels in the absence of astrophysical foregrounds; the performance gain is not significant for the polarization estimator due to the lower SNR. We consider the effects of these foregrounds on the cluster lensing estimators, finding at 150 GHz that astrophysical foregrounds have no impact on the polarization MLE and set an effective noise floor of a few μK-arcmin on the temperature MLE unless removed using multi-frequency data.

We quantify the systematic uncertainties due to astrophysical foregrounds (the tSZ effect, kSZ effect or dusty galaxies), uncertainty in the cluster position or redshift, projection effects from nearby lower-mass haloes, and uncertainty in the cluster mass profile. We find that the dusty galaxies in the cluster are likely to bias the temperature(polarisation) MLE at -4.5%(-1.3%) level. The biases due to uncertainty in the cluster position or redshift are manageable for both temperature and polarization. Lower mass haloes near the galaxy cluster lead to an overestimate of the cluster masses at the 2.5 to 6.3% level, and will need to be carefully accounted for using simulations. The uncertainties in the cluster mass profile can shift the cluster mass either up or down by up to a few percent. Better measurements of the cluster mass profile are needed to reduce this uncertainty.

The clusters own SZ signals induce significant bias on temperature MLE. The kSZ effect has the same spectral dependance as that of CMB and cannot be removed using multiple frequency channels; it will induce a bias of -7.3% on temperature MLE. tSZ induce significant biases on MLE estimators if not taken into account. tSZ is an order of magnitude greater than lensing signal and if not taken into account will kill the lensing signal. We can exploit multiple frequency channels to remove tSZ, however, that will decrease the SNR by a factor of three (Baxter et al., 2015). In the next two chapter we will introduce modified QE to eliminate the tSZ bias with negligible decrease in SNR.

Finally, we present forecasts for the mass uncertainties from upcoming CMB experiments, combining multiple frequency bands with an ILC technique to minimize the instrumental noise and astrophysical foregrounds. The AdvACT, Simons Array and SPT-3G experiments will achieve mass calibration uncertainties of order 3 - 6% for a sample containing 10,000 clusters, with the temperature channel being crucial to these mass constraints. With the even lower noise levels of CMB-S4 and a $2'$ beam, we find the statistical mass uncertainty from either the temperature or polarization MLEs falls to just below 1% with 100,000 clusters. We expect polarization to be the main information channel for CMB-S4 given the potential biases due to the temperature foregrounds. Finally, we consider how the performance of CMB-S4 depends on the assumed noise level or beam size, finding that a factor of three reduction in either the beam size or noise level leads to roughly a factor of two improvement on the mass calibration from the polarization MLE. CMB-S4 has the potential to transform galaxy cluster cosmology by reducing the current 20% mass uncertainty on galaxy clusters twentyfold to

$\sim 1\%$.

Chapter 4

Modified Quadratic Estimator

Overview

In the last chapter 3.4.6 we saw that the thermal Sunayev-Zel'dovich (referred as SZ hereafter) effect is a major contamination in the CMB-cluster lensing analysis. One of the ways to mitigate the SZ induced systematic bias in the Maximum Likelihood Estimator (MLE) is by using SZ-free maps. However, SZ-free maps have higher noise resulting in decrease of signal to noise ratio (SNR) by a factor of three. During my thesis, we developed a modified Quadratic Estimator (mQE) to eliminate the bias due thermal Sunyaev Zel'dovich (SZ) effect with only a slight decrease in SNR.

This chapter is organised as follows. First, we provide a brief review of the SZ effect in 4.1 (refer Sunyaev and Zel'dovich (1970) for a detailed review) and its effect on CMB-cluster lensing in §4.2.1. We discuss the modifications done to the QE in order to remove the SZ bias in §4.2. The datasets and model fitting are described in §4.4 and §4.5 respectively. Before we apply our new method to data in §4.7, we validate our pipeline using simulations in §4.6. The effect of systematics involved in the analysis is quantified in §4.6.3. Finally, we conclude in §4.8. This chapter closely follows Raghunathan et al. (2019a).

4.1 Thermal Sunayev-Zel'dovich effect

The Cosmic microwave background (CMB) photons get inverse Thompson scattered off the high energy electrons present in the intra cluster medium of a galaxy cluster, resulting in the deficiency of photons at lower frequencies and excess of photons at higher frequencies. This phenomena is called the thermal Sunayev-Zel'dovich (SZ) effect. The SZ is a small effect and we illustrate it by showing the CMB spectral distortion for a fictional galaxy cluster 1000 times more massive than a typical galaxy cluster in Fig. 4.1. The solid black curve represents the intensity of the CMB as a function of frequency before its interaction with hot

intracluster medium and the solid blue represents the same after its interaction. As shown in the Fig. 4.1, due to the SZ effect CMB intensity decreases below a frequency of ~220 GHz and increases at higher frequencies.

The fractional change in temperature is given by

$$\frac{\Delta T_{SZ}}{T_{CMB}} = f(x)y = f(x)\int n_e \frac{k_B T_e}{m_e c^2}\sigma_T dl \tag{4.1}$$

where y is Compton y-parameter, n_e is the electron number density, m_e is the electron rest mass, c is the speed of light, T_e is the electron temperature, σ_T is the Thompson cross-section, and $f(x)$ is the dimensionless frequency given by

$$f(x) = \left(x\frac{e^x+1}{e^x-1} - 4\right)(1 + \delta_{SZE}(x, T_e)) \tag{4.2}$$

where $\delta_{SZE}(x, T_e)$ is the relativistic correction to the frequency dependence.

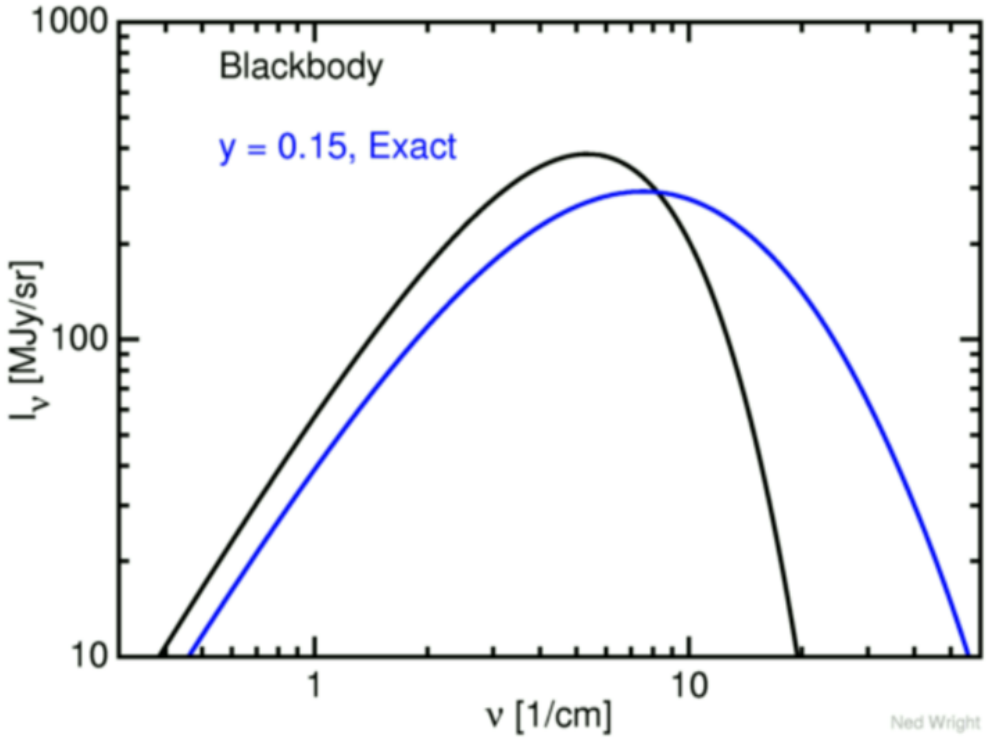

Figure 4.1: The plot shows the intensity of CMB as function of frequency before (black) and after (blue) it passes through a cluster. Credits: Ned Wright, UCLA

The CMB surveys make use of the SZ effect to detect galaxy clusters which appear as a semi-resolved negative signal decrement at frequencies lower than 220

GHz. As can be inferred from Eq. 4.1, the SZ effect is independent of redshift and has the potential to detect high redshift clusters, where the cluster abundance critically depends on the underlying cosmological model.

Fig. 4.2 shows a galaxy cluster of mass $M_{200m} = 5 \times 10^{14} M_{\odot}$[1] at a redshift of $z = 0.7$ as observed by a CMB survey in 90 GHz and 150 GHz channels. While the beam size of 90 GHz channel is bigger than the 150 GHz for a given CMB experiment, here we have assumed the beam sizes of both frequency channels to be $1'$ in order to show the amplitude difference.

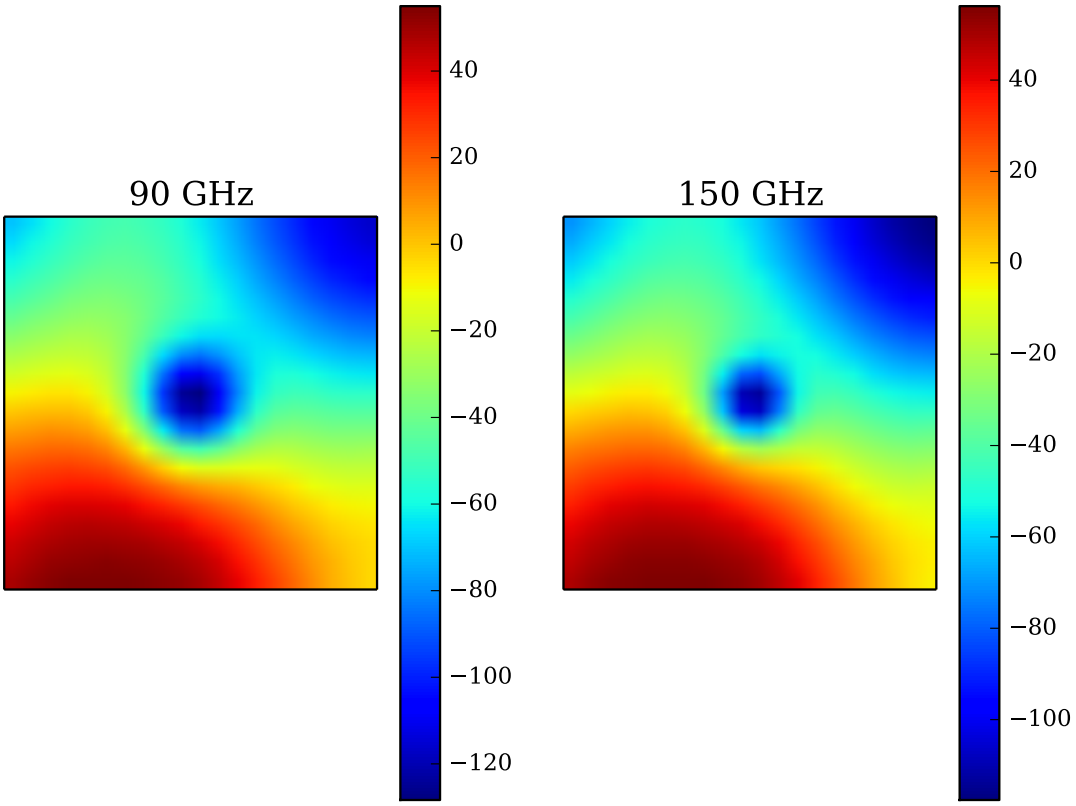

Figure 4.2: A galaxy cluster of mass $M_{200m} = 5 \times 10^{14} M_{\odot}$ at redshift of $z = 0.7$ as observed by a CMB survey with a beam size of $1'$ in both 90 and 150 GHz channels. Each image extends $10' \times 10'$ and the colorbar is μK. It is worth noting that the amplitude of SZ signal in the 90 GHz channel is higher by a factor ~ 1.67 compared to the corresponding SZ signal in the 150 GHz channel.

[1] M_{200m} is defined as the mass of the cluster within radius, R_{200}, within which the cluster density is 200 times the mean density of the Universe at cluster redshift.

4.2 Quadratic Estimator

As mentioned in the previous chapter, lensing remaps the unlensed CMB field. To a first order approximation it can be written as

$$T(\hat{n}) \approx \tilde{T} + \nabla T.\vec{\alpha}(\hat{\mathbf{n}}) \tag{4.3}$$

$$T(\hat{n}) - \tilde{T} \approx \nabla T.\vec{\alpha}(\hat{\mathbf{n}}) \tag{4.4}$$

where $\tilde{T}$ represents the unlensed temperature field, $\hat{n}$ is the direction vector, $\vec{\alpha}$ is the deflection angle which depends on the cluster mass. While this is just a first order approximation, it holds particularly well for the CMB-cluster lensing. This can understood as follows:

- the typical size of a galaxy cluster is of the order of few arc minutes (z>0.3)
- the primordial CMB doesn't have power at such small angular scales due to diffusion damping (Silk, 1968) and can be approximated as a gradient.

It is straight forward to see from Eq. 4.4, for a cluster of given mass and redshift, the magnitude of the lensing signal (dipole like pattern) scales linearly with the magnitude of the CMB gradient. This correlation between the unlensed CMB gradient and the lensing signal is exploited by the Quadratic Estimator (QE) to estimate the cluster mass. Below we provide a brief mathematical formalism for temperature QE and it readily generalises for polarisation. For a detailed review the reader is encouraged to refer Hu et al. (2007).

The gradient approximation doesn't hold for all Fourier modes, but for the modes which are correlated by reconstruction. We filter the maps in the Fourier space to isolate modes for which the gradient approximation is valid. We obtain the filtered gradient map and lensing map from the observed map as follows,

$$L(\hat{n}) = \int \frac{d^2l}{(2\pi)^2} e^{il.\hat{n}} W_l^T T_l \tag{4.5}$$

$$G(\hat{n}) = \nabla\left(\int \frac{d^2l}{(2\pi)^2} e^{il.\hat{n}} W_l^{TT} T_l\right) \tag{4.6}$$

where $G(\hat{n})(L(\hat{n}))$ is filtered gradient (lensing) map, T_l is the observed temperature map in Fourier space, and l is the angular multipole. Fourier filters W_l^T and

W_l^{TT} are given by

$$W_l^T = (C_l^{TT} + N_l^{TT})^{-1} \tag{4.7}$$

$$W_l^{TT} = \widetilde{C}_l^{TT}(C_l^{TT} + N_l^{TT})^{-1} \tag{4.8}$$

where $\widetilde{C}_l^{TT}$,C_l^{TT} is the unlensed and large scale structure lensed CMB power spectrum obtained from `CAMB` (Lewis et al., 2000), N_l^{TT} is the noise power spectrum obtained after deconvolving the experimental beam and filter transfer functions.

Given the correlation between gradient and the lensing map, we can form the QE estimator by multiplying the gradient field and the lensed temperature field. Expanding this product under gradient approximation yields:

$$\begin{aligned}\mathbf{G}\, L \approx\ \nabla\,(\widetilde{T_G})\,\widetilde{T_L}\ + (\nabla\widetilde{T_G})\,(\nabla\widetilde{T}.\nabla\phi)_L + [((\nabla\phi).\nabla)\nabla\widetilde{T} + ((\nabla\widetilde{T}).\nabla)\nabla\phi]_G\widetilde{T_L} \\ +[((\nabla\phi).\nabla)\nabla\widetilde{T} + ((\nabla\widetilde{T}).\nabla)\nabla\phi]_G(\nabla\widetilde{T}.\nabla\phi)_L\end{aligned} \tag{4.9}$$

Under the assumption that cluster lensing is a small perturbation to the unlensed image, we can neglect the quadratic terms in ϕ. By averaging over realisations of the unlensed temperature field we get a quantity proportional to $\nabla\phi$ or the lensing convergence profile, κ,

$$\hat{\kappa_l} = -A_l \int d^2\hat{n}\, e^{i\hat{n}.l}\, Re\nabla.[G(\hat{n})L^*(\hat{n})] \tag{4.10}$$

where A_l is the normalisation parameter given by

$$\frac{1}{A_l} = \frac{2}{l^2} \int \frac{d^2l_1}{4\pi^2}(l.l_1)\, W_l^{TT}\, W_l^T\, (\tilde{C}_{l_1}^{TT}\,(l.l_1) + \tilde{C}_{l_2}^{TT}\,(l.l_2)) \tag{4.11}$$

where $l = l_1 + l_2$. The schematic representation of quadratic estimator is shown in Fig. 4.3. The top panel is the $10' \times 10'$ cutout of the observed temperature map. The observed temperature maps is then filtered in the fourier space (using Eqs. 4.8 and 4.7) to obtain the filtered gradient and lensed maps, shown in middle right and left panels respectively. The lensing convergence map is reconstructed by extracting the correlations between the lensing and the gradient map, which is shown in the bottom panel. Note that Fig. 4.3 is for only idealised simulations and we have neither included experimental noise nor foregrounds.

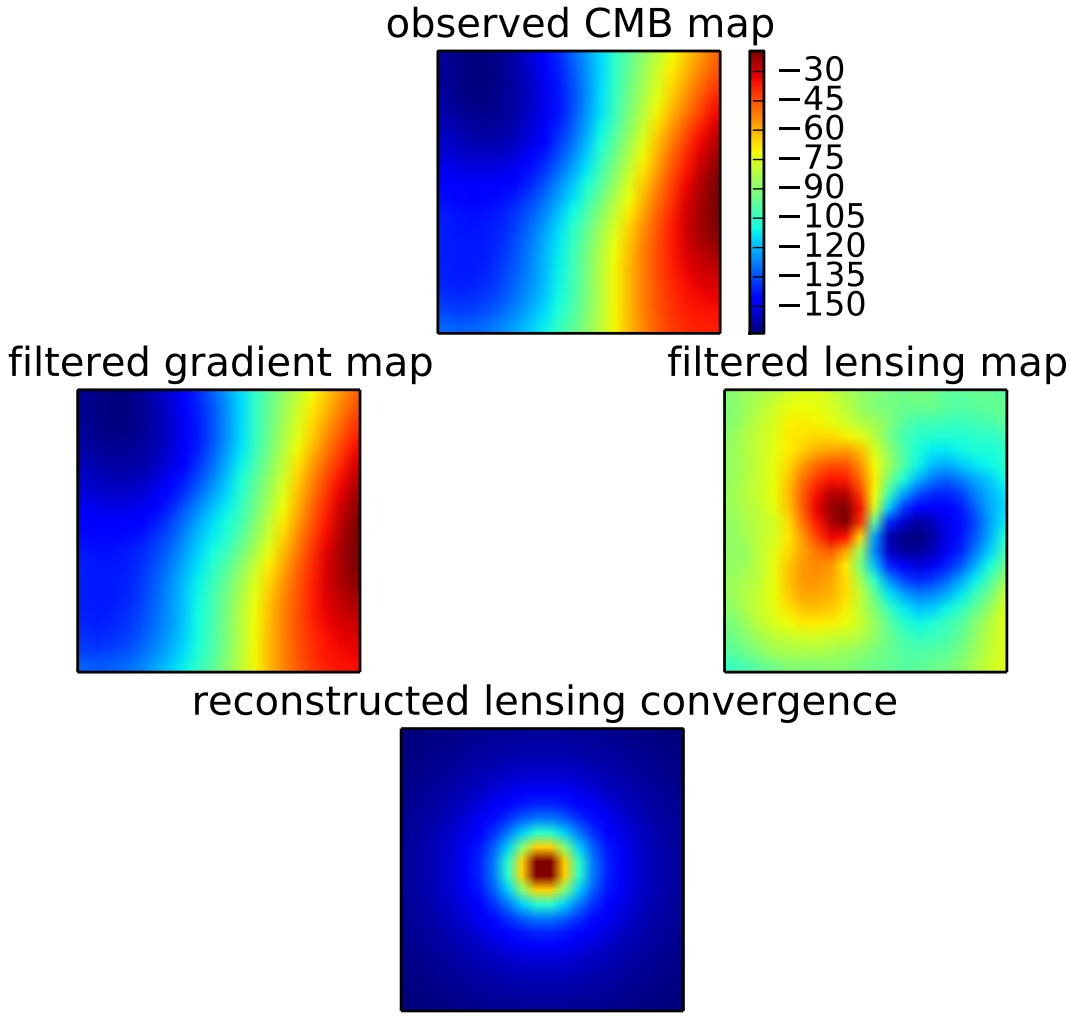

Figure 4.3: Schematic representation of the QE. The top panel shows the observed CMB temperature map, which is then passed through the filters to obtain the large scale gradient map (left middle panel) and the small scale lensing map (right middle panel). The QE extracts the correlation between the gradient map and the lensing map to obtain the reconstructed lensing convergence profile shown in the bottom panel.

mitigating the magnification bias:

Galaxy cluster magnifies the background image and decreases the observed temperature gradient behind it, which leads to a low bias in the lensing reconstruction. The bias is due to the overlap in scales between the unlensed gradient field and lensed temperature field. Though wiener filter reduces the bias, the filter cannot remove the bias. We can reduce the bias further by exploiting the prior

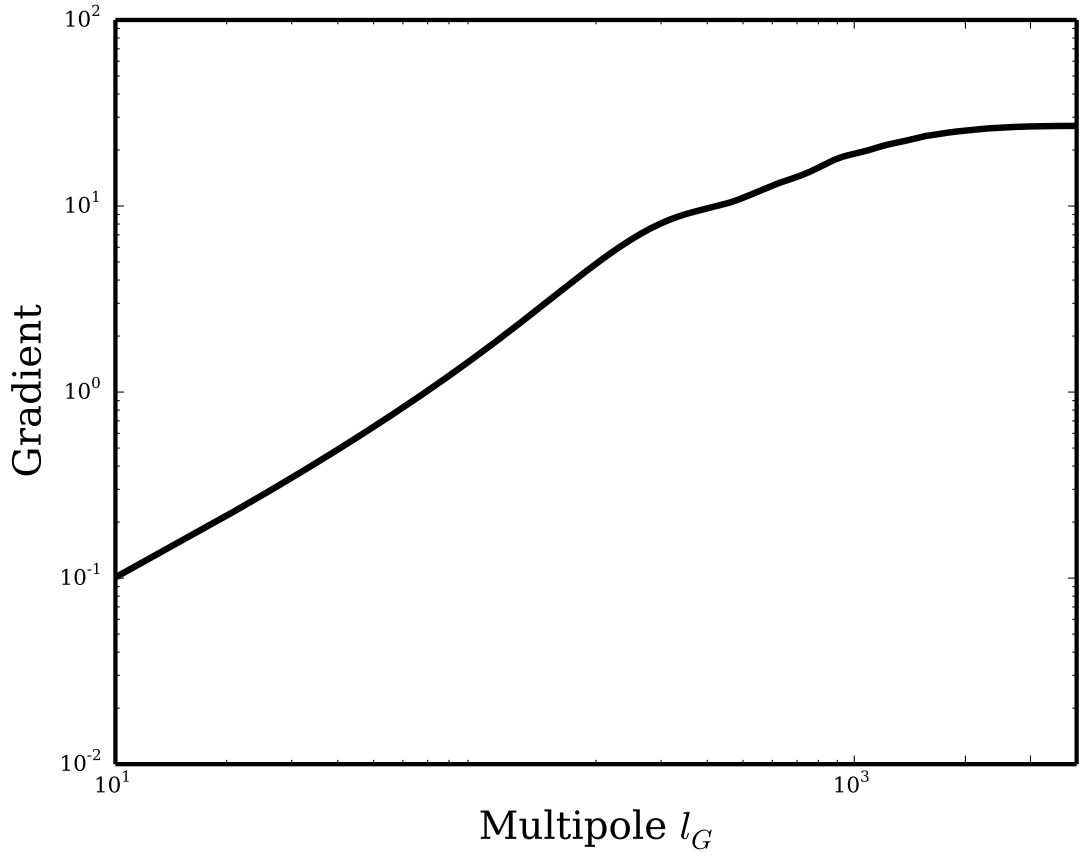

Figure 4.4: Gradient of temperature field as a function of the maximum of a top hat low pass filter (LPF), $l = l_G$. The curve has plateau above $l_G > 2000$. Low pass filtering the gradient map with $l_G < 2000$ mitigates the magnification bias without affecting the SNR.

knowledge on unlensed CMB power spectrum. From Fig. 4.4, which shows the unlensed rms gradient as a function of a top hat low pass filter, it is evident that most of the power for the gradient map comes from scales below $l \leq 2000$. By low pass filtering the gradient map $l \leq 2000$ the SNR of the gradient map is negligibly affected. On these scales, the lensing correction is only tiny for a typical cluster. We get a clean separation between the unlensed gradient and the lensed temperature field by modifying the filter in Eq. 4.8 to

$$W_l^{TT} = \begin{cases} \widetilde{C}_l^{TT}(C_l^{TT} + N_l^{TT})^{-1} & l \leq l_G \\ 0, \quad otherwise \end{cases} \tag{4.12}$$

where $l_G = 2000$.

It is worth here to note that the magnification bias depends on the mass of a galaxy cluster - higher the mass higher the bias. While l_G = 2000 should be sufficient to low mass clusters, for rare massive clusters (few times $10^{14} M_\odot$) even the large scale modes are significantly affected by the magnification bias and more aggressive l_G = 1000 yields a bias free reconstruction (Hu et al., 2007).

4.2.1 SZ induced bias

Though SZ is a small spectral effect, it is still much higher than the lensing signal. It is an order of magnitude larger than the lensing signal inducing a significant systematic and statistical uncertainty if not taken into account. Fig 4.5 shows the effect of SZ on the lensing convergence profile. We simulate 1000 clusters each with a mass of 2×10^{14} $M_\odot$ and at a redshfit of $z = 0.7$. To these simulated clusters we add experimental white noise noise level of $3\mu\mathrm{K}'$. On the top panels we show the stacked lensing convergence profile of these 1000 clusters - the left panel is without adding SZ and the right panel is after adding Arnaud et al. (2010) SZ profile. As can be inferred from the plot, the presence of SZ induces a semi-resolved negative signal decrement (blue blob) in the center resulting in a negative bias. In the bottom panel we have the radial profiles of the two-dimensional kappa profiles. The blue (green) solid curve represents the radial lensing convergence profile with (without) SZ; the solid black curve represents the theoretical model.

4.2.2 Modified quadratic estimator

While designed to pull out the lensing induced correlations, QE is equally sensitive to any other signal present in both G and L maps. SZ present in both the maps results in a low bias if not taken into account as shown in Fig. 4.5. Two methods have been discussed in literature to eliminate/mitigate the SZ bias: one of the ways to eliminate the SZ bias is by using SZ free maps, which are constructed by exploiting the spectral dependance of the SZ signal. However, this results in an increased statistical uncertainty in the reconstructed convergence profile. Another way to mitigate the bias is by using a more stringent low pass filter on the gradient map, wherein a robust separation of scales between gradient map and small scale map reduces SZ correlation. While this can reduce the bias significantly, poor gradient estimation results in an increased statistical uncertainty.

During this thesis, we came up with a novel approach to completely remove

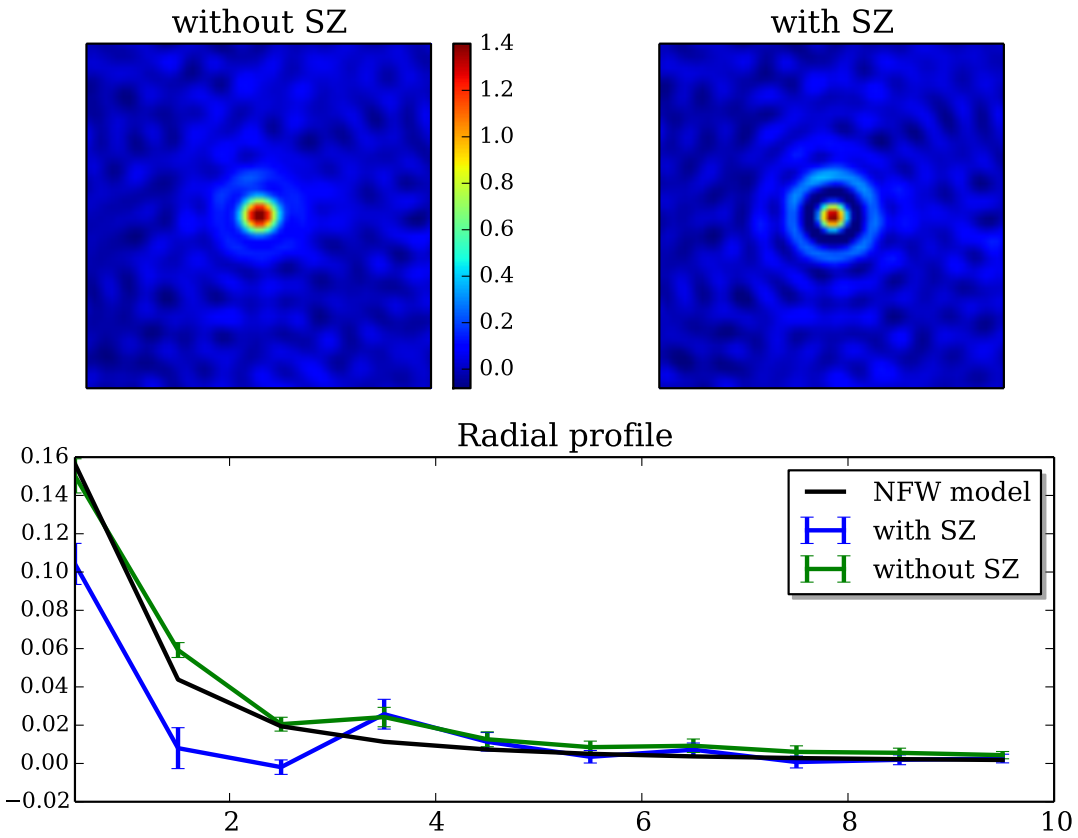

Figure 4.5: Effect of SZ on lensing convergence profile. On the top panel we show the lensing convergence profile for a stack of 1000 cluster each at a mass of $M_{200m} = 2 * 10^{14} M_{\odot}$ and a redshift of $z = 0.7$ with experimental white noise level of 3μK – arcmin; left panel is without SZ and right panel is with SZ. On the bottom panel we have radial profile of the same in solid blue (without SZ) and green (with SZ) curves; black curve is the radial profile of the input NFW profile.

the SZ bias. Any foreground signal which is present in both the maps (gradient and lensing) will lead to a systematic bias; therefore, removal of the foreground signal in one of the maps (either gradient or lensing map) should eliminate the bias completely. As shown in Fig. 4.4, most of the gradient estimation comes from multipoles $l \leq 2000$ where CMB is not limited by experimental noise. The natural choice would be to eliminate SZ in the gradient map by using linear combination of different frequencies. In the mQE, Eqn. 4.6 becomes,

$$G(\hat{n}) = \nabla\left(\int \frac{d^2l}{(2\pi)^2} e^{il.\hat{n}} W_l^{TT} T_l^{SZ-free}\right) \tag{4.13}$$

where $T_l^{SZ-free}$ is an SZ-free map obtained by linear combination of different frequency channels. Also the Eqns. 4.7 and 4.8 are modified to

$$W_l^{TT} = \begin{cases} \widetilde{C}_l^{TT}(C_l^{TT} + N_l^{TT-SZ-free})^{-1} & l \leq l_G \\ 0, \quad otherwise \end{cases} \qquad (4.14)$$

$$W_l^T = (C_l^{TT} + N_l^{TT})^{-1}.$$

where $N_l^{TT-SZ-free}$ is noise power spectrum of the SZ-free map obtained after deconvolving the experimental beam and transfer function.

4.3 Cluster cutouts

We extract $300'$ square box from the data temperature maps at the cluster locations. The boxsize is much larger than the virial radius of the cluster; however, it is necessary to robustly approximate the background gradient. This is because much of the gradient power comes from large scale modes, reducing the analysis to a smaller box will reduce the SNR of the mass estimation. These cutouts are then passed through the pipeline to extract lensing convergence profile, after which we limit the modelling and likelihood calculations to $10'$ box around a cluster to reduce the computational complexity.

As mentioned before, the lensing signal is weak for individual cluster and we need to stack lensing convergence profiles to increase the SNR of detection. Thus the stacked convergence map is simply:

$$\hat{\kappa} = \frac{\sum_j w_j \left[\hat{\kappa}_j - \langle \hat{\kappa}_j \rangle\right]}{\sum_j w_j} - \hat{\kappa}_{\rm MF}, \qquad (4.15)$$

where $\hat{\kappa}_j$ refers to the reconstructed convergence map of j^{th} cluster and w_j is weight assigned to the j^{th} cluster. We remove an estimate of the mean-field $\hat{\kappa}_{\rm MF}$ from this stacked convergence map. The mean-field arises because of two following reasons:

- the temperature maps are apodized using a Hanning window with a $10'$ edge taper to reduce edge effects which induces undesired mode correlation.
- the presence of inhomogeneous noise in the survey region.

We obtain the mean field bias by stacking the convergence maps reconstructed at 50,000 random locations in the maps.

Weighing scheme: We completely eliminated the SZ-induced bias by using SZ-free maps. However, the SZ present in the lensing map induces extra variance. The SZ variance is proportional to the SZ brightness and scales roughly as $M^{5/3}$. We will discuss in detail a refined mQE to suppress the SZ induced variance in the next chapter 5. Here we just down weigh the clusters based on their SZ variance. We decompose the weights assigned for each cluster into two components: inverse noise variance weight and SZ variance weight.

The inverse-noise-variance weight, w_k, is obtained from the data. We pass data cutouts through pipeline to get the lensing convergence profile. As most of the lensing signal is within $10'$ of the cluster center, the variance outside $10'$ should be identical to the inverse-noise-variance. We take the standard deviation in the reconstructed convergence maps in a ring between $10'$ and $30'$ around the cluster center and define it as σ_κ .

The second weight comes from the noise in the convergence maps due to the presence of SZ signal in the lensing map.We obtain this second set of weights, $w_{\rm SZ}$, using simulations. For every cluster in the sample, we reconstruct the convergence profile using a simulated SZ-free gradient map and the lensing map with SZ signal assuming an Arnaud profile (Arnaud et al., 2010) with a log-normal scatter of 20% in the $Y_{SZ} - M$ relation. We pass these simulated cutouts through our pipeline and turn off cluster lensing as the objective here is to only get an estimate of the SZ-induced noise in the convergence maps. A total of 25 simulations are used to get the noise estimate for each cluster. The weights are estimated as $w_{\rm SZ} = 1/\sigma^2_{\rm SZ}$, where $\sigma_{\rm SZ}$ is the standard deviation of the 'null' convergence map within an angular distance of $10'$ from the cluster centre.

The total weight is now:

$$w = \frac{1}{\sigma^2_\kappa + \sigma^2_{\rm SZ}}. \tag{4.16}$$

As expected, introducing $w_{\rm SZ}$ down weighs the massive clusters as the SZ variance is $\sim M^{5/3}$. This reduces the contribution of clusters with $\sigma_{\rm SZ} > \sigma_\kappa$ resulting in a decrease of SNR. The number of clusters with dominate SZ variance depend on the mass distribution of cluster catalog and the experimental noise level (which will be discussed in detail in next chapter 5). One of the alternative ways to tackle this problem would be to swap the maps, by using SZ-free lensing map and single frequency channel for gradient map. However, this still won't help us in gaining SNR as the SZ-free maps have higher noise level than a single frequency map.

For SPTpol like experiment which observes sky in 90 and 150 GHz the SZ-free noise level is 3 × larger than 150 GHz noise level.

4.4 Model Fitting

With cluster cutouts obtained from §4.3 and the method to extract convergence profile (§4.2) in hand, we can fit the model to the observed convergence. To obtain the mass of the cluster, we need to compare the observed lensing profile to the convergence model generated using an assumed halo mass profile. The observed lensing convergence profile of cluster has contributions from its own halo density (κ_{1h}) as well as from the correlated structures along the line of sight known as two halo term (κ_{2h}) (Oguri and Hamana, 2011). For κ_{1h}, we assume the galaxy cluster density to follow Navarro Frenk White (NFW,(Navarro et al., 1996)) profile and in 4.6.3 we quantify the robustness of this assumption by using Einasto profile (Einasto and Haud, 1989). A NFW halo profile is characterized by its scale radius R_s, the dimensionless concentration parameter c, and the dimensionless characteristic over-density δ_c. The lensing convergence profile for NFW is obtained as discussed in the previous chapter §3.1 which we represent as $\kappa_{1h}(\theta)$. We also add two halo term (κ_{2h}) (Oguri and Hamana, 2011) to the $\kappa_{1h}(\theta)$ to get $\kappa(\theta)$. With the model prediction in hand, we can then write down the likelihood of observing the data convergence profile as:

$$-2\ln\mathcal{L}(\hat{\kappa}(\theta)|\mathrm{M}) = \sum_{\theta,\theta'=0}^{10'} \left[\hat{\kappa}(\theta) - \kappa(\theta)\right] \hat{\mathrm{C}}^{-1}_{\theta,\theta'} \left[\hat{\kappa}(\theta') - \kappa(\theta')\right] \tag{4.17}$$

where $\hat{\kappa}(\theta)$, $\kappa(\theta)$ are the azimuthally averaged radial profiles of the stacked data and model convergences respectively, binned in 10 linearly spaced intervals with $\Delta\theta = 1'$.

We use the jackknife re-sampling technique to obtain the covariance matrix. We divide the SPTpol 500 deg^2 region into $N = 500$ sub-fields and estimate the covariance matrix for the radially binned convergence profile as

$$\hat{\mathrm{C}} = \frac{N-1}{N} \sum_{j=1}^{N=500} \left[\hat{\kappa}_j(\theta) - \langle\hat{\kappa}(\theta)\rangle\right] \left[\hat{\kappa}_j(\theta) - \langle\hat{\kappa}(\theta)\rangle\right]^T, \tag{4.18}$$

where $\hat{\kappa}_j(\theta)$ is the azimuthally binned stacked convergence of all the clusters in the j^{th} sub-field and $\langle\hat{\kappa}(\theta)\rangle$ is the ensemble average of all the 500 sub-fields. We test this approach by alternatively estimating the covariance matrix using 500

realizations of the random convergence stacks. We do not note any significant differences between the uncertainties estimated using the two approaches. We apply the Hartlap et al. (2007) correction to $\hat{\mathrm{C}}^{-1}$ to account for the noise in covariance estimation due to the finite number of jackknife re-sampling.

While fitting model to the real data we need to account for mis-centering of cluster, otherwise the results are biased low. For instance Rykoff et al. (2016) compared the centroids DES RM clusters with SZ (Bleem et al., 2015) and X-ray observations and found a fraction, $f_{mis} = 0.22 \pm 0.11$, of the DES clusters to be mis-centered by σ_R, which is a fraction of the cluster radius $R_\lambda = (\lambda/100)^{0.2}\, h^{-1}$. They further modelled the mis-centering as a Rayleigh distribution with $\sigma_R = c_{mis} R_\lambda$ where $\ln c_{mis} = -1.13 \pm 0.22$. Mis-centering smears the convergence profiles and we use the prescription provided in Eq. (34) of Oguri and Hamana (2011) to account for cluster mis-centering in the real data. As we will see in §4.5, we lose some modes due to data filtering and the experimental beam size. The modes corresponding to the filtering and beam scale are removed from the model before fitting to the real data.

4.5 Data

In order to estimate the mass of a cluster catalog, we need the cluster location and the CMB map corresponding to the cluster location. Both catalog and CMB map can come from the same experiment (for example SZ surveys) or from different experiments whose survey areas overlap. In our case we used data sets from two different experiments: CMB maps from South Pole Telescope explained in §4.5.1 and optical cluster catalog from Dark Energy Survey explained in §4.5.2

4.5.1 South Pole Telescope

South Pole Telescope (SPT) is a 10 meter diameter, wide field, offset Gregorian telescope (SPT, Carlstrom et al., 2011; Padin et al., 2008) located at the Amundsen-Scott South Pole station. The SPT has been operating since early 2007 and has completed two surveys so far: SPT-SZ (2007 -2011) and SPTpol (2012-2016). Extremely dry and stable atmosphere of the South Pole makes it one of the best available sites on Earth for observing at millimeter and sub-millimeter wavelengths.

SPTpol 500 deg^2 survey

SPT installed a polarisation sensitive camera, SPTpol, during the austral summer of 2011-2012. The SPTpol focal plane consists of 1536 polarization-sensitive transition edge sensor bolometers (360 at 95 GHz and 1176 at 150 GHz)(Austermann et al., 2012).The SPTpol surveyed 500 deg^2 of southern sky spanning fifteen degrees of declination, from -65 to -50 degrees, and four hours of right ascension, from 22h to 2h. In this section we briefly summarize the SPTpol observation strategy, map making, and beam characterization; we suggest interested reader to refer Henning et al. (2018) for further details.

In this work, we use CMB temperature maps from observations between April 2013 and September 2016 in the frequency bands centered at approximately 95 GHz and 150 GHz. Over this period, SPT used two different scanning strategies to observe the field. From April 2013 upto May 2014 SPT observed the field in lead-trail strategy and for the rest of the observation period SPT adopted full-field strategy. In lead trail strategy the field is split into two halves in right ascension - lead-field and trial-field. The lead-field is scanned first for a period of 2 hours, immediately followed by a 2 hour trail-field scan. During lead-trail strategy the scan speed and elevation steps are set such that the entire observation occurs over the same azimuth range. In order to increase sensitivity at large angular scales, SPT adopted full-field strategy for the rest of its observation period, where constant-elevation scans were made across the entire range of right ascension over 2 hour period.

The telescope beam and pointing solutions were characterized by observing Venus. SPTpol made seven observations of Venus. From these seven observations we calculate the 21 independent cross power spectra and take the average to characterize beam, B_l. The beam covariance is estimated as the noise variance of these 21 independent cross-spectra. Broadening of the beam is caused by two sources: rms pointing error and finite size of Venus. During the analysis it was found that broadening due to the finite size of Venus (which was ~ 11 arc seconds) is negligible. The final telescope beam along with the pointing jitter roughly corresponds to a $\theta_{\rm FWHM}$ = 1.′22 (1.′7) Gaussian for the 150 (95) GHz dataset.

The raw data is composed of digitised time-ordered data (TOD) for each detector that are converted into CMB temperature units. We bin the TOD

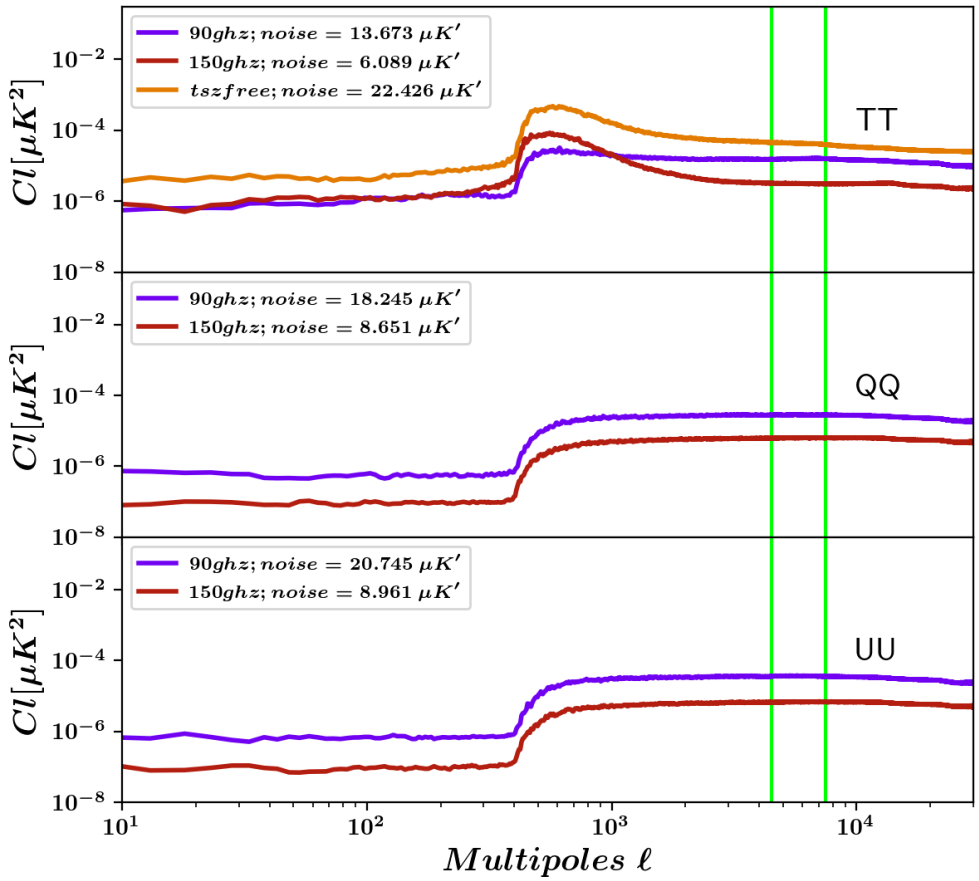

Figure 4.6: SPTpol noise power spectrum of temperature and polarisation maps. The vertical green solid lines are the multipole range across which the corresponding white noise level is calculated.

into two different maps using a flat-sky approximation in the Sanson-Flamsteed projection (Calabretta and Greisen, 2002; Schaffer et al., 2011). To construct the first map (lensing map), in which we aim to reconstruct the small-scale lensing signal ($L(\hat{n})$), we remove large-scale modes $\ell \leq 300$, bandpass filter the TOD in the range of approximately $300 \leq \ell_x \leq 20,000$, and bin them into $0.'5$ square pixels. For the second map (SPTPol SZ-free gradient map), intended for estimation of the large-scale CMB gradient ($G(\hat{n})$), we apply minimal TOD filtering by only removing modes below $\ell_x \leq 30$, and bin them into $3'$ square pixels. While we only use the data from the 150 GHz channel for the first map, the latter is a SZ

signal cleaned map produced by linearly combining the 95 and 150 GHz channels. We use this SZ-free map to reconstruct the background gradient of the CMB at the cluster locations. The minimal filtering on this map allows us to recover large-scale modes which indeed helps in a better estimation of the background gradient. The 0.′5 resolution of 150 GHz temperature map has a white noise level of $\Delta_{\rm T}$ = 6 μK′ estimated using a jackknife approach. The low-resolution SZ-free combination is noisier with $\Delta_{\rm T} \sim 22$ μK′ .

Fig. 4.6 shows the noise power spectrum of temperature and polarisation maps. Top panel in the figure represents the temperature noise power spectrum and the bottom two panels correspond to polarisation stokes Q and U maps. The purple and maroon curve in all the panels correspond to noise spectrum of 90 and 150 GHz channels respectively. The orange curve in the top panel represents the noise power spectrum of the tSZ-free maps obtained by using linear combination 90 and 150 GHz channels. In all the three panels the vertical green curves represent the multipole range across which the white noise level is calculated.

4.5.2 DES and the redMaPPer *catalog*

The Dark Energy Survey (DES) was a ~5000 deg^2, optical to near-infrared survey conducted using the Dark Energy Camera (Flaugher et al., 2015) mounted on the 4-meter Victor Blanco telescope at Cerro Tololo Observatory in Chile and has recently finished its survey. For this analysis, we use the cluster catalog obtained from the first three years of DES observations, which completely overlaps the SPTpol 500 deg^2 survey.

The cluster catalog was derived using the redMaPPer (RM) algorithm (Rykoff et al., 2014). RM is an optical cluster-finding algorithm which detects candidates by identifying over-densities of luminous red galaxies with luminosity greater than 20% of L_*. It is based on our understanding that galaxy clusters are agglomerations of galaxies containing old and subsequently red stars. The algorithm iteratively assigns membership and centering probabilities for each red galaxy identified as belonging to a cluster candidate. A weighted sum of the membership probabilities, richness λ, is assigned to each candidate. The centre comes from the galaxy with the highest centering probability. The DES RM catalog contains two samples: a flux-limited sample and a volume-limited sample. The flux-limited sample has more high-redshift clusters detected from deep fields in

the survey. On the other hand, the volume-limited sample is independent of survey depth, complete above a luminosity threshold (McClintock et al., 2018), and normally preferred for cosmological analysis. See Rykoff et al. (2016) for more information on the application of RM to the DES survey data.

The RM cluster catalog version employed in this analysis is Y3-gold (`y3_gold:v6.4.22`). The Year-3 gold catalogue is based on the previous catalog from the Year-1 data (Drlica-Wagner et al., 2018) with some updates as described in Morganson et al. (2018). The catalog contains 54,112 clusters above richness $\lambda \geq 20$ in the flux-limited sample and 21,094 clusters in the volume-limited sample. Of these, 5,828 (2,428) clusters from the flux(volume)-limited sample lie within the SPTpol 500 deg^2 survey in the redshift range $0.1 \leq z \leq 0.95$ (0.90). We additionally remove clusters near the survey edges with more than 5% masked pixels or within $10'$ distance from any bright ($\geq$ 6 mJy at 150 GHz) point sources detected in the SPTpol temperature map. These cuts leave 4,003 (1,741) clusters with $\lambda \geq 20$ from the flux(volume)-limited sample with a median redshift of $\tilde{z} = 0.77$ (0.48). The error in the cluster photo-z estimates are small with $\hat{\sigma}_z = 0.01(1+z)$ (Rozo et al., 2016).

4.6 Pipeline verification

In this section, we describe tests used to investigate the known and unknown systematic effects in the data and to validate the pipeline. We describe simulations used in 4.6.1 followed by the test for unknown systematics through the "curl" null test (§4.6.2). We then calculate the expected systematic error budget from known sources of systematic uncertainty (§4.6.3).

4.6.1 Simulations

In this section, we describe the simulations used for the pipeline validation. We calculate the large-scale structure lensed CMB power spectra for the fiducial Planck Collaboration et al. (2016b) cosmology using `CAMB` (Lewis et al., 2000) and create $300' \times 300'$ Gaussian realizations of the CMB temperature map with $0.'25$ pixel resolution.Given the small angular extent, these simulations are done in the flat-sky approximation. These simulations are then lensed using the simulated galaxy cluster convergence profiles from the next section. We next apply the frequency-dependent foreground realizations. The simulated maps are convolved by the beam functions, and are rebinned to $0.'5$ pixels to reduce the computational

requirements.

For realistic simulations, we must also account for the noise and the filtering applied to the real data. We add instrumental noise realizations corresponding to SPTpol maps (see §4.5.1). We follow Baxter et al. (2018) and other SPT works and approximate the map filtering using a function of the form:

$$F_{\bar{\ell}} = e^{-(\ell_1/|\bar{\ell}|)^6} e^{-(\ell_2/\ell_x)^6} e^{-(\ell_x/\ell_3)^6}. \tag{4.19}$$

We validate the robustness of this approximation in §4.6.3. For the small-scale lensing map, we set: $\ell_1 = 300$, $\ell_2 = 300$, and $\ell_3 = 20{,}000$. For the gradient map, we set: $\ell_1 = 0$ (as the gradient map does not have an isotropic filter), $\ell_2 = 30$, and $\ell_3 = 3000$.

4.6.2 "Curl" null test

We perform a "curl" null test (Hu et al., 2007) at 4003 cluster locations from the DES RM Year-3 flux-limited sample. Specifically, we replace the divergence of the gradient field, $\nabla \cdot [G(\hat{\mathbf{n}})L^*(\hat{\mathbf{n}})]$, in Eq. (4.10) with the curl operator. Since the curl of a gradient field is zero, the reconstructed field should be consistent with zero unless there is a systematic bias in the data. The result of the curl test is shown in Fig. 4.6.2. We radially bin the test results similar to the cluster stack as described in §4.4 and compare it to a null signal. The test returns a probability to exceed (PTE) value of 0.26 consistent with a null signal.

4.6.3 Systematic error budget

Now we quantify possible sources of systematic error. We estimate the bias due to each cluster's SZ emission and residual foregrounds, the assumption of an underlying cluster profile, uncertainties in the DES RM mis-centering parameter $f_{\rm mis}$, approximations to the filter transfer function (Eq. 4.19), uncertainties in the beam measurements, and the assumption of a background cosmology. Another source of systematic error is the uncertainties in the cluster redshifts estimated photometrically. However the impact of photo$-z$ errors was estimated to be negligible by Raghunathan et al. (2017), and we ignore them here.

We rely on the Sehgal et al. (2010) simulations to estimate the level of residual-SZ/foreground bias in the RM Year-3 flux-limited sample. In all the other cases we use the data and report the shift in the average lensing mass of the clusters in the RM Year-3 volume-limited sample obtained in §4.7. The combined systematic

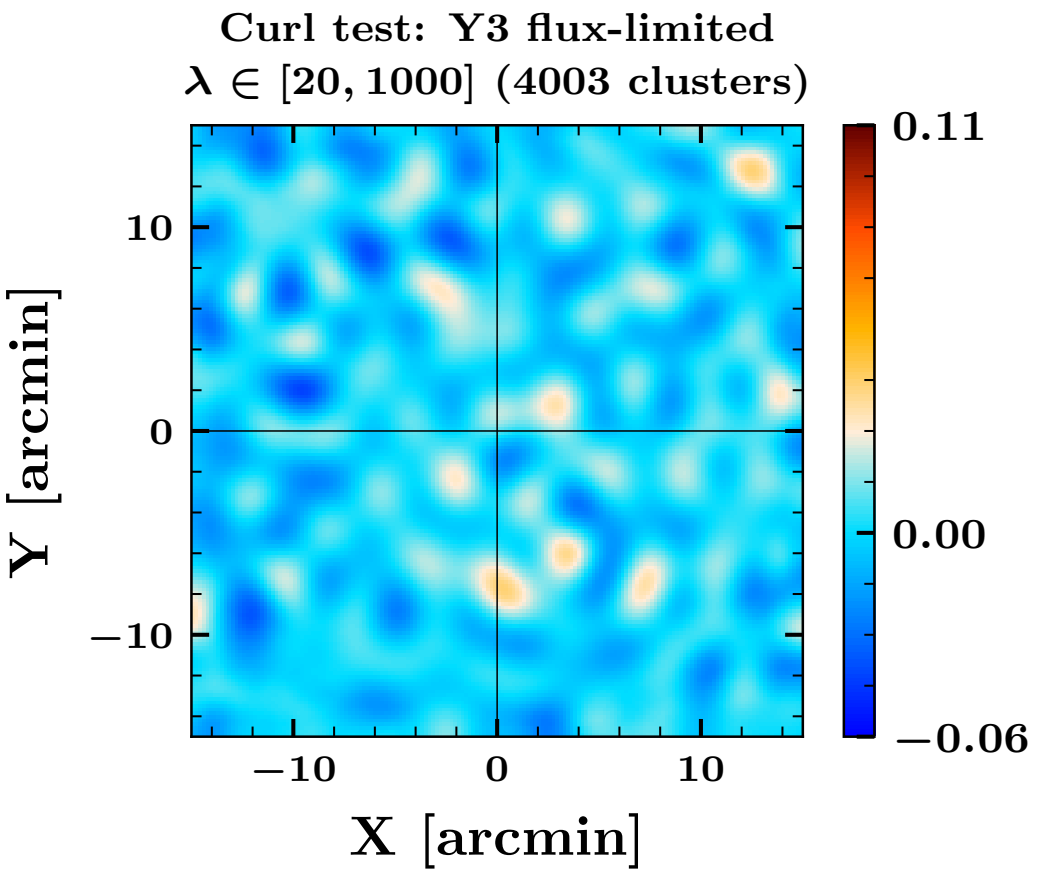

Figure 4.7: Stacked result of the curl test performed at the cluster locations by replacing the divergence operator in Eq. (4.10) with a curl operator. We obtain a PTE value of 0.26, consistent with a null result. For the ease of visual comparison we adopt the same colour scale as in Fig. 4.9.

error budget is presented in Table 4.1. The systematic error calculated as a quadrature sum of the errors presented in Table 4.1 is much smaller than the statistical error in the measurements at a level of 0.15σ. Using a direct sum, the combined error budget is 0.27σ. The dominant error comes from the uncertainty in the DES RM cluster centroids shifting the mean lensing mass by 2.8%.

Cluster SZ signal and residual foregrounds

In this work we eliminate the bias due to SZ signal in the reconstructed convergence maps using a SZ-free gradient map. However, projecting only the SZ signal out tends to modify other frequency-dependent foregrounds, and the resultant map is not an optimal foreground-free CMB map for the lensing reconstruction.

Table 4.1: Systematic error budget for DES RM volume-limited sample

Source of error	Magnitude of error	
	%	frac. of σ_{stat}
Beam uncertainties	$< 0.01\%$	-
Cluster mis-centering	2.78%	0.12σ
Cosmology	0.39%	0.03σ
Filtering ℓ_x	0.21%	0.02σ
Halo profile	0.12%	0.01σ
Residual foregrounds	2.12%	0.09σ
Total	3.53%	0.15σ

This enhancement of foregrounds generally acts as an additional source of noise and tends to increase the variance of the reconstructed convergence maps. At the cluster locations, however, an increase in foreground emission due to galaxies inside the cluster can introduce undesired mode coupling between the SZ-free gradient map and the lensing map resulting in a biased lensing signal. Here we quantify this bias using the Sehgal et al. (2010) foreground simulations.

To this end, we begin with the simulated skies described in §4.6.1, to which we then add simulated clusters, including the lensing signal (only the *1-halo* term), thermal and kinetic SZ effects, and emission associated with the cluster (e.g. from member galaxies). These simulations also include foregrounds uncorrelated with the clusters such as field radio galaxies. The foregrounds (cluster tSZ and kSZ, radio galaxies etc.,), unless specified otherwise, come from the Sehgal et al. (2010) simulations described below. Note that the foreground maps, whether associated with the cluster or not, are not lensed by the cluster in these simulations. We expect the lensing due to foregrounds is minimal and outside the scope this thesis. The number of simulated clusters and their redshifts and richnesses are derived from the DES RM Year-3 flux-limited sample. The richnesses and redshifts are converted to cluster masses according to the $M - \lambda$ relation (Eq. 4.21) with best-fit parameters from Melchior et al. (2017): $A_{\rm M17} = 2.35 \times 10^{14}\ M_\odot$, $\alpha_{\rm M17} = 1.12$, and $\beta_{M17} = 0.18$.

For foregrounds, we extract half-arcminute resolution $300' \times 300'$ cutouts of

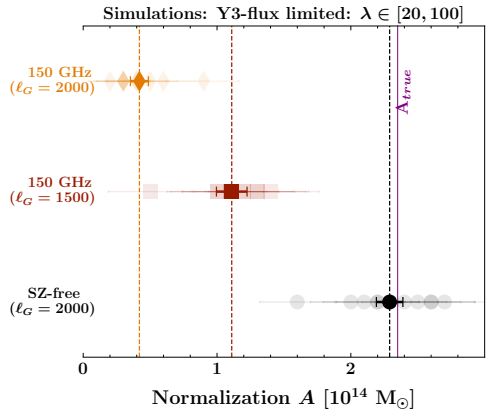

Figure 4.8: Quantifying the level of bias due to residual foregrounds and the SZ signal using Sehgal et al. (2010) simulations. The recovered lensing mass, unbiased for the fiducial case with SZ-free map for gradient estimation and l_G = 2000 is shown as black circles. The equivalent biased results with just the 150 GHz map and l_G = 1500(2000) cutoff scales for the gradient estimation are shown as red squares (orange diamonds). Each light shaded point corresponds to an individual simulation run with clusters from the DES RM Year-3 flux-limited sample. The darker data points are the values obtained for 10 × the sample size

the 95 and 150 GHz Sehgal et al. (2010) simulations of the SZ, kSZ, radio, and infrared galaxies around halos corresponding to the mock cluster sample. We scale the SZ power down from the Sehgal et al. (2010) simulations by a factor of 1.75 to match the George et al. (2015) measurements. These foreground cutouts are added to our mock galaxy cluster lensed CMB datasets. The maps are then processed in the same way as explained in §4.2 to extract the SZ cleaned map and passed into the mQE.

We present the results in Fig. 4.8. The true normalization is shown as the purple solid line. In the figure, the light shaded data points are the result for a single simulation run (~ 4000 clusters) and the darker data points are the results for 10× the sample size. We obtain $A = 2.30 \pm 0.09 \times 10^{14}\ M_\odot$ (black circle) implying no significant residual foreground bias in the lensing measurements. This result also provides evidence that the lensing pipeline is unbiased.

Comparison to standard QE: We also use the Sehgal et al. (2010) simulations to compare the modified QE to the standard case using the 150 GHz map for the background CMB gradient estimation. In the standard case, the correlations introduced between the two maps by the foregrounds, the SZ signal in particular, can be alleviated by lowering the LPF threshold $\ell_{\rm G}$ for the gradient map as in

Eq. (4.14). As described in §4.2, the choice of $\ell_{\rm G}$ is a trade-off between the level of foreground bias and the lensing S/N. Here we adopt $\ell_{\rm G} = 2000$ and $\ell_{\rm G} = 1500$ and note that the results are heavily biased in both cases: red squares (orange diamonds) for $\ell_{\rm G} = 1500$ ($\ell_{\rm G} = 2000$). The level of bias is higher when $\ell_{\rm G}$ is set to 2000 compared to 1500, as expected. This bias is predominantly due to the SZ signal and can be reduced by removing massive clusters from the analysis as in Baxter et al. (2018). For comparison, when we apply a richness cut of $\lambda \in [20, 40]$ the lensing bias is reduced from 82% to 65% for $\ell_{\rm G} = 2000$ and 52% to 35% for $\ell_{\rm G} = 1500$. This cut removes ~500 massive clusters from the analysis. This result can be compared to the conservative SZ-bias of 11% set by Baxter et al. (2018) with $\ell_{\rm G} = 1500$ for the same richness range $\lambda \in [20, 40]$. Baxter et al. (2018) obtained a lower bias value as the high-ℓ modes in the SPT-SZ maps are down-weighted due to 4× higher noise.

Finally, a subtle point from the figure is that the mass constraints obtained using the 150 GHz map for gradient estimation (orange diamonds) are better (~ 14%) than those obtained using the SZ-free map for gradient estimation (black circles) despite adopting $\ell_{\rm G} = 2000$ in both cases. This hit in the SNR arises because the SZ-free map is noisier than the 150 GHz.

Cluster profile

In our fiducial analysis, we assume that the underlying halo profile of the clusters follows the NFW dark matter model. However, the true profile of galaxy cluster may not follow the NFW model and indeed deviations from the NFW profile have been observed (Diemer and Kravtsov, 2014; Child et al., 2018).

In this section, we estimate the magnitude of a possible bias due to the assumption of the incorrect mass profile by using an Einasto profile (Einasto and Haud, 1989) to model the lensing convergence κ^{1h}. The Einasto profile is defined as

$$\rho(r)_{\rm Ein} \;=\; \rho_0 \, \exp\left(-\frac{2}{\alpha}\left[\left(\frac{r}{R_{\rm s}}\right)^{\alpha} - 1\right]\right), \tag{4.20}$$

where $\alpha = 0.18$ is the shape parameter (Ludlow et al., 2013). As in the NFW analysis, the concentration c_{200} as a function of mass and cluster redshift is obtained using the Duffy et al. (2008) relation. We use the general framework for spherically symmetric halos defined in the previous chapter 3 and simply plug

the above density profile into Eq. 3.10 to obtain the Einasto convergence $\kappa^{1h,\mathrm{Ein}}$ profiles. The κ^{2h} term remains the same. For the Einasto case we see a negligible shift of 0.01σ compared to our fiducial result.

Uncertainties in filter transfer function and beam

As described in §4.5, the SPTpol map-making process is lossy, with noisy modes along the scan direction filtered out. The ideal, if computationally expensive, approach to handle the filtering would be an end-to-end simulation from the TOD to the lensing reconstruction. In this work, we take a computationally much cheaper approach and approximate the filtering by the phenomenological fit to the filter transfer function in Fourier space given by Eq. (4.19). The major uncertainty is in the position of the high-pass filter (HPF) in the scan direction: this filters modes more strongly than the isotropic HPF, and the LPF is at angular scales that do not matter to the reconstruction. The estimated position for this HPF is $\ell_x = 300 \pm 20$. We also recompute the models for an assumed $\ell_x = 280$ and 320 to evaluate the shifts in the lensing masses. We note no significant effect (masses shift by roughly $\pm 0.02\sigma$), indicating that the uncertainty in the simplified filtering treatment causes negligible changes to our results.

Similarly, we also check the effect of errors in the telescope beam modeling B_ℓ that were derived using Venus observations (see §4.5.1). We find that the effect due to beam uncertainties in the final result is also negligible. The shift in the lensing mass is $\leq 0.01\sigma$ when we modify $B_\ell \to B_\ell + 2\sigma$.

Underlying cosmology

The systematic error arising due to the assumption of a background cosmology is quantified here. As described in earlier sections, in our fiducial analysis we use the ΛCDM cosmology obtained using the Planck Collaboration et al. (2016b) datasets. Here we repeat the analysis by modifying the lensed CMB power spectra C_ℓ to include the 1σ errors to the Planck Collaboration et al. (2016b) cosmological parameters. Modifying the background cosmology alters the weights of Eq. (4.14) in the lensing estimator and also the model convergence profiles $\kappa^{1h}(M, z)$ and $\kappa^{2h}(M, z)$. However, the effect due to background cosmology in the inferred lensing mass is negligible with a shift in the lensing mass $\leq 0.03\sigma$.

Uncertainties in $f_{\rm mis}$ parameter

In our baseline analysis we perform a mis-centering correction of the cluster convergence models (see §4.4) using $f_{\rm mis} = 0.22$ based on the results by Rykoff et al. (2016) for the RM clusters from the science verification data. Now we generate new convergence models assuming a larger fraction, 33%, of the clusters are mis-centered by modifying the mis-centering parameter by its 1σ error from Rykoff et al. (2016). Since the two parameters, $f_{\rm mis}$ and $c_{\rm mis}$, describing the cluster mis-centering are highly correlated, we also modify ln $c_{\rm mis}$ = -1.32 for this test.

The recovered mass increases by 2.8% in this case. However, the shift is only 0.12σ, $1/8^{th}$ of the statistical uncertainty. The direction of the shift is consistent with expectations, as assuming a larger $f_{\rm mis}$ should smear the convergence model more than the fiducial case leading to an increased lensing mass. Since this is the dominant systematic, we also estimate the error for the flux-limited sample. The mean lensing mass of the volume-limited sample goes up 3.2% but the change is still smaller than the statistical error (0.16σ).

4.7 Results and Discussion

The main results of this work are the lensing-derived cluster mass constraints for the DES RM Year-3 cluster samples using SPTpol SZ-free gradient maps × 150 GHz temperature maps. Below, we first present the lensing mass estimates in §4.7.1 and use the lensing measurements from the DES Year-3 volume-limited sample to independently calibrate the $M - \lambda$ relation of the cluster sample in §4.7.2.

4.7.1 Stacked mass measurements

In Fig. 4.9, we present the results of our stacked lensing measurements. The left (right) panel correspond to the convergence maps stacked at the location of clusters in the DES Year-3 flux(volume)-limited sample. The variance in the flux-limited sample is lower than the volume-limited sample because the flux-limited sample has twice as many objects. An estimate of the mean-field has been subtracted from the maps. We reject the null hypothesis of no lensing with a significance of 8.7σ for the flux-limited sample of 4003 clusters. The obtained S/N is consistent with our expectations from the simulations shown as lighter black circles in Fig. 4.8. For the smaller volume-limited sample, the no-lensing hypothesis is ruled out at 6.7σ. The radially binned convergence profiles that are

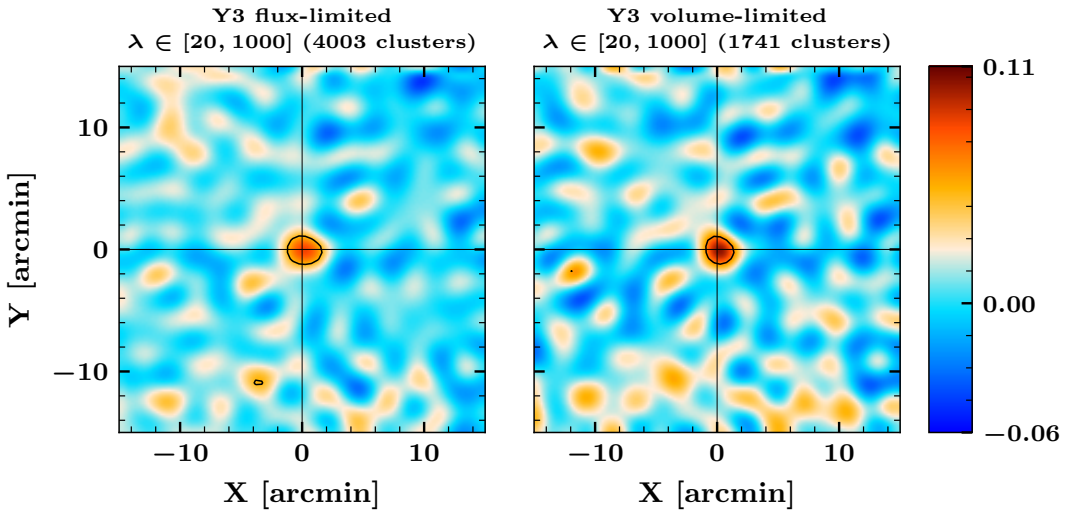

Figure 4.9: The inverse-variance weighted stacked convergence maps at the location of 4002 and 1741 clusters in the range $\lambda \in [20,1000]$ from flux limited (left) and the volume-limited (right) samples of the DES RM Year-3 cluster catalog. The contour corresponds to the regions above 3.5σ. The null hypothesis of no-lensing is rejected at 8.7σ and 6.7σ for the two cases respectively.

used to estimate the cluster masses are shown in Fig. 4.10 along with the best-fit model curves.

The ringing pattern is because of the sharp filtering of modes above the SPTpol beam scale. The error bars plotted are the square root of the diagonal entries of the covariance matrix estimated using Eq. (4.18). The recovered lensing masses for the stacked flux and volume-limited samples are $M_{200m} = 1.28^{+0.14}_{-0.18} \times 10^{14} M_\odot$ and $1.62^{+0.32}_{-0.25} \times 10^{14} M_\odot$ respectively. According to expectations, the lensing masses shift up by 0.3σ when the *2-halo* term is excluded.

A higher mean mass is expected for the volume-limited sample. At redshifts above $z \sim 0.6$, galaxies at the luminosity threshold adopted by RM become too faint to be detected in the DES data. Consequently, the richness of the clusters is extrapolated from the subset of galaxies that are sufficiently bright to be detected. This extrapolation introduces additional noise in the richness estimates. The increased scatter leads to more low-mass systems scattering up to apparently rich systems, thereby lowering the mean mass of the selected halos. For this reason, we restrict our analysis to the volume-limited sample in the subsequent sections.

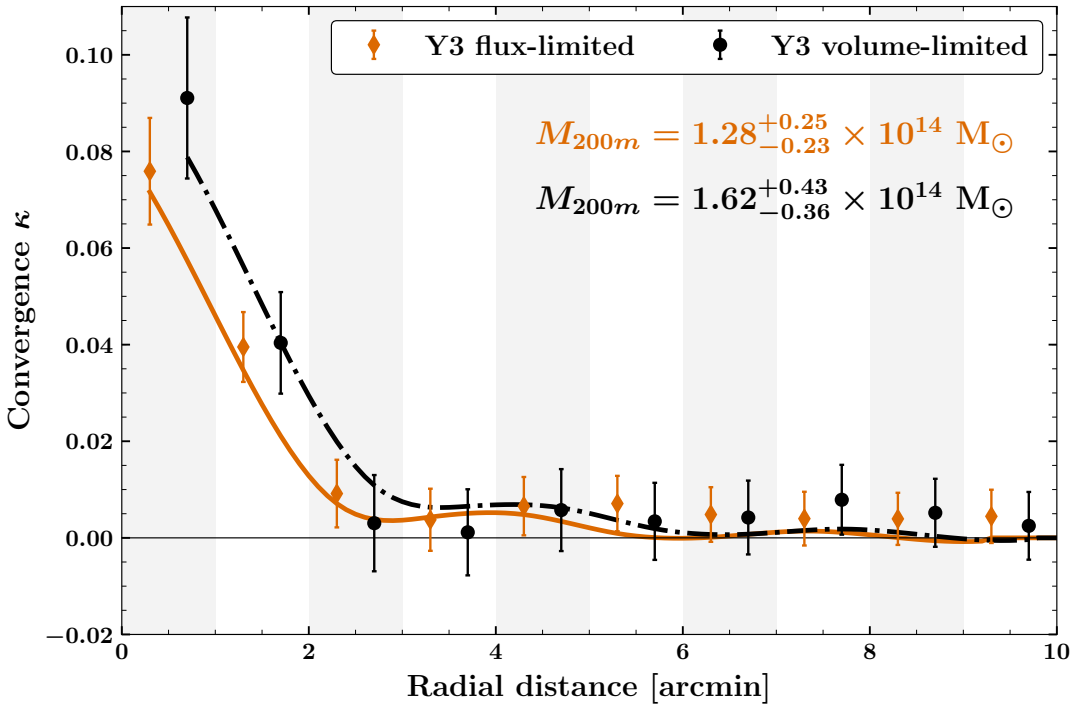

Figure 4.10: The azimuthally averaged radial profile of the stacked convergence maps from Fig. 4.9. The black circles and orange diamonds correspond to the flux and volume-limited Year-3 DES RM cluster samples. The error bars are the diagonal value of the covariance matrix estimated using the jackknife technique in Eq. 4.18. The data points for the two samples have been artificially shifted from the bin centres to avoid cluttering (orange diamonds are shifted to left and solid black circles to right).

4.7.2 Mass-richness $M - \lambda$ scaling relation calibration

We now apply the lensing mass measurements from §4.7.1 to constrain the relationship between a cluster's mass, M, and optical richness, λ, in the DES RM Year-3 volume-limited sample. We limit the analysis to just the volume-limited sample since the flux-limited sample has selection bias as explained previously in §4.7.1. Following earlier weak-lensing analyses of RM clusters (Simet et al., 2018; Melchior et al., 2017; McClintock et al., 2018), we use a power-law scaling relation for cluster mass, M, as a function of richness, λ, and redshift, z,

$$M = A\left(\frac{\lambda}{40}\right)^{\alpha}\left(\frac{1+z}{1+0.35}\right)^{\beta}, \tag{4.21}$$

where A is a normalization parameter, and the exponents α and β are richness and redshift evolution parameters respectively. The pivot points for the richness and redshift evolution parameters were set based on DES weak-lensing measurements of McClintock et al. (2018). The model for the stacked mass is

$$M(A, \alpha, \beta) \equiv M = \frac{\sum_j w_j M(\lambda_j, z_j)}{\sum_j w_j}, \tag{4.22}$$

where the sum runs over the number of clusters in the sample and the weight w for each cluster is given in Eq. (4.16).

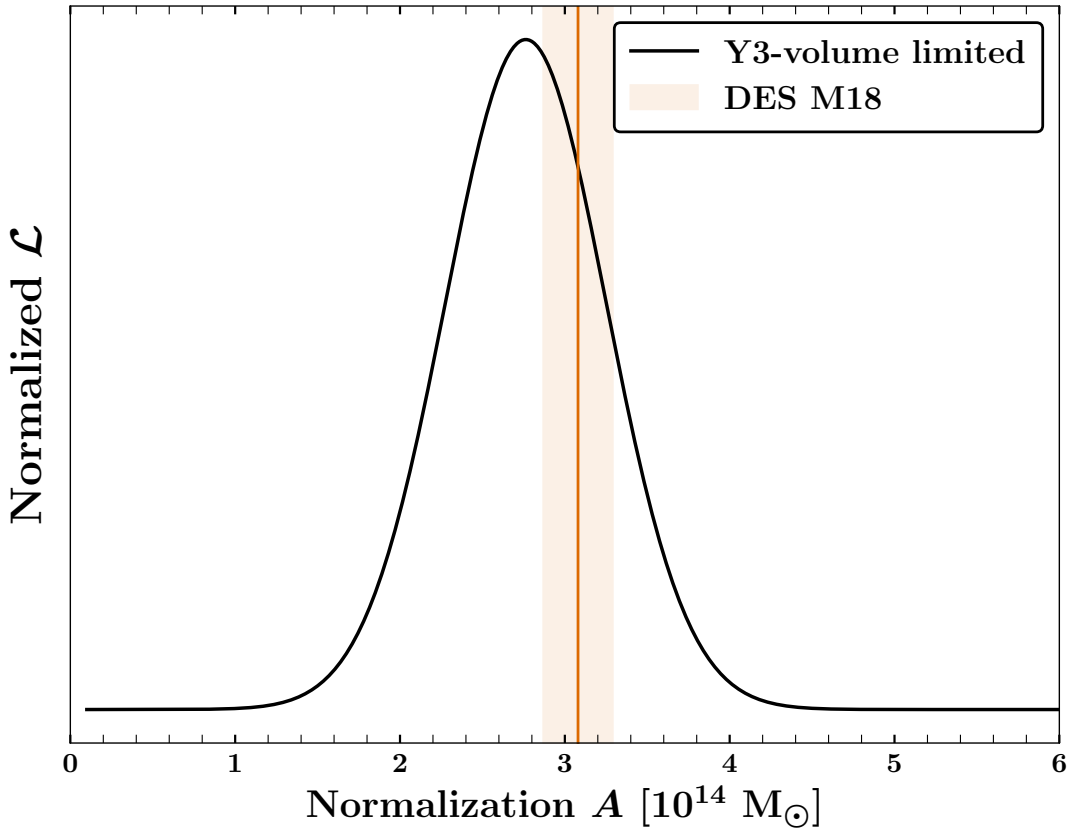

Figure 4.11: Marginalized posteriors of the normalization parameter A of the M-λ relation for the volume-limited sample of the RM cluster-catalog. The result is consistent with the best-fit values obtained by DES weak-lensing measurements McClintock et al. (2018), shown as the shaded region

We do not split the stacks into different richness or redshift bins. As a result, the data's sensitivity to the two evolution parameters is minimal and we apply informative priors to both. We perform a Markov chain Monte Carlo (MCMC)

analysis using the publicly available *emcee* (Foreman-Mackey et al., 2013) code to sample the likelihood space. We assume a flat prior for the normalization parameter A in the range $A \in [0.1, 100] \times 10^{14}\ M_\odot$. For the slopes, we use a Gaussian prior based on McClintock et al. (2018). Specifically, we set $(\alpha_0, \sigma_\alpha) = (1.356, 0.056)$ and $(\beta_0, \sigma_\beta) = (-0.3, 0.3)$. The posteriors on both the richness evolution parameters, as expected, follow the assumed prior. We obtain a normalization value of $A = 2.70^{+0.51}_{-0.50} \times 10^{14} M_\odot$, which is consistent with results from DES weak-lensing measurements of $A_{\rm DES} = 3.08 \pm 0.21 \times 10^{14}\ M_\odot$ by McClintock et al. (2018). The marginizalized posterior for A is shown as the black curve in Fig. 4.11 along with measurements from McClintock et al. (2018) as the orange shaded region.

4.8 Conclusions

In this chapter, we introduced the quadratic estimator which extracts CMB-cluster lensing signal by exploiting the correlation between the gradient map and lensing map. Though QE is just a first order approximation, it holds excellently well even in the strong lensing regime as CMB doesn't have structures at galaxy cluster angular scales. The SZ effect acts as a major source of systematic and statistical contaminant for CMB-cluster lensing analysis. We developed a modified QE to eliminate the SZ induced systematic bias. In the modified QE, the undesired SZ correlation between the gradient and the lensing map can be eliminated by using an SZ-free gradient map with only a slight decrease of SNR. Our pipeline returned unbiased results when tested using simulations.

We used our proposed method to constrain the mass of DES year-3 cluster catalog. The DES year-3 catalog consists of 4002 (1741) clusters in the full (volume) limited sample. We model the lensing convergence profile assuming a NFW profile and found the average mass of full (volume) limited cluster sample to be $M_{200m} = 1.28^{+0.14}_{-0.18}$ ($M_{200m} = 1.62^{+0.32}_{-0.25}$). In addition to that, we also reported several sources of systematics in Table 4.1 and found that all the systematics are much smaller than the statistical error.

Chapter 5

Template Fitting

The modified Quadratic Estimator (mQE) developed in the last chapter completely eliminates the thermal Sunyaev-Zel'dovich (SZ) bias by using a SZ free gradient map. Though SZ bias is removed in the mQE, SZ present in the lensing map induces extra variance in the reconstructed lensing convergence profile. Unlike the variance due to other sources (such as instrumental noise, uncorrelated foregrounds etc.,), SZ variance depends on the mass of the galaxy cluster. The SZ variance scales roughly with the mass of the cluster as $M^{3.33}$. For DES X SPT-pol clusters which we used in the previous chapter, we downweighed the massive clusters to take the SZ variance into account. This didn't have much effect on the final SNR as we had only few massive clusters. However, with future low noise CMB surveys such as SPT-3G, CMB-S4, Simons Observatory etc.,(Bender et al., 2018; CMB-S4 Collaboration et al., 2016; The Simons Observatory Collaboration et al., 2019) downweighing won't be an optimal solution.

This chapter is organised as follows: in §5.1 we explain the simulations used in this chapter. In §5.2, we describe the template fitting approach which will significantly reduce the SZ variance, followed by results in §5.3. We forecast mass uncertainties for future experiments using our new method in §5.4 and then we finally conclude in §5.5.

5.1 Simulations

We use simulations to validate our new method and also to forecast future experiments. We create $100' \times 100'$ unlensed Gaussian realizations of the *Planck* 2015 (Planck Collaboration et al., 2016b) best-fit lensed CMB power spectrum obtained from CAMB[1] (Lewis et al., 2000) (as explained in chapter 3). These maps are then lensed by the cluster convergence profile (see §3.1). We add simulated SZ emission (§5.1.1) and then convolve the map by the assumed instrumental beam. We take the instrumental beam to be a Gaussian with a FWHM = $1'.7$ at

[1] `https://camb.info/`

95 GHz and = 1′.0 at 150 GHz. Finally, we add Gaussian realizations of white noise at the specified noise level.

5.1.1 thermal Sunyaev-Zel'dovich signal

Unless otherwise noted, we assume the SZ emission is described by a radially-symmetric Arnaud profile (Arnaud et al., 2010) expected for a cluster of the specified mass and redshift. We do test the robustness of this assumption in §5.3.1 by using two sets of realistic SZ simulations from Sehgal et al. (2010) and Takahashi et al. (2017). The SZ power in the (Sehgal et al., 2010) simulations is scaled down by a factor of 1.75 to better match the measured SZ power in George et al. (2015); the Takahashi et al. (2017) simulations post-date the SZ measurements and are not rescaled. Extracting the appropriate SZ signal from these simulations requires selecting matching galaxy clusters, with a tradeoff between the number of matching clusters in the simulations and the fidelity of the match. We randomly select halos which are within 5% of the desired mass and ±0.2 of the desired redshift.

5.2 Method

In this section, we present a template fitting approach designed to reduce the SZ variance for massive galaxy clusters or for low noise surveys. We also discuss sources of uncertainties present in the CMB-cluster lensing analysis.

5.2.1 Template fitting to reduce the SZ variance

An obvious way to eliminate the SZ variance is by using SZ-free maps for both the lensing and gradient maps. Of course this would undo the advantages of the modified QE for the instrumental noise in the lensing map. One can also reduce this extra variance by projecting out a model template for the SZ signal, and thereby reducing the total amount of SZ power in the lensing map. Given the impossibility in creating a 'perfect' SZ template, the template fitting will not completely eliminate the SZ signal in the lensing map. However, template fitting can significantly reduce the SZ power in the lensing map, and thus reduce the SZ noise penalty on the lensing mass reconstruction.

To be unbiased, we must fit the template to a CMB-subtracted map or account for the information loss from template projection in the normalization factor A_l of Eqn. 4.10. The latter tact (correcting A_l) might have advantages if one needed

to suppress multiple kinds of cluster emission, e.g., dusty and radio galaxies in addition to the thermal SZ effect. Projecting a template from the Compton-y map will not help these other cluster signals. However, we expect these other signals to be small compared to the SZ flux for massive galaxy clusters [2]. In this work, we take the first approach and fit the template to a Compton-y map created from a linear combination of 95 and 150 GHz maps. Effectively, we have used the different spectral dependence of the SZ and CMB to eliminate the CMB, and thus any correlation between the removed template and the lensing dipole in the CMB map.

We choose to use a radially symmetric template at the fixed cluster location in this work. Unless otherwise noted, we assume the beam to be a Gaussian with FWHM = $1'$ at 150 GHz and $1'.7$ at 95 GHz. As this beam size is significantly large compared to the actual size of clusters at $z > 0.3$, clusters are approaching the effective point source limit where the specific details of their shape would not matter. Thus we choose to use a simple Gaussian template as the baseline template in this work. We also compare the results to template fitting with more physically motivated Arnaud profile (Arnaud et al., 2010), convolved by the experimental Gaussian beam. The residuals of removing a $2'.0$ FWHM Gaussian from an Arnaud profile convolved by a $1'.7$ beam are illustrated in Fig. 5.1. As argued above, the Gaussian template significantly reduces the SZ signal despite the mismatch between the assumed profile and input SZ model. While there should be small variations in the typical size of the cluster's SZ emission with mass and redshift, we neglect these variations and fix the size of the templates based on the expected median mass and redshift of the sample. One could easily adjust the template based on individual cluster redshift for a minimal increase in complexity.

As SZ and CMB have different frequency dependence, we use linear combination of 95 GHz and 150 GHz channels to obtain Compton-y maps. We then pull out a central $10' \times 10'$ cutout at the cluster location for fitting the template. Since the SZ emission is concentrated within a few arcminutes of the cluster center, there is little reason to fit over a larger area. We allow for two free parameters in the fitting: the overall amplitude of the template, and a constant DC background

[2] While the statement is generally true, it is important to note that in some low redshift clusters radio emission from the AGN core can be much larger than the SZ signal and CIB may be significant for some high redshift clusters.

level. We include the DC term while fitting the template amplitude, however, we do not subtract DC level. Only the template is subtracted from the lensing map.

With template fitting included, the Fourier transforms of the two maps used by the quadratic estimator can be written down as:

$$G_\ell = i\ell W_\ell^G T_\ell^{\rm SZ-free} \quad (5.1)$$

$$L_\ell = W_\ell^L \left(T_\ell - T_\ell^{\rm SZ-template}\right) \quad (5.2)$$

where, G_ℓ is the large-scale gradient map and L_ℓ is the lensing map. W_l^G and W_l^L are the Wiener filters to maximize the lensing signal Hu et al. (2007). The mm-wave map is T_ℓ while the constructed SZ-free map is $T_\ell^{\rm SZ-free}$. Compared to the modified QE (Madhavacheril and Hill, 2018; Raghunathan et al., 2019a), the new element is the $T_\ell^{\rm SZ-template}$ term representing the SZ template fit.

5.2.2 Sources of uncertainty in the CMB-Cluster Lensing Measurement

Template fitting is intended to reduce the SZ variance, however it will not suppress other sources of uncertainty such as instrumental noise, CMB sample variance and foreground emission. Thus it will be useful to look at the relative magnitudes of these two terms, the SZ variance (σ_{SZ}^2) and the non-SZ variance (σ_κ^2), when interpreting the performance of template fitting in the next section.

The non-SZ variance or kappa variance depends on the survey parameters (i.e. instrumental noise, and the degree to which foregrounds are cleaned) but is independent of the cluster properties. We estimate the non-SZ variance, σ_κ^2, using simulations of the CMB plus instrumental noise. Given the goal, we do not include the cluster's SZ emission. We apply the lensing pipeline to the simulated skies to estimate the convergence maps. We fit the convergence map to determine a mass, and take the scatter in these inferred masses over 1000 simulations to be σ_κ.

In contrast, the SZ variance should increase with cluster mass, M, roughly as $\sigma_{sz}^2 \propto M^{10/3}$, while being independent of the survey parameters. We estimate the SZ variance using the same suite of simulations, however now adding the cluster's SZ emission to the lensing map. We continue using an SZ-free map for other leg of the QE, the large-scale gradient map. As before, we estimate the convergence maps, fit for masses and take the scatter in these inferred masses to estimate σ_{SZ}^2

$+ \sigma^2_\kappa$.

We present the ratio of the SZ to non-SZ variances, $\sigma^2_{SZ}/\sigma^2_\kappa$, as a function of survey noise level and cluster mass in Fig. 5.2. As expected, the ratio increases with mass at any given noise level. The black solid curve represents a ratio of unity when the SZ variance equals the non-SZ variance. We expect template fitting to significantly improve the mass uncertainties only for clusters above the black curve.

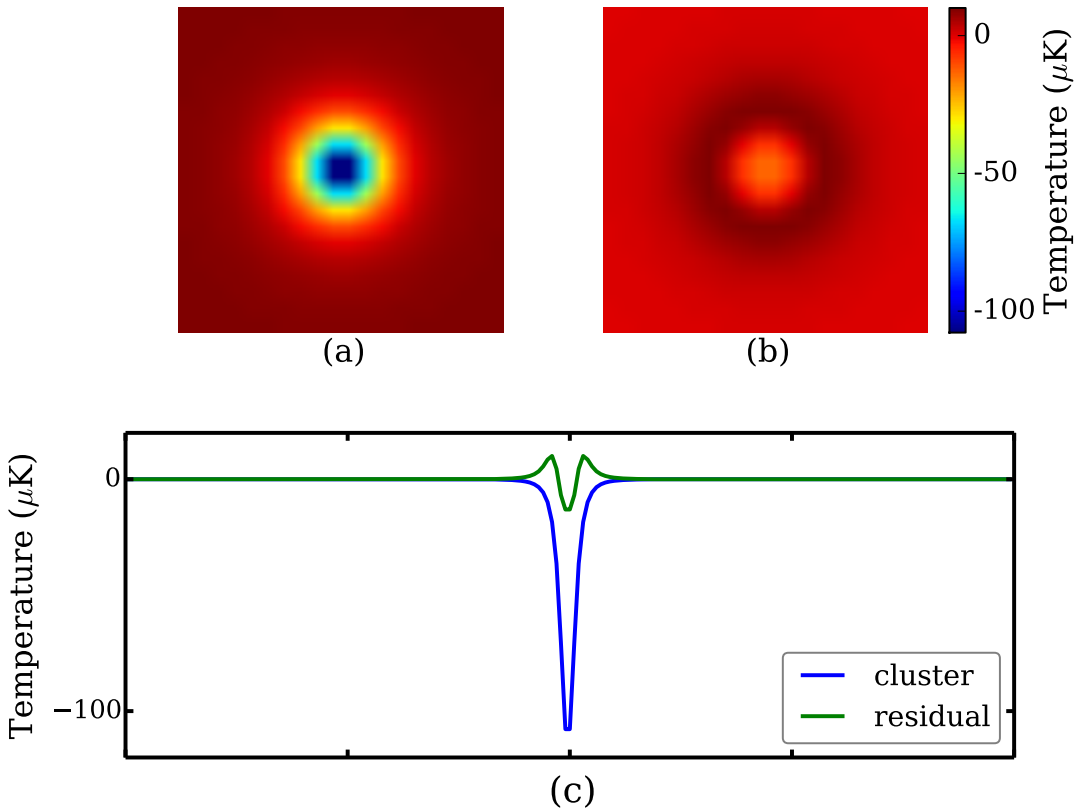

Figure 5.1: Template fitting significantly reduces SZ power, even with an imperfect match between the template and true SZ signal. The top left panel (a) shows the expected Arnaud profile for a galaxy cluster of mass $M_{200m} = 5 \times 10^{14}\ M_{\odot}$ at z=0.7 after being smoothed by Gaussian beam with FWHM= $1'.7$. The top right panel (b) shows the residuals after subtracting the best-fit $2'.0$ FWHM Gaussian (the amplitude is free, but the FWHM is fixed). The lower panel (c) shows one-dimensional slices through each panel: the solid blue line is a slice through the beam-convolved Arnaud profile of (a), and the dashed green line is a slice through the residual map in (b).

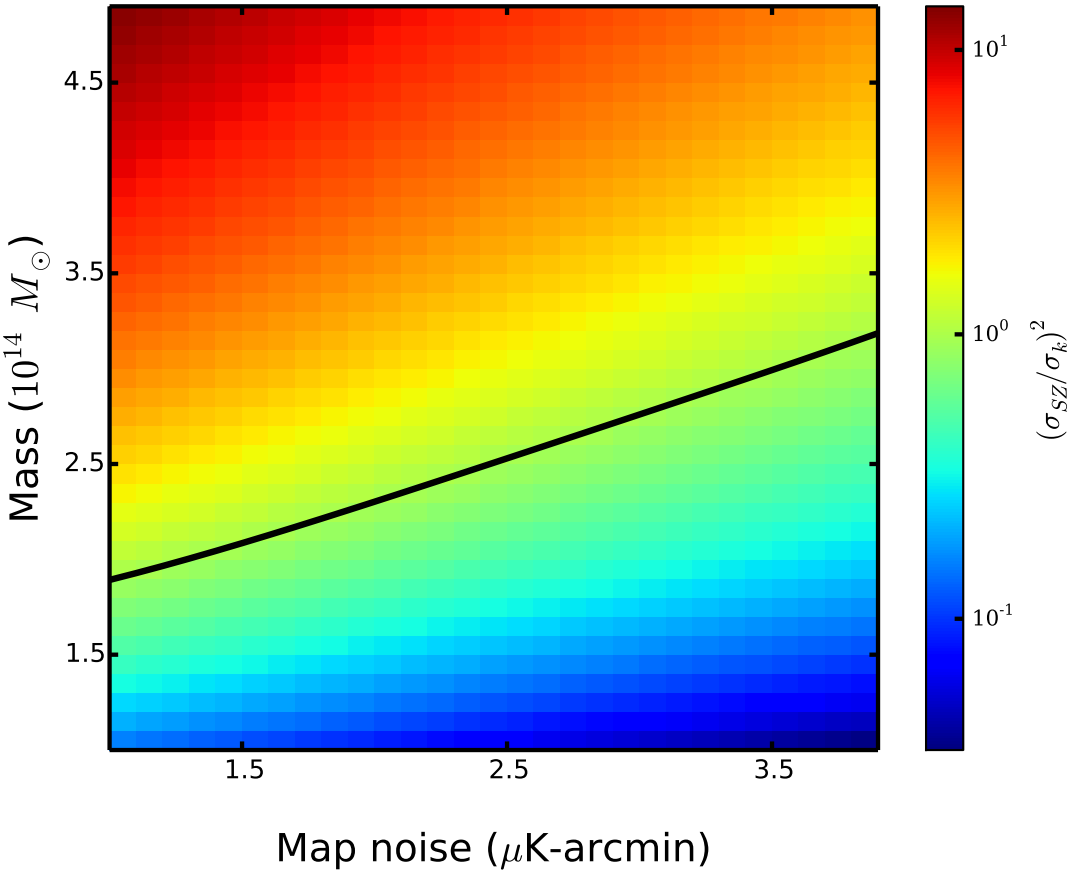

Figure 5.2: Ratio of SZ variance over kappa variance as a function of cluster mass and experimental noise level. As expected the ratio increases with mass for a given experimental noise level. The black solid line represents the points where the SZ variance is equal to the non-SZ variance.

5.3 Results

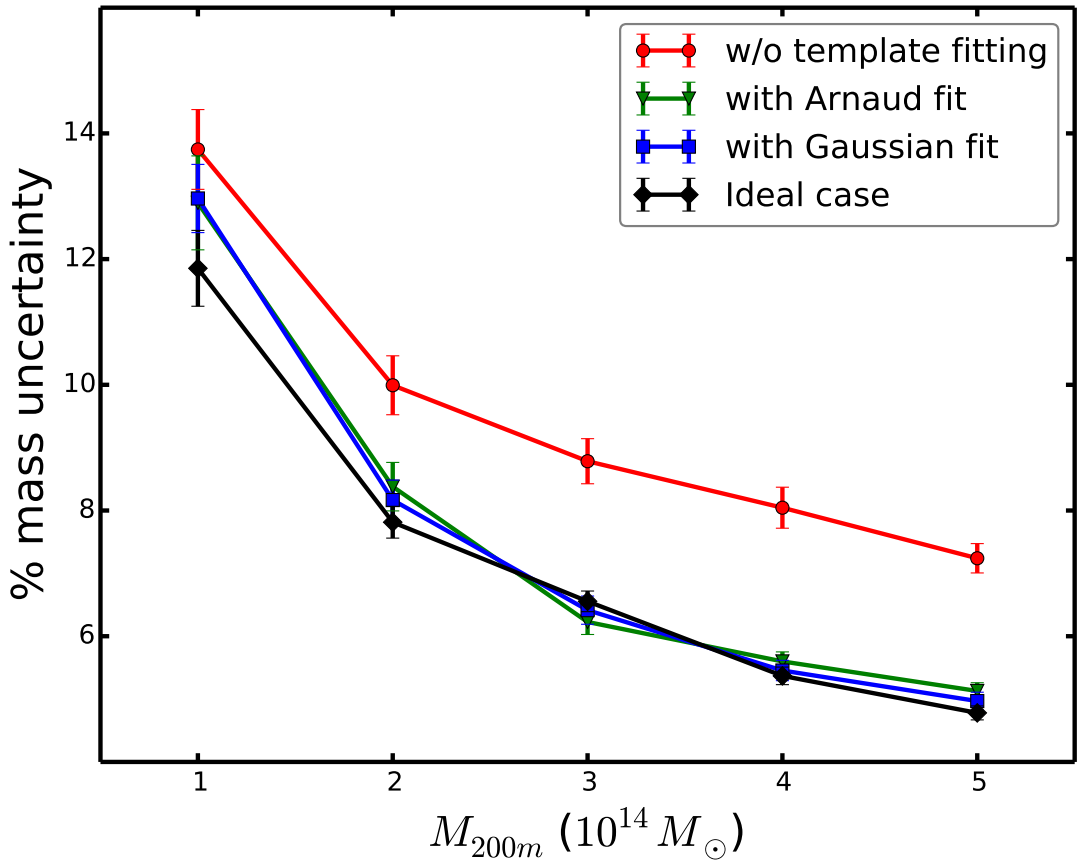

Figure 5.3: Projecting out an SZ template from the second leg o the modified QE improves the performance for all masses considered. Here we show the percentage mass uncertainties from three methods for a sample of 1000 clusters at a experimental noise level of 3 μK-arcmin. All the curves use an SZ-free map for the gradient, but make different assumptions about the second, lensing filtered map.

As shown in Fig. 5.3, we find that template fitting leads to a significant improvement in the final mass uncertainties for CMB-cluster lensing. For high-mass clusters, template fitting does nearly as well as in the idealized (non-physical) limit of having no SZ emission. In this figure, we are assuming an SPT-3G like experiment with FWHM of 1′ and 1.7′ at 150 GHz and 95 GHz respectively and a survey noise level of 3 μK-arcmin. We compare four algorithms to estimate cluster masses. In all cases we use a SZ-free gradient map (from a linear combination of 95 and 150 GHz maps). First, the red solid line shows the performance

of the original modified QE without template fitting, where we have used SZ-free gradient map and 150GHz map with Arnaud SZ for the lensing map. The second, black solid line shows the results for an idealized case, where we use a 150 GHz map without SZ for the lensing map. While this assumption is unphysical since there will be SZ emission at 150 GHz, it is useful as a representation of the performance limit for perfect SZ subtraction. Note that the relative performance improvement between the idealized and baseline case increases with mass as expected. For these survey parameters, the idealized case has 17% smaller uncertainties than the baseline for clusters of mass $1 \times 10^{14}\, M_\odot$ and 50% smaller for cluster masses of $5 \times 10^{14}\, M_\odot$. Template fitting recovers nearly all of this gain for high-mass clusters, as shown by the green triangles and blue squares (we have introduced an offset along mass axis for clarity). The two lines reflect different templates for subtraction. The green triangle shows the performance of projecting out an Arnaud SZ template from the lensing map. The blue square shows the results when using a Gaussian template instead, which is slightly mismatched to the assumed SZ signal. There is no practical performance difference between the two templates. For these assumed survey parameters, both templates are essentially indistinguishable from the idealized perfect SZ removal case at masses above $2 \times 10^{14}\, M_\odot$. Template fitting does not do as well at lower masses. This can be understood by considering the zero-mass limit – where one tries to remove the SZ template from a map without SZ emission. The noisy estimate of the SZ template amplitude will set a non-zero, effective floor to the apparent SZ-like signal in this map. In the low-mass limit, SZ template removal will thus perform more poorly than the original estimator. The first signs of this transition can be seen in Fig. 5.3 when comparing the performance at $M_{200m} = 2 \times 10^{14}\, M_\odot$ to $1 \times 10^{14}\, M_\odot$.

5.3.1 Robustness of template fitting method

As shown in the last section, the refinement to the modified QE improves the fractional mass uncertainties significantly (above a mass threshold that depends on the survey noise) for the symmetric Arnaud profile. However, the question remains as to whether this improvement will continue with the more complex real SZ emission of galaxy clusters along with any other haloes along the line-of-sight. To test this, we turn to the SZ simulations of Sehgal et al. (2010); Takahashi et al. (2017). As noted in §5.1.1, we draw SZ maps from these sims centered at

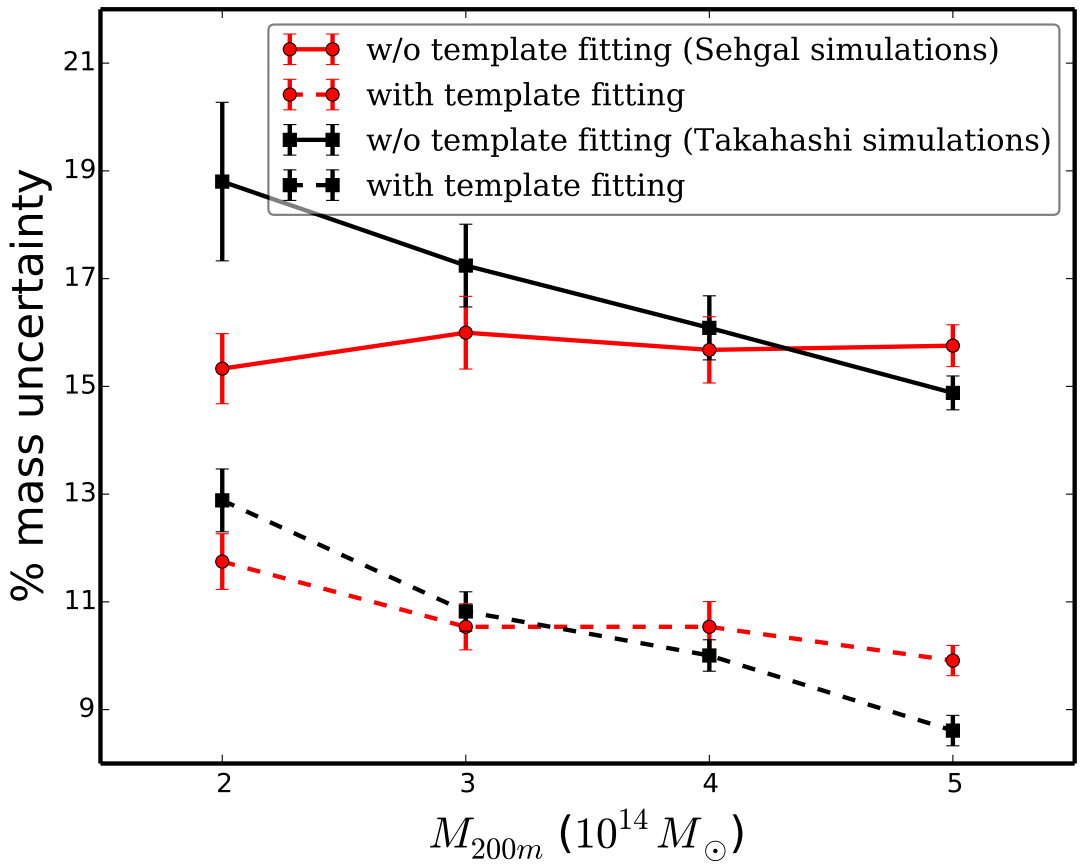

Figure 5.4: Our new method is robust to realistic SZ simulations. The red and black solid curves show the performance of modified QE for the Sehgal and Takahashi simulations respectively for a sample of 1000 clusters. The dashed lines show the improvement in each case when template fitting is used to reduce the SZ variance in the lensing map. The plotted uncertainties are for a stack of 1000 galaxy clusters of the quoted mass at $z = 0.7$.

the locations of similarly massed haloes. The results for these sims are shown in Fig. 5.4 for Gaussian template fitting. We have tested using both the Gaussian and Arnaud template fitting, and have found no appreciable difference. Red lines are for the Sehgal simulations and black lines for the Takahashi simulations. The solid lines are without template fitting, while the dashed lines show the improvement from template fitting in each case. The apparent flattening of the red curve is due the limited number of higher mass clusters in the Sehgal simulation. In this case of realistic SZ signals, however, we note that the performance is not equivalent to the idealized case presented as black solid curve in Fig. 5.3. This is due to the residual SZ signals in the map coming from the template mismatch,

for example fitting a spherically symmetric template does not account for the cluster asphericity [3]. In addition, the SZ signal from adjacent halos which we do not attempt to remove will also result in additional variance.

5.4 Forecasts

We now consider the impact of this method on the performance of upcoming CMB surveys, SPT-3G (Bender et al., 2018), SO (The Simons Observatory Collaboration et al., 2019) and CMB-S4 (CMB-S4 Collaboration et al., 2016). For the latter two experiments, we only consider the large-aperture telescopes (LAT) with an experimental beam of $\theta_{\rm FWHM} = 1.'4$ at 150 GHz and covering 40% of the sky (see also Table 5.1). For SPT-3G, we assume a survey area of $1500\,{\rm deg}^2$ and an experimental beam of $\theta_{\rm FWHM} = 1.'2$ at 150 GHz. We create a single cluster catalog realization for each experiment based on the noise levels at 150 GHz. Note that for simplicity, we make no attempt to use frequency information to remove other temperature foreground signals such as the the CIB, nor to improve the noise level on the Compton-y map. These assumptions are likely to mean that the simulated cluster list is conservative since we are not taking advantage of the multiple frequency bands in each of these experiments.

The three simulated cluster sample and assumed experimental parameters are passed through the cluster-lensing pipeline to estimate the mass uncertainty from CMB-cluster lensing on each stacked sample. For forecasts we picks SZ profiles from Takahashi et al. (2017) simulations and as mentioned before we randomly pick all the halos which fall within 5% of the desired mass and ±0.2 of the desired redshift. The results are given in Table 5.1. We find that template fitting can reduce the percentage mass uncertainty for SPT-3G, SO and CMB-S4 by 28%, 25% and 30% respectively.

[3] By allowing more morphological freedom to the template might reduce this variance.

Table 5.1: Forecasted mass uncertainties for SPT-3G, SO and CMB-S4 with the modified QE before and after removing the estimated SZ template.

Exp.	Δ_T [$\mu K'$]	$N_{\rm clus}$	$\Delta M/M$ [%]	
			No template fitting	With template fitting
SPT-3G	2.2	2,400	11.10	8.00
SO-LAT	6.0	27,000	2.82	2.12
CMB-S4	1.73	75,000	1.92	1.33

5.5 Discussion and Conclusion

We have presented an improved version of the QE to estimate galaxy cluster masses through CMB lensing. By projecting out an SZ template from the lensing map of the QE, the algorithm substantially reduces the variance due to a cluster's own SZ emission. The SZ variance can be significant fraction of the total variance for high-mass clusters or low-noise surveys. Note that in the opposite limit of low masses or high noise (i.e. when the SZ variance is negligible), this template fitting may slightly reduce the overall S/N.

While the performance of the template fitting does depend on the fidelity with which the template accurately represents the true SZ signal, these variations do not seem to be a significant issue. In part this is because upcoming CMB experiments will not have sufficient angular resolution to resolve most of the structure in the SZ emission; the instrumental beam at 150 GHz for a 6-meter telescope is slightly larger than a typical high-redshift cluster. For mock SZ signals modeled using Arnaud profile, we find that the template removal approach reduces all of the additional variance due to the SZ signal. The improvement is not 100% for realistic SZ signals (Sehgal et al., 2010; Takahashi et al., 2017) because of the SZ emission from the adjacent haloes along the line-of-sight that we do not attempt to remove.

The method presented in this work is not limited to the cluster lensing. For example, Madhavacheril and Hill (2018) demonstrated that the modified QE can also be employed to CMB lensing in general. However, as shown here the thermal SZ signal from clusters detected at high S/N adds extra variance in the reconstructed lensing maps. By using template fitting approach we reduced the variance significantly. In future CMB lensing work, we can use the template fitting approach instead of masking the massive galaxy clusters.

CMB-cluster lensing will be a key tool for galaxy cluster cosmology at high redshifts, while also providing a cross-check of optical weak lensing mass estimates at lower redshifts. For future surveys like CMB-S4 and Simons Observatory and for clusters above masses of $4 \times 10^{14}\, M_{\odot}$, we find that template fitting yields a factor of 1.4 reduction in the mass uncertainties. These results will help us in the quest to understand dark energy and the accelerating expansion of the Universe.

Chapter 6

Discussions & Future Work

The number density of galaxy clusters as a function of mass and redshift is highly sensitive to the underlying cosmology. However, cluster cosmology is currently limited by uncertainty in the cluster mass estimation. The upcoming optical, X-ray, and SZ surveys are expected to detect tens or even hundreds of thousands of galaxy clusters (LSST Science Collaboration et al., 2009; CMB-S4 Collaboration et al., 2016; Merloni et al., 2012; Refregier et al., 2010). A robust cluster mass estimation is essential in order to fully realise the potential of these cluster catalogs. CMB-cluster lensing offers one of the robust ways to accurately measure the masses of galaxy clusters, especially for clusters at high redshift ($z > 1$).

The main projects I worked during my thesis have been discussed in chapters (3,4, and, 5). In this chapter, I summarise the main findings of my thesis in §6.1. In §6.2, and §6.3 I briefly discuss other CMB-cluster lensing projects I was actively involved in and provide the status of my current project in §6.4. Finally, I will consider directions for future work in §6.5.

6.1 Summary

In chapter 3, we developed the Maximum Likelihood Estimator (MLE) approach, an optimal way to extract cluster lensing information from the temperature and polarisation maps of the CMB. We found that MLE outperforms the Quadratic Estimator (QE) by a factor of 2 for future low noise surveys in the absence of astrophysical foregrounds. The polarsiation EB and QU estimators perform identically. While astrophysical foregrounds affect the temperature MLE and set an effective noise of few μK, the polarisation estimator is negligibly affected as foregrounds are only partially polarised. We also quantified serval sources of systematics that affect the CMB cluster lensing in Table. 3.1. Cluster's own SZ signals, the tSZ and the kSZ induce significant statistical and systematic uncertainties on the temperature MLE. The tSZ signal is an order of magnitude greater than lensing signal. We can fit a model to the tSZ signal, however, even

a percent level misestimation of the tSZ model will result in 6% bias. Another way to tackle tSZ bias is to exploit the spectral dependence of tSZ signal. While a prefect knowledge of relative frequency calibration will eliminate tSZ bias, but it degrades the SNR by a factor of three (Baxter et al., 2015). In chapters 4 and 5 we modify QE to eliminate tSZ systematic uncertainty and significantly reduce the tSZ statistical variance respectively.

We modified the quadratic estimator (mQE) in chapter 4 to eliminate tSZ bias with negligible decrease in SNR. The QE exploits the correlation between the gradient map and the lensing map to extract cluster lensing signal. Any foreground present in both the maps will result in undesired correlation inducing a bias. By using tSZ free gradient map we largely eliminated the tSZ induced systematic bias with only a slight decrease of SNR. We used the mQE to constrain the mass of DES year-3 clusters using SPTpol CMB temperature maps. In addition to that we also constrained the normalisation parameter of optical richness-mass scaling relation at 17% level. The constraint is in good agreement with the corresponding optical weak lensing analysis.

While mQE eliminates the tSZ systematic uncertainty, the tSZ power present in the small scale lensing map of mQE induces extra variance in the lensing analysis. Unlike experimental noise and other uncorrelated foregrounds, tSZ induced variance is a function of mass. The tSZ induced statistical uncertainty scales with mass as $\approx M^{5/3}$. Although at current experimental noise levels the SZ induced statistical uncertainty is not significant, it will be a major source of contamination for future low noise surveys as shown in Fig. 5.2. We showed in 5.3 that by subtracting out a SZ template from the lensing map of mQE we can significantly reduce its variance. In addition to eliminating the tSZ induced bias our template fitting approach also significantly reduces the tSZ induced variance.

6.2 Polarisation detection

While the cluster lensing signal has been detected in CMB temperature data by many experiments (Baxter et al., 2015; Raghunathan et al., 2019a; Geach and Peacock, 2017; Baxter et al., 2018), the cluster lensing signal in CMB polarisation maps has been detected only recently by Raghunathan et al. (2019b). As a second author this publication, I worked on the pipeline to extract the CMB-cluster lensing signal and also wrote the draft of the paper. The cluster lensing signal is weaker in polarisation than temperature. However, the astrophysical

foregrounds that significantly affect temperature and have negligible effect on polarisation channel. The lensing SNR in polarisation is weaker compared to its temperature counter part at the present experimental noise level. However, as shown in Fig. 3.3, the foregrounds set an effective floor for CMB temperature estimator. As forecasts in Table 3.2 show, we expect the polarisation estimator to have comparable performance with that of temperature estimator for proposed CMB-S4 Collaboration et al. (2016).

In Raghunathan et al. (2019b), we report the first detection of cluster lensing signal in CMB polarisation data at 4.8σ significance. We used CMB polarisation QU maps from SPTPol 500 deg^2 survey and galaxy cluster catalog from DES year-3. The overlap of SPTpol and DES year-3 roughly has 18,000 clusters above a richness of $\lambda > 10$. Our detection in polarisation is a first key step for cluster cosmology with future low-noise CMB surveys, like CMB-S4, for which CMB polarisation will be the primary channel for cluster lensing measurements.

6.3 Inpainting approach

The cluster's own SZ signals, the tSZ and the kSZ, act as major sources of contamination when estimating the cluster mass using CMB temperature data. While we can eliminate the tSZ systematic uncertainty by using tSZ-free gradient maps as we saw in §4.2, the kSZ signal cannot be eliminated by using linear combination of different frequency channels as the kSZ and CMB have same spectral dependence.

As shown in §3.4.5, the kSZ effect induces significant bias on the the lensing analysis if not considered. In Raghunathan et al. (2019c) we modified the quadratic estimator in order to eliminate both tSZ and kSZ induced systematic biases. Using tSZ-free gradient map largely eliminates the tSZ bias, however, kSZ is still present in the gradient map. The correlation between the gradient map and the lensing map due to the presence of kSZ signal in both will induce a small bias in the reconstructed convergence maps. Both tSZ and kSZ signals span a radial range of the order of couple of arc minutes from the cluster center. We can construct the gradient map by interpolating the pixel values within this radial range using the information from the surrounding areas. In this inpainting approach both the tSZ and the kSZ signals are eliminated from the gradient map by using a constrained Gaussian realisation based on the information from the surrounding region Benoit-Lévy et al. (2013).

6.4 Constraining SZ-mass scaling relation

The SPT observed 2500 deg^2 of southern sky for five years (2007 -11) as part of SPT-SZ survey. The SPT-SZ survey detected clusters via their tSZ signatures on CMB temperature maps (Bleem et al., 2015). The SPT-SZ cluster catalog has a total of 513 clusters detected above a signal-to-noise of 4.5 with a mean redshift of 0.55. Baxter et al. (2015) used MLE on temperature maps to measure the average mass of these clusters. In order to eliminate the tSZ bias Baxter et al. (2015) exploited the frequency dependence of tSZ to generate tSZ free maps, however, that resulted in a significant decrease of SNR.

In my new project (Patil et al., in preparation), I will be using the method we developed in 4 and 5 to constrain the mass of the SPT-SZ cluster catalog. This has two advantages over the previous work of Baxter et al. (2015):

- by using a tSZ free gradient map we will completely eliminate tSZ bias
- by subtracting out a tSZ template from the lensing map we will significantly suppress the tSZ variance.

So far I have tested template fitting approach (Patil et al., 2019) on the simulated data. The recovered percentage mass uncertainty for SPT-SZ like cluster catalog is 13%, a significant improvement compared to 3σ detection of Baxter et al. (2015). The timeline for the project is as follows:

- extract cluster cutouts from 90, 150, and 220 GHz SPT-SZ maps (November 2019 -December 2019)
- construct tSZ free maps using ILC technique on 90,150, and 220 GHz (December 2019 - January 2020)
- apply Patil et al. (2019) method to the extracted cutouts (January 2020 - mid-January 2020)
- complete the draft (mid-January 2020 - March 2020)

6.5 Final remarks

The CMB-cluster lensing has come a long way from the detection regime in 2015 (Baxter et al., 2015) to constraining optical richness-mass normalisation parameter by 10% (Geach and Peacock, 2017). In order to fully realise the potential

of CMB-cluster lensing for future surveys we need to develop estimators that are robust to foreground contamination. The major contamination for the CMB cluster lensing in temperature maps is tSZ. In this thesis, we modified quadratic estimators that are robust to the tSZ contamination. However, a lot of work remains to be done in the near future to achieve sub-percent mass uncertainties for future low noise surveys.

The MLE performs better by a factor of two than QE for future low noise surveys (Fig. 3.3). In future we need to work on modifying MLE to make it robust to tSZ systematic and statistical uncertainty. One of the ways to make it robust to the tSZ systematic uncertainty is by marginalising over the tSZ model parameters. While this approach is expected to remove the tSZ systematic, it will slightly affect the SNR and also increases the computational complexity.

As reported in §3.4, dusty galaxies, kinematic Sunyaev-Zel'dovich effect, cluster position, corrleated halos along the line of sight, and density profiles will induce a systematic uncertainty $> 1\%$. In order to claim our sub-percent mass uncertainty we need to robustly address these systematics. Future work needs to be done in developing new/modified estimators that are robust to these systematics. We need precise theoretical models and foreground simulations to accurately quantify the bias for the future CMB-S4 experiment. In addition we also need observational constraints, for example we need CIB and SZ observations of high redshift clusters to confirm the morphologies predicted by simulations.

Bibliography

S. Adachi, M. A. O. Aguilar Faúndez, K. Arnold, C. Baccigalupi, D. Barron, D. Beck, S. Beckman, F. Bianchini, D. Boettger, J. Borrill, J. Carron, S. Chapman, K. Cheung, Y. Chinone, K. Crowley, A. Cukierman, M. Dobbs, H. El Bouhargani, T. Elleflot, J. Errard, G. Fabbian, C. Feng, T. Fujino, N. Galitzki, N. Goeckner-Wald, J. Groh, G. Hall, N. Halverson, T. Hamada, M. Hasegawa, M. Hazumi, C. A. Hill, L. Howe, Y. Inoue, G. Jaehnig, O. Jeong, D. Kaneko, N. Katayama, B. Keating, R. Keskitalo, S. Kikuchi, T. Kisner, N. Krachmalnicoff, A. Kusaka, A. T. Lee, D. Leon, E. Linder, L. N. Lowry, A. Mangu, F. Matsuda, Y. Minami, M. Navaroli, H. Nishino, A. T. P. Pham, D. Poletti, G. Puglisi, C. L. Reichardt, Y. Segawa, M. Silva-Feaver, P. Siritanasak, N. Stebor, R. Stompor, A. Suzuki, O. Tajima, S. Takakura, S. Takatori, D. Tanabe, G. P. Teply, C. Tsai, C. Verges, B. Westbrook, and Y. Zhou. A Measurement of the Degree Scale CMB B-mode Angular Power Spectrum with POLARBEAR. *arXiv e-prints*, art. arXiv:1910.02608, Oct 2019.

Shadab Alam, Metin Ata, Stephen Bailey, Florian Beutler, Dmitry Bizyaev, Jonathan A. Blazek, Adam S. Bolton, Joel R. Brownstein, Angela Burden, Chia-Hsun Chuang, Johan Comparat, Antonio J. Cuesta, Kyle S. Dawson, Daniel J. Eisenstein, Stephanie Escoffier, Héctor Gil-Marín, Jan Niklas Grieb, Nick Hand, Shirley Ho, Karen Kinemuchi, David Kirkby, Francisco Kitaura, Elena Malanushenko, Viktor Malanushenko, Claudia Maraston, Cameron K. McBride, Robert C. Nichol, Matthew D. Olmstead, Daniel Oravetz, Nikhil Padmanabhan, Nathalie Palanque-Delabrouille, Kaike Pan, Marcos Pellejero-Ibanez, Will J. Percival, Patrick Petitjean, Francisco Prada, Adrian M. Price-Whelan, Beth A. Reid, Sergio A. Rodríguez-Torres, Natalie A. Roe, Ashley J. Ross, Nicholas P. Ross, Graziano Rossi, Jose Alberto Rubiño-Martín, Shun Saito, Salvador Salazar-Albornoz, Lado Samushia, Ariel G. Sánchez, Siddharth Satpathy, David J. Schlegel, Donald P. Schneider, Claudia G. Scóccola, Hee-Jong Seo, Erin S. Sheldon, Audrey Simmons, Anže Slosar, Michael A. Strauss, Molly E. C. Swanson, Daniel Thomas, Jeremy L. Tinker, Rita Tojeiro, Mariana Vargas Magaña, Jose Alberto Vazquez, Licia Verde, David A. Wake, Yuting

Wang, David H. Weinberg, Martin White, W. Michael Wood-Vasey, Christophe Yèche, Idit Zehavi, Zhongxu Zhai, and Gong-Bo Zhao. The clustering of galaxies in the completed SDSS-III Baryon Oscillation Spectroscopic Survey: cosmological analysis of the DR12 galaxy sample. *MNRAS*, 470(3):2617–2652, Sep 2017. doi: 10.1093/mnras/stx721.

S. W. Allen, A. E. Evrard, and A. B. Mantz. Cosmological Parameters from Observations of Galaxy Clusters. *ARA&A*, 49:409–470, September 2011. doi: 10.1146/annurev-astro-081710-102514.

M. Arnaud, G. W. Pratt, R. Piffaretti, H. Bohringer, J. H. Croston, and E. Pointecouteau. The universal galaxy cluster pressure profile from a representative sample of nearby systems (REXCESS) and the Y_{SZ} - M_{500} relation. *A&A*, 517:A92+, July 2010. doi: 10.1051/0004-6361/200913416.

J. E. Austermann, K. A. Aird, J. A. Beall, D. Becker, A. Bender, B. A. Benson, L. E. Bleem, J. Britton, J. E. Carlstrom, C. L. Chang, H. C. Chiang, H.-M. Cho, T. M. Crawford, A. T. Crites, A. Datesman, T. de Haan, M. A. Dobbs, E. M. George, N. W. Halverson, N. Harrington, J. W. Henning, G. C. Hilton, G. P. Holder, W. L. Holzapfel, S. Hoover, N. Huang, J. Hubmayr, K. D. Irwin, R. Keisler, J. Kennedy, L. Knox, A. T. Lee, E. Leitch, D. Li, M. Lueker, D. P. Marrone, J. J. McMahon, J. Mehl, S. S. Meyer, T. E. Montroy, T. Natoli, J. P. Nibarger, M. D. Niemack, V. Novosad, S. Padin, C. Pryke, C. L. Reichardt, J. E. Ruhl, B. R. Saliwanchik, J. T. Sayre, K. K. Schaffer, E. Shirokoff, A. A. Stark, K. Story, K. Vanderlinde, J. D. Vieira, G. Wang, R. Williamson, V. Yefremenko, K. W. Yoon, and O. Zahn. SPTpol: an instrument for CMB polarization measurements with the South Pole Telescope. In *Society of Photo-Optical Instrumentation Engineers (SPIE) Conference Series*, volume 8452, September 2012. doi: 10.1117/12.927286.

M. Bartelmann. Arcs from a universal dark-matter halo profile. *A&A*, 313:697–702, September 1996.

M. Bartelmann and P. Schneider. Weak gravitational lensing. *Physics Reports*, 340 (4-5):291–472, Jan 2001. doi: 10.1016/S0370-1573(00)00082-X.

N. Battaglia. The tau of galaxy clusters. *JCAP*, 2016(8):058, Aug 2016. doi: 10.1088/1475-7516/2016/08/058.

D. Baumann, M. G. Jackson, P. Adshead, A. Amblard, A. Ashoorioon, N. Bartolo, R. Bean, M. Beltrán, F. de Bernardis, S. Bird, X. Chen, D. J. H. Chung, L. Colombo, A. Cooray, P. Creminelli, S. Dodelson, J. Dunkley, C. Dvorkin, R. Easther, F. Finelli, R. Flauger, M. P. Hertzberg, K. Jones-Smith, S. Kachru, K. Kadota, J. Khoury, W. H. Kinney, E. Komatsu, L. M. Krauss, J. Lesgourgues, A. Liddle, M. Liguori,

E. Lim, A. Linde, S. Matarrese, H. Mathur, L. McAllister, A. Melchiorri, A. Nicolis, L. Pagano, H. V. Peiris, M. Peloso, L. Pogosian, E. Pierpaoli, A. Riotto, U. Seljak, L. Senatore, S. Shandera, E. Silverstein, T. Smith, P. Vaudrevange, L. Verde, B. Wandelt, D. Wands, S. Watson, M. Wyman, A. Yadav, W. Valkenburg, and M. Zaldarriaga. Probing Inflation with CMB Polarization. In S. Dodelson, D. Baumann, A. Cooray, J. Dunkley, A. Fraisse, M. G. Jackson, A. Kogut, L. Krauss, M. Zaldarriaga, and K. Smith, editors, *American Institute of Physics Conference Series*, volume 1141 of *American Institute of Physics Conference Series*, pages 10–120, June 2009. doi: 10.1063/1.3160885.

E. J. Baxter, R. Keisler, S. Dodelson, K. A. Aird, S. W. Allen, M. L. N. Ashby, M. Bautz, M. Bayliss, B. A. Benson, L. E. Bleem, S. Bocquet, M. Brodwin, J. E. Carlstrom, C. L. Chang, I. Chiu, H.-M. Cho, A. Clocchiatti, T. M. Crawford, A. T. Crites, S. Desai, J. P. Dietrich, T. de Haan, M. A. Dobbs, R. J. Foley, W. R. Forman, E. M. George, M. D. Gladders, A. H. Gonzalez, N. W. Halverson, N. L. Harrington, C. Hennig, H. Hoekstra, G. P. Holder, W. L. Holzapfel, Z. Hou, J. D. Hrubes, C. Jones, L. Knox, A. T. Lee, E. M. Leitch, J. Liu, M. Lueker, D. Luong-Van, A. Mantz, D. P. Marrone, M. McDonald, J. J. McMahon, S. S. Meyer, M. Millea, L. M. Mocanu, S. S. Murray, S. Padin, C. Pryke, C. L. Reichardt, A. Rest, J. E. Ruhl, B. R. Saliwanchik, A. Saro, J. T. Sayre, K. K. Schaffer, E. Shirokoff, J. Song, H. G. Spieler, B. Stalder, S. A. Stanford, Z. Staniszewski, A. A. Stark, K. T. Story, A. van Engelen, K. Vanderlinde, J. D. Vieira, A. Vikhlinin, R. Williamson, O. Zahn, and A. Zenteno. A Measurement of Gravitational Lensing of the Cosmic Microwave Background by Galaxy Clusters Using Data from the South Pole Telescope. *ApJ*, 806:247, June 2015. doi: 10.1088/0004-637X/806/2/247.

E. J. Baxter, S. Raghunathan, T. M. Crawford, P. Fosalba, Z. Hou, G. P. Holder, Y. Omori, S. Patil, E. Rozo, T. M. C. Abbott, J. Annis, K. Aylor, A. Benoit-Lévy, B. A. Benson, E. Bertin, L. Bleem, E. Buckley-Geer, D. L. Burke, J. Carlstrom, A. Carnero Rosell, M. Carrasco Kind, J. Carretero, C. L. Chang, H.-M. Cho, A. T. Crites, M. Crocce, C. E. Cunha, L. N. da Costa, C. B. D'Andrea, C. Davis, T. de Haan, S. Desai, J. P. Dietrich, M. A. Dobbs, S. Dodelson, P. Doel, A. Drlica-Wagner, J. Estrada, W. B. Everett, A. Fausti Neto, B. Flaugher, J. Frieman, J. García-Bellido, E. M. George, E. Gaztanaga, T. Giannantonio, D. Gruen, R. A. Gruendl, J. Gschwend, G. Gutierrez, N. W. Halverson, N. L. Harrington, W. G. Hartley, W. L. Holzapfel, K. Honscheid, J. D. Hrubes, B. Jain, D. J. James, M. Jarvis, T. Jeltema, L. Knox, E. Krause, K. Kuehn, S. Kuhlmann, N. Kuropatkin, O. Lahav, A. T. Lee, E. M. Leitch, T. S. Li, M. Lima, D. Luong-Van, A. Manzotti, M. March, D. P. Marrone, J. L. Marshall, P. Martini, J. J. McMahon, P. Melchior, F. Menanteau,

S. S. Meyer, C. J. Miller, R. Miquel, L. M. Mocanu, J. J. Mohr, T. Natoli, B. Nord, R. L. C. Ogando, S. Padin, A. A. Plazas, C. Pryke, D. Rapetti, C. L. Reichardt, A. K. Romer, A. Roodman, J. E. Ruhl, E. Rykoff, M. Sako, E. Sanchez, J. T. Sayre, V. Scarpine, K. K. Schaffer, R. Schindler, M. Schubnell, I. Sevilla-Noarbe, E. Shirokoff, M. Smith, R. C. Smith, M. Soares-Santos, F. Sobreira, Z. Staniszewski, A. Stark, K. Story, E. Suchyta, G. Tarle, D. Thomas, M. A. Troxel, K. Vanderlinde, J. D. Vieira, A. R. Walker, R. Williamson, Y. Zhang, and J. Zuntz. A Measurement of CMB Cluster Lensing with SPT and DES Year 1 Data. *MNRAS*, February 2018. doi: 10.1093/mnras/sty305.

M. R. Becker and A. V. Kravtsov. On the Accuracy of Weak Lensing Cluster Mass Reconstructions. *ArXiv e-prints*, November 2010.

A. N. Bender, P. A. R. Ade, Z. Ahmed, A. J. Anderson, J. S. Avva, K. Aylor, P. S. Barry, R. Basu Thakur, B. A. Benson, L. S. Bleem, S. Bocquet, K. Byrum, J. E. Carlstrom, F. W. Carter, T. W. Cecil, C. L. Chang, H. M. Cho, J. F. Cliche, T. M. Crawford, A. Cukierman, T. de Haan, E. V. Denison, J. Ding, M. A. Dobbs, S. Dodelson, D. Dutcher, W. Everett, A. Foster, J. Gallicchio, A. Gilbert, J. C. Groh, S. T. Guns, N. W. Halverson, A. H. Harke-Hosemann, N. L. Harrington, J. W. Henning, G. C. Hilton, G. P. Holder, W. L. Holzapfel, N. Huang, K. D. Irwin, O. B. Jeong, M. Jonas, A. Jones, T. S. Khaire, L. Knox, A. M. Kofman, M. Korman, D. L. Kubik, S. Kuhlmann, C. L. Kuo, A. T. Lee, E. M. Leitch, A. E. Lowitz, S. S. Meyer, D. Michalik, J. Montgomery, A. Nadolski, T. Natoli, H. Ngyuen, G. I. Noble, V. Novosad, S. Padin, Z. Pan, J. Pearson, C. M. Posada, W. Quan, S. Raghunathan, A. Rahlin, C. L. Reichardt, J. E. Ruhl, J. T. Sayre, E. Shirokoff, G. Smecher, J. A. Sobrin, A. A. Stark, K. T. Story, A. Suzuki, K. L. Thompson, C. Tucker, L. R. Vale, K. Vand erlinde, J. D. Vieira, G. Wang, N. Whitehorn, W. L. K. Wu, V. Yefremenko, K. W. Yoon, and M. R. Young. Year two instrument status of the SPT-3G cosmic microwave background receiver. In *Millimeter, Submillimeter, and Far-Infrared Detectors and Instrumentation for Astronomy IX*, volume 10708 of *Society of Photo-Optical Instrumentation Engineers (SPIE) Conference Series*, page 1070803, Jul 2018. doi: 10.1117/12.2312426.

A. Benoit-Lévy, T. Déchelette, K. Benabed, J. F. Cardoso, D. Hanson, and S. Prunet. Full-sky CMB lensing reconstruction in presence of sky-cuts. *A&A*, 555:A37, July 2013. doi: 10.1051/0004-6361/201321048.

B. A. Benson, P. A. R. Ade, Z. Ahmed, S. W. Allen, K. Arnold, J. E. Austermann, A. N. Bender, L. E. Bleem, J. E. Carlstrom, C. L. Chang, H. M. Cho, J. F. Cliche, T. M. Crawford, A. Cukierman, T. de Haan, M. A. Dobbs, D. Dutcher, W. Everett,

A. Gilbert, N. W. Halverson, D. Hanson, N. L. Harrington, K. Hattori, J. W. Henning, G. C. Hilton, G. P. Holder, W. L. Holzapfel, K. D. Irwin, R. Keisler, L. Knox, D. Kubik, C. L. Kuo, A. T. Lee, E. M. Leitch, D. Li, M. McDonald, S. S. Meyer, J. Montgomery, M. Myers, T. Natoli, H. Nguyen, V. Novosad, S. Padin, Z. Pan, J. Pearson, C. Reichardt, J. E. Ruhl, B. R. Saliwanchik, G. Simard, G. Smecher, J. T. Sayre, E. Shirokoff, A. A. Stark, K. Story, A. Suzuki, K. L. Thompson, C. Tucker, K. Vanderlinde, J. D. Vieira, A. Vikhlinin, G. Wang, V. Yefremenko, and K. W. Yoon. SPT-3G: a next-generation cosmic microwave background polarization experiment on the South Pole telescope. In *Society of Photo-Optical Instrumentation Engineers (SPIE) Conference Series*, volume 9153 of *Society of Photo-Optical Instrumentation Engineers (SPIE) Conference Series*, page 1, July 2014. doi: 10.1117/12.2057305.

M. Béthermin, H. Dole, G. Lagache, D. Le Borgne, and A. Penin. Modeling the evolution of infrared galaxies: a parametric backward evolution model. *A&A*, 529:A4+, May 2011. doi: 10.1051/0004-6361/201015841.

F. Beutler, C. Blake, M. Colless, D. H. Jones, L. Staveley-Smith, L. Campbell, Q. Parker, W. Saunders, and F. Watson. The 6dF Galaxy Survey: baryon acoustic oscillations and the local Hubble constant. *MNRAS*, 416:3017–3032, October 2011. doi: 10.1111/j.1365-2966.2011.19250.x.

Suman Bhattacharya, Salman Habib, Katrin Heitmann, and Alexey Vikhlinin. Dark Matter Halo Profiles of Massive Clusters: Theory versus Observations. *ApJ*, 766(1): 32, Mar 2013. doi: 10.1088/0004-637X/766/1/32.

BICEP2 and Keck Array Collaborations, P. A. R. Ade, Z. Ahmed, R. W. Aikin, K. D. Alexander, D. Barkats, S. J. Benton, C. A. Bischoff, J. J. Bock, J. A. Brevik, I. Buder, E. Bullock, V. Buza, J. Connors, B. P. Crill, C. D. Dowell, C. Dvorkin, L. Duband, J. P. Filippini, S. Fliescher, S. R. Golwala, M. Halpern, S. Harrison, M. Hasselfield, S. R. Hildebrandt, G. C. Hilton, V. V. Hristov, H. Hui, K. D. Irwin, K. S. Karkare, J. P. Kaufman, B. G. Keating, S. Kefeli, S. A. Kernasovskiy, J. M. Kovac, C. L. Kuo, E. M. Leitch, M. Lueker, P. Mason, K. G. Megerian, C. B. Netterfield, H. T. Nguyen, R. O'Brient, IV Ogburn, R. W., A. Orlando, C. Pryke, C. D. Reintsema, S. Richter, R. Schwarz, C. D. Sheehy, Z. K. Staniszewski, R. V. Sudiwala, G. P. Teply, K. L. Thompson, J. E. Tolan, A. D. Turner, A. G. Vieregg, A. C. Weber, J. Willmert, C. L. Wong, and K. W. Yoon. BICEP2/Keck Array V: Measurements of B-mode Polarization at Degree Angular Scales and 150 GHz by the Keck Array. *ApJ*, 811(2): 126, Oct 2015. doi: 10.1088/0004-637X/811/2/126.

BICEP2 Collaboration, Keck Array Collaboration, P. A. R. Ade, Z. Ahmed, R. W. Aikin, K. D. Alexand er, D. Barkats, S. J. Benton, C. A. Bischoff, J. J. Bock,

R. Bowens-Rubin, J. A. Brevik, I. Buder, E. Bullock, V. Buza, J. Connors, J. Cornelison, B. P. Crill, M. Crumrine, M. Dierickx, L. Duband, C. Dvorkin, J. P. Filippini, S. Fliescher, J. Grayson, G. Hall, M. Halpern, S. Harrison, S. R. Hildebrand t, G. C. Hilton, H. Hui, K. D. Irwin, J. Kang, K. S. Karkare, E. Karpel, J. P. Kaufman, B. G. Keating, S. Kefeli, S. A. Kernasovskiy, J. M. Kovac, C. L. Kuo, N. A. Larsen, K. Lau, E. M. Leitch, M. Lueker, K. G. Megerian, L. Moncelsi, T. Namikawa, C. B. Netterfield, H. T. Nguyen, R. O'Brient, R. W. Ogburn, S. Palladino, C. Pryke, B. Racine, S. Richter, A. Schillaci, R. Schwarz, C. D. Sheehy, A. Soliman, T. St. Germaine, Z. K. Staniszewski, B. Steinbach, R. V. Sudiwala, G. P. Teply, K. L. Thompson, J. E. Tolan, C. Tucker, A. D. Turner, C. Umiltà, A. G. Vieregg, A. Wand ui, A. C. Weber, D. V. Wiebe, J. Willmert, C. L. Wong, W. L. K. Wu, H. Yang, K. W. Yoon, and C. Zhang. Constraints on Primordial Gravitational Waves Using Planck, WMAP, and New BICEP2/Keck Observations through the 2015 Season. *PRL*, 121 (22):221301, Nov 2018. doi: 10.1103/PhysRevLett.121.221301.

L. E. Bleem, B. Stalder, M. Brodwin, M. T. Busha, M. D. Gladders, F. W. High, A. Rest, and R. H. Wechsler. A New Reduction of the Blanco Cosmology Survey: An Optically Selected Galaxy Cluster Catalog and a Public Release of Optical Data Products. *ApJS*, 216:20, January 2015. doi: 10.1088/0067-0049/216/1/20.

S. Bocquet, J. P. Dietrich, T. Schrabback, L. E. Bleem, M. Klein, S. W. Allen, D. E. Applegate, M. L. N. Ashby, M. Bautz, M. Bayliss, B. A. Benson, M. Brodwin, E. Bulbul, R. E. A. Canning, R. Capasso, J. E. Carlstrom, C. L. Chang, I. Chiu, H-M. Cho, A. Clocchiatti, T. M. Crawford, A. T. Crites, T. de Haan, S. Desai, M. A. Dobbs, R. J. Foley, W. R. Forman, G. P. Garmire, E. M. George, M. D. Gladders, A. H. Gonzalez, S. Grandis, N. Gupta, N. W. Halverson, J. Hlavacek-Larrondo, H. Hoekstra, G. P. Holder, W. L. Holzapfel, Z. Hou, J. D. Hrubes, N. Huang, C. Jones, G. Khullar, L. Knox, R. Kraft, A. T. Lee, A. von der Linden, D. Luong-Van, A. Mantz, D. P. Marrone, M. McDonald, J. J. McMahon, S. S. Meyer, L. M. Mocanu, J. J. Mohr, R. G. Morris, S. Padin, S. Patil, C. Pryke, D. Rapetti, C. L. Reichardt, A. Rest, J. E. Ruhl, B. R. Saliwanchik, A. Saro, J. T. Sayre, K. K. Schaffer, E. Shirokoff, B. Stalder, S. A. Stanford, Z. Staniszewski, A. A. Stark, K. T. Story, V. Strazzullo, C. W. Stubbs, K. Vanderlinde, J. D. Vieira, A. Vikhlinin, R. Williamson, and A. Zenteno. Cluster Cosmology Constraints from the 2500 deg$\hat{2}$ SPT-SZ Survey: Inclusion of Weak Gravitational Lensing Data from Magellan and the Hubble Space Telescope. *ApJ*, art. arXiv:1812.01679, Dec 2018.

Paul Bode, Jeremiah P. Ostriker, Renyue Cen, and Hy Trac. Calibration of Nonthermal Pressure in Global Dark Matter Simulations of Clusters of Galaxies. *arXiv e-prints*, art. arXiv:1204.1762, Apr 2012.

M. R. Calabretta and E. W. Greisen. Representations of celestial coordinates in FITS. *A&A*, 395:1077–1122, December 2002. doi: 10.1051/0004-6361:20021327.

Jean-François Cardoso, Maude Le Jeune, Jacques Delabrouille, Marc Betoule, and Guillaume Patanchon. Component Separation With Flexible Models—Application to Multichannel Astrophysical Observations. *IEEE Journal of Selected Topics in Signal Processing*, 2(5):735–746, Nov 2008. doi: 10.1109/JSTSP.2008.2005346.

J. E. Carlstrom, G. P. Holder, and E. D. Reese. Cosmology with the Sunyaev-Zel'dovich Effect. *ARA&A*, 40:643–680, 2002.

J. E. Carlstrom, P. A. R. Ade, K. A. Aird, B. A. Benson, L. E. Bleem, S. Busetti, C. L. Chang, E. Chauvin, H.-M. Cho, T. M. Crawford, A. T. Crites, M. A. Dobbs, N. W. Halverson, S. Heimsath, W. L. Holzapfel, J. D. Hrubes, M. Joy, R. Keisler, T. M. Lanting, A. T. Lee, E. M. Leitch, J. Leong, W. Lu, M. Lueker, D. Luong-van, J. J. McMahon, J. Mehl, S. S. Meyer, J. J. Mohr, T. E. Montroy, S. Padin, T. Plagge, C. Pryke, J. E. Ruhl, K. K. Schaffer, D. Schwan, E. Shirokoff, H. G. Spieler, Z. Staniszewski, A. A. Stark, C. Tucker, K. Vanderlinde, J. D. Vieira, and R. Williamson. The 10 Meter South Pole Telescope. *PASP*, 123:568–581, May 2011. doi: 10.1086/659879.

Hillary L. Child, Salman Habib, Katrin Heitmann, Nicholas Frontiere, Hal Finkel, Adrian Pope, and Vitali Morozov. Halo Profiles and the Concentration-Mass Relation for a ΛCDM Universe. *ApJ*, 859(1):55, May 2018. doi: 10.3847/1538-4357/aabf95.

CMB-S4 Collaboration, K. N. Abazajian, P. Adshead, Z. Ahmed, S. W. Allen, D. Alonso, K. S. Arnold, C. Baccigalupi, J. G. Bartlett, N. Battaglia, B. A. Benson, C. A. Bischoff, J. Borrill, V. Buza, E. Calabrese, R. Caldwell, J. E. Carlstrom, C. L. Chang, T. M. Crawford, F.-Y. Cyr-Racine, F. De Bernardis, T. de Haan, S. di Serego Alighieri, J. Dunkley, C. Dvorkin, J. Errard, G. Fabbian, S. Feeney, S. Ferraro, J. P. Filippini, R. Flauger, G. M. Fuller, V. Gluscevic, D. Green, D. Grin, E. Grohs, J. W. Henning, J. C. Hill, R. Hlozek, G. Holder, W. Holzapfel, W. Hu, K. M. Huffenberger, R. Keskitalo, L. Knox, A. Kosowsky, J. Kovac, E. D. Kovetz, C.-L. Kuo, A. Kusaka, M. Le Jeune, A. T. Lee, M. Lilley, M. Loverde, M. S. Madhavacheril, A. Mantz, D. J. E. Marsh, J. McMahon, P. D. Meerburg, J. Meyers, A. D. Miller, J. B. Munoz, H. N. Nguyen, M. D. Niemack, M. Peloso, J. Peloton, L. Pogosian, C. Pryke, M. Raveri, C. L. Reichardt, G. Rocha, A. Rotti, E. Schaan, M. M. Schmittfull, D. Scott, N. Sehgal, S. Shandera, B. D. Sherwin, T. L. Smith, L. Sorbo, G. D. Starkman, K. T. Story, A. van Engelen, J. D. Vieira, S. Watson, N. Whitehorn, and W. L. Kimmy Wu. CMB-S4 Science Book, First Edition. *ArXiv e-prints*, October 2016.

Ryan J. Cooke, Max Pettini, Kenneth M. Nollett, and Regina Jorgenson. The Primordial Deuterium Abundance of the Most Metal-poor Damped Lyman-α System. *ApJ*, 830(2):148, Oct 2016. doi: 10.3847/0004-637X/830/2/148.

Andrei Cuceu, James Farr, Pablo Lemos, and Andreu Font-Ribera. Baryon Acoustic Oscillations and the Hubble constant: past, present and future. *JCAP*, 2019(10):044, Oct 2019. doi: 10.1088/1475-7516/2019/10/044.

S. Das, T. A. Marriage, P. A. R. Ade, P. Aguirre, M. Amiri, J. W. Appel, L. F. Barrientos, E. S. Battistelli, J. R. Bond, B. Brown, B. Burger, J. Chervenak, M. J. Devlin, S. R. Dicker, W. Bertrand Doriese, J. Dunkley, R. Dünner, T. Essinger-Hileman, R. P. Fisher, J. W. Fowler, A. Hajian, M. Halpern, M. Hasselfield, C. Hernández-Monteagudo, G. C. Hilton, M. Hilton, A. D. Hincks, R. Hlozek, K. M. Huffenberger, D. H. Hughes, J. P. Hughes, L. Infante, K. D. Irwin, J. Baptiste Juin, M. Kaul, J. Klein, A. Kosowsky, J. M. Lau, M. Limon, Y.-T. Lin, R. H. Lupton, D. Marsden, K. Martocci, P. Mauskopf, F. Menanteau, K. Moodley, H. Moseley, C. B. Netterfield, M. D. Niemack, M. R. Nolta, L. A. Page, L. Parker, B. Partridge, B. Reid, N. Sehgal, B. D. Sherwin, J. Sievers, D. N. Spergel, S. T. Staggs, D. S. Swetz, E. R. Switzer, R. Thornton, H. Trac, C. Tucker, R. Warne, E. Wollack, and Y. Zhao. The Atacama Cosmology Telescope: A Measurement of the Cosmic Microwave Background Power Spectrum at 148 and 218 GHz from the 2008 Southern Survey. *ApJ*, 729:62–+, March 2011a. doi: 10.1088/0004-637X/729/1/62.

S. Das, B. D. Sherwin, P. Aguirre, J. W. Appel, J. R. Bond, C. S. Carvalho, M. J. Devlin, J. Dunkley, R. Dünner, T. Essinger-Hileman, J. W. Fowler, A. Hajian, M. Halpern, M. Hasselfield, A. D. Hincks, R. Hlozek, K. M. Huffenberger, J. P. Hughes, K. D. Irwin, J. Klein, A. Kosowsky, R. H. Lupton, T. A. Marriage, D. Marsden, F. Menanteau, K. Moodley, M. D. Niemack, M. R. Nolta, L. A. Page, L. Parker, E. D. Reese, B. L. Schmitt, N. Sehgal, J. Sievers, D. N. Spergel, S. T. Staggs, D. S. Swetz, E. R. Switzer, R. Thornton, K. Visnjic, and E. Wollack. Detection of the Power Spectrum of Cosmic Microwave Background Lensing by the Atacama Cosmology Telescope. *Physical Review Letters*, 107(2):021301–+, July 2011b. doi: 10.1103/PhysRevLett.107.021301.

T. de Haan, B. A. Benson, L. E. Bleem, S. W. Allen, D. E. Applegate, M. L. N. Ashby, M. Bautz, M. Bayliss, S. Bocquet, M. Brodwin, J. E. Carlstrom, C. L. Chang, I. Chiu, H.-M. Cho, A. Clocchiatti, T. M. Crawford, A. T. Crites, S. Desai, J. P. Dietrich, M. A. Dobbs, A. N. Doucouliagos, R. J. Foley, W. R. Forman, G. P. Garmire, E. M. George, M. D. Gladders, A. H. Gonzalez, N. Gupta, N. W. Halverson, J. Hlavacek-Larrondo, H. Hoekstra, G. P. Holder, W. L. Holzapfel, Z. Hou, J. D.

Hrubes, N. Huang, C. Jones, R. Keisler, L. Knox, A. T. Lee, E. M. Leitch, A. von der Linden, D. Luong-Van, A. Mantz, D. P. Marrone, M. McDonald, J. J. McMahon, S. S. Meyer, L. M. Mocanu, J. J. Mohr, S. S. Murray, S. Padin, C. Pryke, D. Rapetti, C. L. Reichardt, A. Rest, J. Ruel, J. E. Ruhl, B. R. Saliwanchik, A. Saro, J. T. Sayre, K. K. Schaffer, T. Schrabback, E. Shirokoff, J. Song, H. G. Spieler, B. Stalder, S. A. Stanford, Z. Staniszewski, A. A. Stark, K. T. Story, C. W. Stubbs, K. Vanderlinde, J. D. Vieira, A. Vikhlinin, R. Williamson, and A. Zenteno. Cosmological Constraints from Galaxy Clusters in the 2500 Square-degree SPT-SZ Survey. *ApJ*, 832:95, November 2016. doi: 10.3847/0004-637X/832/1/95.

G. De Zotti, R. Ricci, D. Mesa, L. Silva, P. Mazzotta, L. Toffolatti, and J. González-Nuevo. Predictions for high-frequency radio surveys of extragalactic sources. *A&A*, 431:893–903, March 2005. doi: 10.1051/0004-6361:20042108.

B. Diemer and A. V. Kravtsov. Dependence of the Outer Density Profiles of Halos on Their Mass Accretion Rate. *ApJ*, 789:1, July 2014. doi: 10.1088/0004-637X/789/1/1.

S. Dodelson. *Modern Cosmology*. Academic Press, 2003.

S. Dodelson. CMB-cluster lensing. *PRD*, 70(2):023009, July 2004. doi: 10.1103/PhysRevD.70.023009.

A. Drlica-Wagner, I. Sevilla-Noarbe, E. S. Rykoff, R. A. Gruendl, B. Yanny, D. L. Tucker, B. Hoyle, A. Carnero Rosell, G. M. Bernstein, K. Bechtol, M. R. Becker, A. Benoit-Lévy, E. Bertin, M. Carrasco Kind, C. Davis, J. de Vicente, H. T. Diehl, D. Gruen, W. G. Hartley, B. Leistedt, T. S. Li, J. L. Marshall, E. Neilsen, M. M. Rau, E. Sheldon, J. Smith, M. A. Troxel, S. Wyatt, Y. Zhang, T. M. C. Abbott, F. B. Abdalla, S. Allam, M. Banerji, D. Brooks, E. Buckley-Geer, D. L. Burke, D. Capozzi, J. Carretero, C. E. Cunha, C. B. D'Andrea, L. N. da Costa, D. L. DePoy, S. Desai, J. P. Dietrich, P. Doel, A. E. Evrard, A. Fausti Neto, B. Flaugher, P. Fosalba, J. Frieman, J. García-Bellido, D. W. Gerdes, T. Giannantonio, J. Gschwend, G. Gutierrez, K. Honscheid, D. J. James, T. Jeltema, K. Kuehn, S. Kuhlmann, N. Kuropatkin, O. Lahav, M. Lima, H. Lin, M. A. G. Maia, P. Martini, R. G. McMahon, P. Melchior, F. Menanteau, R. Miquel, R. C. Nichol, R. L. C. Ogando, A. A. Plazas, A. K. Romer, A. Roodman, E. Sanchez, V. Scarpine, R. Schindler, M. Schubnell, M. Smith, R. C. Smith, M. Soares-Santos, F. Sobreira, E. Suchyta, G. Tarle, V. Vikram, A. R. Walker, R. H. Wechsler, J. Zuntz, and DES Collaboration. Dark Energy Survey Year 1 Results: The Photometric Data Set for Cosmology. *ApJS*, 235:33, April 2018. doi: 10.3847/1538-4365/aab4f5.

A. R. Duffy, J. Schaye, S. T. Kay, and C. Dalla Vecchia. Dark matter halo concentrations in the Wilkinson Microwave Anisotropy Probe year 5 cosmology. *MNRAS*, 390:L64–

L68, October 2008. doi: 10.1111/j.1745-3933.2008.00537.x.

J Dunkley, E Calabrese, J Sievers, G.E Addison, N Battaglia, E.S Battistelli, J.R Bond, S Das, M.JDevlin, R DÃijnner, J.W Fowler, M Gralla, A Hajian, M Halpern, M Hasselfield, A.D Hincks, R Hlozek, J.P Hughes andK.D Irwin, A Kosowsky, T Louis, T.A Marriage, D Marsden, F Menanteau, K Moodley, M Niemack, M.R Nolta, L.A Page, B Partridge, N Sehgal, D.N Spergel, S.T Staggs, E.R Switzer, H Trac, and E Wollack. The atacama cosmology telescope: likelihood for small-scale CMB data. *Journal of Cosmology and Astroparticle Physics*, 2013(07):025–025, jul 2013. doi: 10.1088/1475-7516/2013/07/025. URL `https://doi.org/10.1088%2F1475-7516%2F2013%2F07%2F025`.

J. Einasto and U. Haud. Galactic models with massive corona. I - Method. II - Galaxy. *A&A*, 223:89–106, October 1989.

B. Flaugher, H. T. Diehl, K. Honscheid, T. M. C. Abbott, O. Alvarez, R. Angstadt, J. T. Annis, M. Antonik, O. Ballester, L. Beaufore, G. M. Bernstein, R. A. Bernstein, B. Bigelow, M. Bonati, D. Boprie, D. Brooks, E. J. Buckley-Geer, J. Campa, L. Cardiel-Sas, F. J. Castander, J. Castilla, H. Cease, J. M. Cela-Ruiz, S. Chappa, E. Chi, C. Cooper, L. N. da Costa, E. Dede, G. Derylo, D. L. DePoy, J. de Vicente, P. Doel, A. Drlica-Wagner, J. Eiting, A. E. Elliott, J. Emes, J. Estrada, A. Fausti Neto, D. A. Finley, R. Flores, J. Frieman, D. Gerdes, M. D. Gladders, B. Gregory, G. R. Gutierrez, J. Hao, S. E. Holland, S. Holm, D. Huffman, C. Jackson, D. J. James, M. Jonas, A. Karcher, I. Karliner, S. Kent, R. Kessler, M. Kozlovsky, R. G. Kron, D. Kubik, K. Kuehn, S. Kuhlmann, K. Kuk, O. Lahav, A. Lathrop, J. Lee, M. E. Levi, P. Lewis, T. S. Li, I. Mandrichenko, J. L. Marshall, G. Martinez, K. W. Merritt, R. Miquel, F. Muñoz, E. H. Neilsen, R. C. Nichol, B. Nord, R. Ogando, J. Olsen, N. Palaio, K. Patton, J. Peoples, A. A. Plazas, J. Rauch, K. Reil, J.-P. Rheault, N. A. Roe, H. Rogers, A. Roodman, E. Sanchez, V. Scarpine, R. H. Schindler, R. Schmidt, R. Schmitt, M. Schubnell, K. Schultz, P. Schurter, L. Scott, S. Serrano, T. M. Shaw, R. C. Smith, M. Soares-Santos, A. Stefanik, W. Stuermer, E. Suchyta, A. Sypniewski, G. Tarle, J. Thaler, R. Tighe, C. Tran, D. Tucker, A. R. Walker, G. Wang, M. Watson, C. Weaverdyck, W. Wester, R. Woods, B. Yanny, and DES Collaboration. The Dark Energy Camera. *Astrophysical Journal*, 150:150, November 2015. doi: 10.1088/0004-6256/150/5/150.

Samuel Flender, Lindsey Bleem, Hal Finkel, Salman Habib, Katrin Heitmann, and Gilbert Holder. Simulations of the Pairwise Kinematic Sunyaev-Zel'dovich Signal. *ApJ*, 823(2):98, Jun 2016. doi: 10.3847/0004-637X/823/2/98.

D. Foreman-Mackey, D. W. Hogg, D. Lang, and J. Goodman. emcee: The MCMC

Hammer. *PASP*, 125:306, March 2013. doi: 10.1086/670067.

J. W. Fowler, V. Acquaviva, P. A. R. Ade, P. Aguirre, M. Amiri, J. W. Appel, L. F. Barrientos, E. S. Battistelli, J. R. Bond, B. Brown, B. Burger, J. Chervenak, S. Das, M. J. Devlin, S. R. Dicker, W. B. Doriese, J. Dunkley, R. Dünner, T. Essinger-Hileman, R. P. Fisher, A. Hajian, M. Halpern, M. Hasselfield, C. Hernández-Monteagudo, G. C. Hilton, M. Hilton, A. D. Hincks, R. Hlozek, K. M. Huffenberger, D. H. Hughes, J. P. Hughes, L. Infante, K. D. Irwin, R. Jimenez, J. B. Juin, M. Kaul, J. Klein, A. Kosowsky, J. M. Lau, M. Limon, Y. T. Lin, R. H. Lupton, T. A. Marriage, D. Marsden, K. Martocci, P. Mauskopf, F. Menanteau, K. Moodley, H. Moseley, C. B. Netterfield, M. D. Niemack, M. R. Nolta, L. A. Page, L. Parker, B. Partridge, H. Quintana, B. Reid, N. Sehgal, J. Sievers, D. N. Spergel, S. T. Staggs, D. S. Swetz, E. R. Switzer, R. Thornton, H. Trac, C. Tucker, L. Verde, R. Warne, G. Wilson, E. Wollack, and Y. Zhao. The Atacama Cosmology Telescope: A Measurement of the 600 < ell < 8000 Cosmic Microwave Background Power Spectrum at 148 GHz. *ApJ*, 722(2):1148–1161, Oct 2010. doi: 10.1088/0004-637X/722/2/1148.

G. Gamow. Expanding Universe and the Origin of Elements. *Physical Review*, 70(7-8): 572–573, Oct 1946. doi: 10.1103/PhysRev.70.572.2.

J. E. Geach and J. A. Peacock. Cluster richness-mass calibration with cosmic microwave background lensing. *Nature Astronomy*, 1:795–799, November 2017. doi: 10.1038/s41550-017-0259-1.

E. M. George, C. L. Reichardt, K. A. Aird, B. A. Benson, L. E. Bleem, J. E. Carlstrom, C. L. Chang, H. M. Cho, T. M. Crawford, A. T. Crites, T. de Haan, M. A. Dobbs, J. Dudley, N. W. Halverson, N. L. Harrington, G. P. Holder, W. L. Holzapfel, Z. Hou, J. D. Hrubes, R. Keisler, L. Knox, A. T. Lee, E. M. Leitch, M. Lueker, D. Luong-Van, J. J. McMahon, J. Mehl, S. S. Meyer, M. Millea, L. M. Mocanu, J. J. Mohr, T. E. Montroy, S. Padin, T. Plagge, C. Pryke, J. E. Ruhl, K. K. Schaffer, L. Shaw, E. Shirokoff, H. G. Spieler, Z. Staniszewski, A. A. Stark, K. T. Story, A. van Engelen, K. Vanderlinde, J. D. Vieira, R. Williamson, and O. Zahn. A Measurement of Secondary Cosmic Microwave Background Anisotropies from the 2500 Square-degree SPT-SZ Survey. *ApJ*, 799(2):177, Feb 2015. doi: 10.1088/0004-637X/799/2/177.

J. González-Nuevo, L. Toffolatti, and F. Argüeso. Predictions of the Angular Power Spectrum of Clustered Extragalactic Point Sources at Cosmic Microwave Background Frequencies from Flat and All-Sky Two-dimensional Simulations. *ApJ*, 621(1):1–14, Mar 2005. doi: 10.1086/427425.

K. M. Górski, E. Hivon, A. J. Banday, B. D. Wandelt, F. K. Hansen, M. Reinecke, and M. Bartelmann. HEALPix: A Framework for High-Resolution Discretization and

Fast Analysis of Data Distributed on the Sphere. *ApJ*, 622:759–771, April 2005. doi: 10.1086/427976.

J. Hartlap, P. Simon, and P. Schneider. Why your model parameter confidences might be too optimistic. Unbiased estimation of the inverse covariance matrix. *A&A*, 464: 399–404, March 2007. doi: 10.1051/0004-6361:20066170.

M. Hasselfield, M. Hilton, T. A. Marriage, G. E. Addison, L. F. Barrientos, N. Battaglia, E. S. Battistelli, J. R. Bond, D. Crichton, S. Das, M. J. Devlin, S. R. Dicker, J. Dunkley, R. Dünner, J. W. Fowler, M. B. Gralla, A. Hajian, M. Halpern, A. D. Hincks, R. Hlozek, J. P. Hughes, L. Infante, K. D. Irwin, A. Kosowsky, D. Marsden, F. Menanteau, K. Moodley, M. D. Niemack, M. R. Nolta, L. A. Page, B. Partridge, E. D. Reese, B. L. Schmitt, N. Sehgal, B. D. Sherwin, J. Sievers, C. Sifón, D. N. Spergel, S. T. Staggs, D. S. Swetz, E. R. Switzer, R. Thornton, H. Trac, and E. J. Wollack. The Atacama Cosmology Telescope: Sunyaev-Zel'dovich selected galaxy clusters at 148 GHz from three seasons of data. *JCAP*, 7:008, July 2013. doi: 10.1088/1475-7516/2013/07/008.

S. W. Henderson, R. Allison, J. Austermann, T. Baildon, N. Battaglia, J. A. Beall, D. Becker, F. De Bernardis, J. R. Bond, E. Calabrese, S. K. Choi, K. P. Coughlin, K. T. Crowley, R. Datta, M. J. Devlin, S. M. Duff, J. Dunkley, R. Dünner, A. van Engelen, P. A. Gallardo, E. Grace, M. Hasselfield, F. Hills, G. C. Hilton, A. D. Hincks, R. Hložek, S. P. Ho, J. Hubmayr, K. Huffenberger, J. P. Hughes, K. D. Irwin, B. J. Koopman, A. B. Kosowsky, D. Li, J. McMahon, C. Munson, F. Nati, L. Newburgh, M. D. Niemack, P. Niraula, L. A. Page, C. G. Pappas, M. Salatino, A. Schillaci, B. L. Schmitt, N. Sehgal, B. D. Sherwin, J. L. Sievers, S. M. Simon, D. N. Spergel, S. T. Staggs, J. R. Stevens, R. Thornton, J. Van Lanen, E. M. Vavagiakis, J. T. Ward, and E. J. Wollack. Advanced ACTPol Cryogenic Detector Arrays and Readout. *Journal of Low Temperature Physics*, 184:772–779, August 2016. doi: 10.1007/s10909-016-1575-z.

J. W. Henning, J. T. Sayre, C. L. Reichardt, P. A. R. Ade, A. J. Anderson, J. E. Austermann, J. A. Beall, A. N. Bender, B. A. Benson, L. E. Bleem, J. E. Carlstrom, C. L. Chang, H. C. Chiang, H.-M. Cho, R. Citron, C. Corbett Moran, T. M. Crawford, A. T. Crites, T. de Haan, M. A. Dobbs, W. Everett, J. Gallicchio, E. M. George, A. Gilbert, N. W. Halverson, N. Harrington, G. C. Hilton, G. P. Holder, W. L. Holzapfel, S. Hoover, Z. Hou, J. D. Hrubes, N. Huang, J. Hubmayr, K. D. Irwin, R. Keisler, L. Knox, A. T. Lee, E. M. Leitch, D. Li, A. Lowitz, A. Manzotti, J. J. McMahon, S. S. Meyer, L. Mocanu, J. Montgomery, A. Nadolski, T. Natoli, J. P. Nibarger, V. Novosad, S. Padin, C. Pryke, J. E. Ruhl, B. R. Saliwanchik, K. K.

Schaffer, C. Sievers, G. Smecher, A. A. Stark, K. T. Story, C. Tucker, K. Vanderlinde, T. Veach, J. D. Vieira, G. Wang, N. Whitehorn, W. L. K. Wu, and V. Yefremenko. Measurements of the Temperature and E-mode Polarization of the CMB from 500 Square Degrees of SPTpol Data. *ApJ*, 852:97, January 2018. doi: 10.3847/1538-4357/aa9ff4.

G. Hinshaw, D. Larson, E. Komatsu, D. N. Spergel, C. L. Bennett, J. Dunkley, M. R. Nolta, M. Halpern, R. S. Hill, N. Odegard, L. Page, K. M. Smith, J. L. Weiland, B. Gold, N. Jarosik, A. Kogut, M. Limon, S. S. Meyer, G. S. Tucker, E. Wollack, and E. L. Wright. Nine-year Wilkinson Microwave Anisotropy Probe (WMAP) Observations: Cosmological Parameter Results. *ApJS*, 208:19, October 2013. doi: 10.1088/0067-0049/208/2/19.

Benjamin Horowitz, Simone Ferraro, and Blake D. Sherwin. Reconstructing small-scale lenses from the cosmic microwave background temperature fluctuations. *MNRAS*, 485(3):3919–3929, May 2019. doi: 10.1093/mnras/stz566.

W. Hu and M. White. A CMB polarization primer. *New Astronomy*, 2:323–344, 1997. astro-ph/9706147.

W. Hu, S. DeDeo, and C. Vale. Cluster mass estimators from CMB temperature and polarization lensing. *New Journal of Physics*, 9:441–+, December 2007. doi: 10.1088/1367-2630/9/12/441.

Edwin Hubble. A Relation between Distance and Radial Velocity among Extra-Galactic Nebulae. *Proceedings of the National Academy of Science*, 15(3):168–173, Mar 1929. doi: 10.1073/pnas.15.3.168.

A. Jenkins, C.S̃. Frenk, S. D.M̃. White, J.M̃. Colberg, S. Cole, A.Ẽ. Evrard, H. M.P̃. Couchman, and N. Yoshida. The mass function of dark matter haloes. *MNRAS*, 321:372–384, February 2001.

M. Kamionkowski, A. Kosowsky, and A. Stebbins. Statistics of Cosmic Microwave Background Polarization. *PRD*, 55:7368–7388, June 1997. URL `http://adsabs.harvard.edu/cgi-bin/nph-bib_query?bibcode=1997PhRvD..55.7368K&db_key=AST`.

R. Keisler, C. L. Reichardt, K. A. Aird, B. A. Benson, L. E. Bleem, J. E. Carlstrom, C. L. Chang, H. M. Cho, T. M. Crawford, A. T. Crites, T. de Haan, M. A. Dobbs, J. Dudley, E. M. George, N. W. Halverson, G. P. Holder, W. L. Holzapfel, S. Hoover, Z. Hou, J. D. Hrubes, M. Joy, L. Knox, A. T. Lee, E. M. Leitch, M. Lueker, D. Luong-Van, J. J. McMahon, J. Mehl, S. S. Meyer, M. Millea, J. J. Mohr, T. E. Montroy, T. Natoli, S. Padin, T. Plagge, C. Pryke, J. E. Ruhl, K. K. Schaffer, L. Shaw, E. Shirokoff, H. G. Spieler, Z. Staniszewski, A. A. Stark, K. Story, A. van Engelen, K. Vanderlinde, J. D. Vieira, R. Williamson, and O. Zahn. A Measurement of the

Damping Tail of the Cosmic Microwave Background Power Spectrum with the South Pole Telescope. *ApJ*, 743:28, December 2011. doi: 10.1088/0004-637X/743/1/28.

R. Keisler, S. Hoover, N. Harrington, J. W. Henning, P. A. R. Ade, K. A. Aird, J. E. Austermann, J. A. Beall, A. N. Bender, B. A. Benson, L. E. Bleem, J. E. Carlstrom, C. L. Chang, H. C. Chiang, H. Cho, R. Citron, T. M. Crawford, A. T. Crites, T. de Haan, M. A. Dobbs, W. Everett, J. Gallicchio, J. Gao, E. M. George, A. Gilbert, N. W. Halverson, D. Hanson, G. C. Hilton, G. P. Holder, W. L. Holzapfel, Z. Hou, J. D. Hrubes, N. Huang, J. Hubmayr, K. D. Irwin, L. Knox, A. T. Lee, E. M. Leitch, D. Li, D. Luong-Van, D. P. Marrone, J. J. McMahon, J. Mehl, S. S. Meyer, L. Mocanu, T. Natoli, J. P. Nibarger, V. Novosad, S. Padin, C. Pryke, C. L. Reichardt, J. E. Ruhl, B. R. Saliwanchik, J. T. Sayre, K. K. Schaffer, E. Shirokoff, G. Smecher, A. A. Stark, K. T. Story, C. Tucker, K. Vanderlinde, J. D. Vieira, G. Wang, N. Whitehorn, V. Yefremenko, and O. Zahn. Measurements of Sub-degree B-mode Polarization in the Cosmic Microwave Background from 100 Square Degrees of SPTpol Data. *ApJ*, 807:151, July 2015. doi: 10.1088/0004-637X/807/2/151.

L. J. King and P. Schneider. Cluster mass profiles from weak lensing II. *A&A*, 369: 1–15, Apr 2001. doi: 10.1051/0004-6361:20010030.

J. M. Kovac, E. M. Leitch, C. Pryke, J. E. Carlstrom, N. W. Halverson, and W. L. Holzapfel. Detection of polarization in the cosmic microwave background using DASI. *Nature*, 420:772, December 2002.

Boris Leistedt, Jason D. McEwen, Martin Büttner, and Hiranya V. Peiris. Wavelet reconstruction of E and B modes for CMB polarization and cosmic shear analyses. *MNRAS*, 466(3):3728–3740, Apr 2017. doi: 10.1093/mnras/stw3176.

A. Lewis and A. Challinor. Weak gravitational lensing of the CMB. *Physics Reports*, 429:1–65, June 2006. doi: 10.1016/j.physrep.2006.03.002.

A. Lewis, A. Challinor, and A. Lasenby. Efficient Computation of Cosmic Microwave Background Anisotropies in Closed Friedmann-Robertson-Walker Models. *ApJ*, 538: 473–476, August 2000. doi: 10.1086/309179.

Thibaut Louis, Emily Grace, Matthew Hasselfield, Marius Lungu, Loïc Maurin, Graeme E. Addison, Peter A. R. Ade, Simone Aiola, Rupert Allison, Mandana Amiri, Elio Angile, Nicholas Battaglia, James A. Beall, Francesco de Bernardis, J. Richard Bond, Joe Britton, Erminia Calabrese, Hsiao-mei Cho, Steve K. Choi, Kevin Coughlin, Devin Crichton, Kevin Crowley, Rahul Datta, Mark J. Devlin, Simon R. Dicker, Joanna Dunkley, Rolando Dünner, Simone Ferraro, Anna E. Fox, Patricio Gallardo, Megan Gralla, Mark Halpern, Shawn Henderson, J. Colin Hill, Gene C. Hilton, Matt Hilton, Adam D. Hincks, Renée Hlozek, S. P. Patty Ho, Zhiqi Huang, Jo-

hannes Hubmayr, Kevin M. Huffenberger, John P. Hughes, Leopoldo Infante, Kent Irwin, Simon Muya Kasanda, Jeff Klein, Brian Koopman, Arthur Kosowsky, Dale Li, Mathew Madhavacheril, Tobias A. Marriage, Jeff McMahon, Felipe Menanteau, Kavilan Moodley, Charles Munson, Sigurd Naess, Federico Nati, Laura Newburgh, John Nibarger, Michael D. Niemack, Michael R. Nolta, Carolina Nuñez, Lyman A. Page, Christine Pappas, Bruce Partridge, Felipe Rojas, Emmanuel Schaan, Benjamin L. Schmitt, Neelima Sehgal, Blake D. Sherwin, Jon Sievers, Sara Simon, David N. Spergel, Suzanne T. Staggs, Eric R. Switzer, Robert Thornton, Hy Trac, Jesse Treu, Carole Tucker, Alexander Van Engelen, Jonathan T. Ward, and Edward J. Wollack. The Atacama Cosmology Telescope: two-season ACTPol spectra and parameters. *JCAP*, 2017(6):031, Jun 2017. doi: 10.1088/1475-7516/2017/06/031.

LSST Science Collaboration, P. A. Abell, J. Allison, S. F. Anderson, J. R. Andrew, J. R. P. Angel, L. Armus, D. Arnett, S. J. Asztalos, T. S. Axelrod, and et al. LSST Science Book, Version 2.0. *ArXiv e-prints*, December 2009.

A. D. Ludlow, J. F. Navarro, M. Boylan-Kolchin, P. E. Bett, R. E. Angulo, M. Li, S. D. M. White, C. Frenk, and V. Springel. The mass profile and accretion history of cold dark matter haloes. *MNRAS*, 432:1103–1113, June 2013. doi: 10.1093/mnras/stt526.

M. Lueker, C. L. Reichardt, K. K. Schaffer, O. Zahn, P. A. R. Ade, K. A. Aird, B. A. Benson, L. E. Bleem, J. E. Carlstrom, C. L. Chang, H.-M. Cho, T. M. Crawford, A. T. Crites, T. de Haan, M. A. Dobbs, E. M. George, N. R. Hall, N. W. Halverson, G. P. Holder, W. L. Holzapfel, J. D. Hrubes, M. Joy, R. Keisler, L. Knox, A. T. Lee, E. M. Leitch, J. J. McMahon, J. Mehl, S. S. Meyer, J. J. Mohr, T. E. Montroy, S. Padin, T. Plagge, C. Pryke, J. E. Ruhl, L. Shaw, E. Shirokoff, H. G. Spieler, B. Stalder, Z. Staniszewski, A. A. Stark, K. Vanderlinde, J. D. Vieira, and R. Williamson. Measurements of Secondary Cosmic Microwave Background Anisotropies with the South Pole Telescope. *ApJ*, 719:1045–1066, August 2010. doi: 10.1088/0004-637X/719/2/1045.

E. Macaulay, R. C. Nichol, D. Bacon, D. Brout, T. M. Davis, B. Zhang, B. A. Bassett, D. Scolnic, A. Möller, C. B. D'Andrea, S. R. Hinton, R. Kessler, A. G. Kim, J. Lasker, C. Lidman, M. Sako, M. Smith, M. Sullivan, T. M. C. Abbott, S. Allam, J. Annis, J. Asorey, S. Avila, K. Bechtol, D. Brooks, P. Brown, D. L. Burke, J. Calcino, A. Carnero Rosell, D. Carollo, M. Carrasco Kind, J. Carretero, F. J. Castander, T. Collett, M. Crocce, C. E. Cunha, L. N. da Costa, C. Davis, J. De Vicente, H. T. Diehl, P. Doel, A. Drlica-Wagner, T. F. Eifler, J. Estrada, A. E. Evrard, A. V. Filippenko, D. A. Finley, B. Flaugher, R. J. Foley, P. Fosalba, J. Frieman, L. Gal-

bany, J. García-Bellido, E. Gaztanaga, K. Glazebrook, S. González-Gaitán, D. Gruen, R. A. Gruendl, J. Gschwend, G. Gutierrez, W. G. Hartley, D. L. Hollowood, K. Honscheid, J. K. Hoormann, B. Hoyle, D. Huterer, B. Jain, D. J. James, T. Jeltema, E. Kasai, E. Krause, K. Kuehn, N. Kuropatkin, O. Lahav, G. F. Lewis, T. S. Li, M. Lima, H. Lin, M. A. G. Maia, J. L. Marshall, P. Martini, R. Miquel, P. Nugent, A. Palmese, Y. C. Pan, A. A. Plazas, A. K. Romer, A. Roodman, E. Sanchez, V. Scarpine, R. Schindler, M. Schubnell, S. Serrano, I. Sevilla-Noarbe, R. Sharp, M. Soares-Santos, F. Sobreira, N. E. Sommer, E. Suchyta, E. Swann, M. E. C. Swanson, G. Tarle, D. Thomas, R. C. Thomas, B. E. Tucker, S. A. Uddin, V. Vikram, A. R. Walker, P. Wiseman, and DES Collaboration. First cosmological results using Type Ia supernovae from the Dark Energy Survey: measurement of the Hubble constant. *MNRAS*, 486(2):2184–2196, Jun 2019. doi: 10.1093/mnras/stz978.

M. Madhavacheril, N. Sehgal, R. Allison, N. Battaglia, J. R. Bond, E. Calabrese, J. Caliguiri, K. Coughlin, D. Crichton, R. Datta, M. J. Devlin, J. Dunkley, R. Dünner, K. Fogarty, E. Grace, A. Hajian, M. Hasselfield, J. C. Hill, M. Hilton, A. D. Hincks, R. Hlozek, J. P. Hughes, A. Kosowsky, T. Louis, M. Lungu, J. McMahon, K. Moodley, C. Munson, S. Naess, F. Nati, L. Newburgh, M. D. Niemack, L. A. Page, B. Partridge, B. Schmitt, B. D. Sherwin, J. Sievers, D. N. Spergel, S. T. Staggs, R. Thornton, A. Van Engelen, J. T. Ward, E. J. Wollack, and Atacama Cosmology Telescope Collaboration. Evidence of Lensing of the Cosmic Microwave Background by Dark Matter Halos. *Physical Review Letters*, 114(15):151302, April 2015. doi: 10.1103/PhysRevLett.114.151302.

M. S. Madhavacheril and J. C. Hill. Mitigating Foreground Biases in CMB Lensing Reconstruction Using Cleaned Gradients. *PRD*, (98):023534, July 2018. doi: 10.1103/PhysRevD.98.023534.

A. Mantz, S. W. Allen, H. Ebeling, and D. Rapetti. New constraints on dark energy from the observed growth of the most X-ray luminous galaxy clusters. *MNRAS*, 387:1179–1192, July 2008. doi: 10.1111/j.1365-2966.2008.13311.x.

A. Mantz, S. W. Allen, D. Rapetti, and H. Ebeling. The observed growth of massive galaxy clusters - I. Statistical methods and cosmological constraints. *MNRAS*, 406:1759–1772, August 2010. doi: 10.1111/j.1365-2966.2010.16992.x.

A. B. Mantz, A. von der Linden, S. W. Allen, D. E. Applegate, P. L. Kelly, R. G. Morris, D. A. Rapetti, R. W. Schmidt, S. Adhikari, M. T. Allen, P. R. Burchat, D. L. Burke, M. Cataneo, D. Donovan, H. Ebeling, S. Shandera, and A. Wright. Weighing the giants - IV. Cosmology and neutrino mass. *MNRAS*, 446:2205–2225, January 2015. doi: 10.1093/mnras/stu2096.

A. Manzotti, K. T. Story, W. L. K. Wu, J. E. Austermann, J. A. Beall, A. N. Bender, B. A. Benson, L. E. Bleem, J. J. Bock, J. E. Carlstrom, C. L. Chang, H. C. Chiang, H. Cho, R. Citron, A. Conley, T. M. Crawford, A. T. Crites, T. de Haan, M. A. Dobbs, S. Dodelson, W. Everett, J. Gallicchio, E. M. George, A. Gilbert, N. W. Halverson, N. Harrington, J. W. Henning, G. C. Hilton, G. P. Holder, W. L. Holzapfel, S. Hoover, Z. Hou, J. D. Hrubes, N. Huang, J. Hubmayr, K. D. Irwin, R. Keisler, L. Knox, A. T. Lee, E. M. Leitch, D. Li, J. J. McMahon, S. S. Meyer, L. M. Mocanu, T. Natoli, J. P. Nibarger, V. Novosad, S. Padin, C. Pryke, C. L. Reichardt, J. E. Ruhl, B. R. Saliwanchik, J. T. Sayre, K. K. Schaffer, G. Smecher, A. A. Stark, K. Vanderlinde, J. D. Vieira, M. P. Viero, G. Wang, N. Whitehorn, V. Yefremenko, and M. Zemcov. CMB Polarization B-mode Delensing with SPTpol and Herschel. *ArXiv e-prints*, January 2017.

J. C. Mather, E. S. Cheng, D. A. Cottingham, Jr. Eplee, R. E., D. J. Fixsen, T. Hewagama, R. B. Isaacman, K. A. Jensen, S. S. Meyer, P. D. Noerdlinger, S. M. Read, L. P. Rosen, R. A. Shafer, E. L. Wright, C. L. Bennett, N. W. Boggess, M. G. Hauser, T. Kelsall, Jr. Moseley, S. H., R. F. Silverberg, G. F. Smoot, R. Weiss, and D. T. Wilkinson. Measurement of the Cosmic Microwave Background Spectrum by the COBE FIRAS Instrument. *ApJ*, 420:439, Jan 1994. doi: 10.1086/173574.

I. G. McCarthy, A. M. C. Le Brun, J. Schaye, and G. P. Holder. The thermal Sunyaev-Zel'dovich effect power spectrum in light of Planck. *MNRAS*, 440:3645–3657, June 2014. doi: 10.1093/mnras/stu543.

T. McClintock, T. N. Varga, D. Gruen, E. Rozo, E. S. Rykoff, T. Shin, P. Melchior, J. DeRose, S. Seitz, J. P. Dietrich, E. Sheldon, Y. Zhang, A. v. der Linden, T. Jeltema, A. B. Mantz, A. K. Romer, S. Allen, M. R. Becker, A. Bermeo, S. Bhargava, M. Costanzi, S. Everett, A. Farahi, N. Hamaus, W. G. Hartley, D. L. Hollowood, B. Hoyle, H. Israel, P. Li, N. MacCrann, G. Morris, A. Palmese, A. A. Plazas, G. Pollina, M. M. Rau, M. Simet, M. Soares-Santos, M. A. Troxel, C. V. Cervantes, R. H. Wechsler, J. Zuntz, T. M. C. Abbott, F. B. Abdalla, S. Allam, J. Annis, S. Avila, S. L. Bridle, D. Brooks, D. L. Burke, A. C. Rosell, M. C. Kind, J. Carretero, F. J. Castander, M. Crocce, C. E. Cunha, C. B. D'Andrea, L. N. da Costa, C. Davis, J. De Vicente, H. T. Diehl, P. Doel, A. Drlica-Wagner, A. E. Evrard, B. Flaugher, P. Fosalba, J. Frieman, J. García-Bellido, E. Gaztanaga, D. W. Gerdes, T. Giannantonio, R. A. Gruendl, G. Gutierrez, K. Honscheid, D. J. James, D. Kirk, E. Krause, K. Kuehn, O. Lahav, T. S. Li, M. Lima, M. March, J. L. Marshall, F. Menanteau, R. Miquel, J. J. Mohr, B. Nord, R. L. C. Ogando, A. Roodman, E. Sanchez, V. Scarpine, R. Schindler, I. Sevilla-Noarbe, M. Smith, R. C. Smith, F. Sobreira, E. Suchyta, M. E. C. Swanson, G. Tarle, D. L. Tucker, V. Vikram, A. R. Walker, and

J. Weller. Dark Energy Survey Year 1 Results: Weak Lensing Mass Calibration of redMaPPer Galaxy Clusters. *MNRAS*, October 2018. doi: 10.1093/mnras/sty2711.

P. Melchior, D. Gruen, T. McClintock, T. N. Varga, E. Sheldon, E. Rozo, A. Amara, M. R. Becker, B. A. Benson, A. Bermeo, S. L. Bridle, J. Clampitt, J. P. Dietrich, W. G. Hartley, D. Hollowood, B. Jain, M. Jarvis, T. Jeltema, T. Kacprzak, N. MacCrann, E. S. Rykoff, A. Saro, E. Suchyta, M. A. Troxel, J. Zuntz, C. Bonnett, A. A. Plazas, T. M. C. Abbott, F. B. Abdalla, J. Annis, A. Benoit-Lévy, G. M. Bernstein, E. Bertin, D. Brooks, E. Buckley-Geer, A. Carnero Rosell, M. Carrasco Kind, J. Carretero, C. E. Cunha, C. B. D'Andrea, L. N. da Costa, S. Desai, T. F. Eifler, B. Flaugher, P. Fosalba, J. García-Bellido, E. Gaztanaga, D. W. Gerdes, R. A. Gruendl, J. Gschwend, G. Gutierrez, K. Honscheid, D. J. James, D. Kirk, E. Krause, K. Kuehn, N. Kuropatkin, O. Lahav, M. Lima, M. A. G. Maia, M. March, P. Martini, F. Menanteau, C. J. Miller, R. Miquel, J. J. Mohr, R. C. Nichol, R. Ogando, A. K. Romer, E. Sanchez, V. Scarpine, I. Sevilla-Noarbe, R. C. Smith, M. Soares-Santos, F. Sobreira, M. E. C. Swanson, G. Tarle, D. Thomas, A. R. Walker, J. Weller, and Y. Zhang. Weak-lensing mass calibration of redMaPPer galaxy clusters in Dark Energy Survey Science Verification data. *MNRAS*, 469:4899–4920, August 2017. doi: 10.1093/mnras/stx1053.

J.-B. Melin and J. G. Bartlett. Measuring cluster masses with CMB lensing: a statistical approach. *A&A*, 578:A21, June 2015. doi: 10.1051/0004-6361/201424720.

A. Merloni, P. Predehl, W. Becker, H. Böhringer, T. Boller, H. Brunner, M. Brusa, K. Dennerl, M. Freyberg, P. Friedrich, A. Georgakakis, F. Haberl, G. Hasinger, N. Meidinger, J. Mohr, K. Nandra, A. Rau, T. H. Reiprich, J. Robrade, M. Salvato, A. Santangelo, M. Sasaki, A. Schwope, J. Wilms, and t. German eROSITA Consortium. eROSITA Science Book: Mapping the Structure of the Energetic Universe. *ArXiv e-prints*, September 2012.

Joseph J. Mohr, Brian O'Shea, August E. Evrard, John Bialek, and Zoltan Haiman. Studying dark energy with galaxy cluster surveys. *Nuclear Physics B Proceedings Supplements*, 124:63–67, Jul 2003. doi: 10.1016/S0920-5632(03)02078-4.

E. Morganson, R. A. Gruendl, F. Menanteau, M. Carrasco Kind, Y.-C. Chen, G. Daues, A. Drlica-Wagner, D. N. Friedel, M. Gower, M. W. G. Johnson, M. D. Johnson, R. Kessler, F. Paz-Chinchón, D. Petravick, C. Pond, B. Yanny, S. Allam, R. Armstrong, W. Barkhouse, K. Bechtol, A. Benoit-Lévy, G. M. Bernstein, E. Bertin, E. Buckley-Geer, R. Covarrubias, S. Desai, H. T. Diehl, D. A. Goldstein, D. Gruen, T. S. Li, H. Lin, J. Marriner, J. J. Mohr, E. Neilsen, C.-C. Ngeow, K. Paech, E. S. Rykoff, M. Sako, I. Sevilla-Noarbe, E. Sheldon, F. Sobreira, D. L. Tucker, W. Wester,

and DES Collaboration. The Dark Energy Survey Image Processing Pipeline. *PASP*, 130(7):074501, July 2018. doi: 10.1088/1538-3873/aab4ef.

S. Naess, M. Hasselfield, J. McMahon, M. D. Niemack, G. E. Addison, P. A. R. Ade, R. Allison, M. Amiri, N. Battaglia, J. A. Beall, F. de Bernardis, J. R. Bond, J. Britton, E. Calabrese, H.-m. Cho, K. Coughlin, D. Crichton, S. Das, R. Datta, M. J. Devlin, S. R. Dicker, J. Dunkley, R. Dünner, J. W. Fowler, A. E. Fox, P. Gallardo, E. Grace, M. Gralla, A. Hajian, M. Halpern, S. Henderson, J. C. Hill, G. C. Hilton, M. Hilton, A. D. Hincks, R. Hlozek, P. Ho, J. Hubmayr, K. M. Huffenberger, J. P. Hughes, L. Infante, K. Irwin, R. Jackson, S. Muya Kasanda, J. Klein, B. Koopman, A. Kosowsky, D. Li, T. Louis, M. Lungu, M. Madhavacheril, T. A. Marriage, L. Maurin, F. Menanteau, K. Moodley, C. Munson, L. Newburgh, J. Nibarger, M. R. Nolta, L. A. Page, C. Pappas, B. Partridge, F. Rojas, B. L. Schmitt, N. Sehgal, B. D. Sherwin, J. Sievers, S. Simon, D. N. Spergel, S. T. Staggs, E. R. Switzer, R. Thornton, H. Trac, C. Tucker, M. Uehara, A. Van Engelen, J. T. Ward, and E. J. Wollack. The Atacama Cosmology Telescope: CMB Polarization at 200l9000. *JCAP*, 10:007, October 2014. doi: 10.1088/1475-7516/2014/10/007.

J. F. Navarro, C. S. Frenk, and S. D. M. White. The Structure of Cold Dark Matter Halos. *ApJ*, 462:563–+, May 1996. doi: 10.1086/177173.

J. F. Navarro, C. S. Frenk, and S. D. M. White. A Universal Density Profile from Hierarchical Clustering. *ApJ*, 490:493–+, December 1997. doi: 10.1086/304888.

M. Oguri and T. Hamana. Detailed cluster lensing profiles at large radii and the impact on cluster weak lensing studies. *MNRAS*, 414:1851–1861, July 2011. doi: 10.1111/j.1365-2966.2011.18481.x.

S. Padin, Z. Staniszewski, R. Keisler, M. Joy, A. A. Stark, P. A. R. Ade, K. A. Aird, B. A. Benson, L. E. Bleem, J. E. Carlstrom, C. L. Chang, T. M. Crawford, A. T. Crites, M. A. Dobbs, N. W. Halverson, S. Heimsath, R. E. Hills, W. L. Holzapfel, C. Lawrie, A. T. Lee, E. M. Leitch, J. Leong, W. Lu, M. Lueker, J. J. McMahon, S. S. Meyer, J. J. Mohr, T. E. Montroy, T. Plagge, C. Pryke, J. E. Ruhl, K. K. Schaffer, E. Shirokoff, H. G. Spieler, and J. D. Vieira. South pole telescope optics. *Appl. Opt.*, 47(24):4418–4428, 2008.

Sanjaykumar Patil, Srinivasan Raghunathan, and Christian L. Reichardt. Suppressing the thermal SZ-induced variance in CMB-cluster lensing estimators. *arXiv e-prints*, art. arXiv:1905.07943, May 2019.

A. A. Penzias and R. W. Wilson. A Measurement of Excess Antenna Temperature at 4080 Mc/s. *ApJ*, 142:419–421, July 1965. URL `http://adsabs.harvard.edu/cgi-bin/nph-bib_query?bibcode=1965ApJ...142..419P&db_key=AST`.

S. Perlmutter, G. Aldering, G. Goldhaber, R.Ã. Knop, P. Nugent, P.G̃. Castro, S. Deustua, S. Fabbro, A. Goobar, D.Ẽ. Groom, I.M̃. Hook, A.G̃. Kim, M.Ỹ. Kim, J.C̃. Lee, N.J̃. Nunes, R. Pain, C.R̃. Pennypacker, R. Quimby, C. Lidman, R.S̃. Ellis, M. Irwin, R.G̃. McMahon, P. Ruiz-Lapuente, N. Walton, B. Schaefer, B.J̃. Boyle, A.Ṽ. Filippenko, T. Matheson, A.S̃. Fruchter, N. Panagia, H. J.M̃. Newberg, W.J̃. Couch, and The Supernova Cosmology Project. Measurements of omega and lambda from 42 high-redshift supernovae. *ApJ*, 517:565–586, June 1999. URL `http://adsabs.harvard.edu/cgi-bin/nph-bib_query?bibcode=1999ApJ...517..565P&db_key=AST`.

S. Perlmutter, M.S. Turner, and M. White. Constraining dark energy with type ia supernovae and large scale structure. *PRL*, 83:670, 1999.

Planck Collaboration, P. A. R. Ade, N. Aghanim, C. Armitage-Caplan, M. Arnaud, M. Ashdown, F. Atrio-Barand ela, J. Aumont, C. Baccigalupi, A. J. Banday, and et al. Planck 2013 results. XII. Diffuse component separation. *A&A*, 571:A12, Nov 2014a. doi: 10.1051/0004-6361/201321580.

Planck Collaboration, P. A. R. Ade, N. Aghanim, C. Armitage-Caplan, M. Arnaud, M. Ashdown, F. Atrio-Barand ela, J. Aumont, C. Baccigalupi, A. J. Banday, and et al. Planck 2013 results. XXIV. Constraints on primordial non-Gaussianity. *A&A*, 571:A24, Nov 2014b. doi: 10.1051/0004-6361/201321554.

Planck Collaboration, P. A. R. Ade, N. Aghanim, M. Arnaud, M. Ashdown, J. Aumont, C. Baccigalupi, A. J. Banday, R. B. Barreiro, J. G. Bartlett, and et al. Planck 2015 results. XXIV. Cosmology from Sunyaev-Zeldovich cluster counts. *A&A*, 594:A24, September 2016a. doi: 10.1051/0004-6361/201525833.

Planck Collaboration, P. A. R. Ade, N. Aghanim, M. Arnaud, M. Ashdown, J. Aumont, C. Baccigalupi, A. J. Banday, R. B. Barreiro, J. G. Bartlett, and et al. Planck 2015 results. XIII. Cosmological parameters. *A&A*, 594:A13, September 2016b. doi: 10.1051/0004-6361/201525830.

Planck Collaboration, P. A. R. Ade, N. Aghanim, M. Arnaud, M. Ashdown, J. Aumont, C. Baccigalupi, A. J. Banday, R. B. Barreiro, J. G. Bartlett, et al. Planck 2015 results. XXIV. Cosmology from Sunyaev-Zeldovich cluster counts. *A&A*, 594:A24, September 2016c. doi: 10.1051/0004-6361/201525833.

Planck Collaboration, P. A. R. Ade, N. Aghanim, M. Arnaud, J. Aumont, C. Baccigalupi, A. J. Band ay, R. B. Barreiro, J. G. Bartlett, N. Bartolo, and et al. Planck 2015 results. XXIII. The thermal Sunyaev-Zeldovich effect-cosmic infrared background correlation. *A&A*, 594:A23, Sep 2016d. doi: 10.1051/0004-6361/201527418.

Planck Collaboration, N. Aghanim, Y. Akrami, M. Ashdown, J. Aumont, C. Bacci-

galupi, M. Ballardini, A. J. Banday, R. B. Barreiro, N. Bartolo, S. Basak, R. Battye, K. Benabed, J. P. Bernard, M. Bersanelli, P. Bielewicz, J. J. Bock, J. R. Bond, J. Borrill, F. R. Bouchet, F. Boulanger, M. Bucher, C. Burigana, R. C. Butler, E. Calabrese, J. F. Cardoso, J. Carron, A. Challinor, H. C. Chiang, J. Chluba, L. P. L. Colombo, C. Combet, D. Contreras, B. P. Crill, F. Cuttaia, P. de Bernardis, G. de Zotti, J. Delabrouille, J. M. Delouis, E. Di Valentino, J. M. Diego, O. Doré, M. Douspis, A. Ducout, X. Dupac, S. Dusini, G. Efstathiou, F. Elsner, T. A. Enßlin, H. K. Eriksen, Y. Fantaye, M. Farhang, J. Fergusson, R. Fernandez-Cobos, F. Finelli, F. Forastieri, M. Frailis, E. Franceschi, A. Frolov, S. Galeotta, S. Galli, K. Ganga, R. T. Génova-Santos, M. Gerbino, T. Ghosh, J. González-Nuevo, K. M. Górski, S. Gratton, A. Gruppuso, J. E. Gudmundsson, J. Hamann, W. Hand ley, D. Herranz, E. Hivon, Z. Huang, A. H. Jaffe, W. C. Jones, A. Karakci, E. Keihänen, R. Keskitalo, K. Kiiveri, J. Kim, T. S. Kisner, L. Knox, N. Krachmalnicoff, M. Kunz, H. Kurki-Suonio, G. Lagache, J. M. Lamarre, A. Lasenby, M. Lattanzi, C. R. Lawrence, M. Le Jeune, P. Lemos, J. Lesgourgues, F. Levrier, A. Lewis, M. Liguori, P. B. Lilje, M. Lilley, V. Lindholm, M. López-Caniego, P. M. Lubin, Y. Z. Ma, J. F. Macías-Pérez, G. Maggio, D. Maino, N. Mandolesi, A. Mangilli, A. Marcos-Caballero, M. Maris, P. G. Martin, M. Martinelli, E. Martínez-González, S. Matarrese, N. Mauri, J. D. McEwen, P. R. Meinhold, A. Melchiorri, A. Mennella, M. Migliaccio, M. Millea, S. Mitra, M. A. Miville-Deschênes, D. Molinari, L. Montier, G. Morgante, A. Moss, P. Natoli, H. U. Nørgaard-Nielsen, L. Pagano, D. Paoletti, B. Partridge, G. Patanchon, H. V. Peiris, F. Perrotta, V. Pettorino, F. Piacentini, L. Polastri, G. Polenta, J. L. Puget, J. P. Rachen, M. Reinecke, M. Remazeilles, A. Renzi, G. Rocha, C. Rosset, G. Roudier, J. A. Rubiño-Martín, B. Ruiz-Granados, L. Salvati, M. Sandri, M. Savelainen, D. Scott, E. P. S. Shellard, C. Sirignano, G. Sirri, L. D. Spencer, R. Sunyaev, A. S. Suur-Uski, J. A. Tauber, D. Tavagnacco, M. Tenti, L. Toffolatti, M. Tomasi, T. Trombetti, L. Valenziano, J. Valiviita, B. Van Tent, L. Vibert, P. Vielva, F. Villa, N. Vittorio, B. D. Wand elt, I. K. Wehus, M. White, S. D. M. White, A. Zacchei, and A. Zonca. Planck 2018 results. VI. Cosmological parameters. *arXiv e-prints*, art. arXiv:1807.06209, Jul 2018.

Planck Collaboration, N. Aghanim, Y. Akrami, M. Ashdown, J. Aumont, C. Baccigalupi, M. Ballardini, A. J. Banday, R. B. Barreiro, N. Bartolo, S. Basak, K. Benabed, J. P. Bernard, M. Bersanelli, P. Bielewicz, J. J. Bock, J. R. Bond, J. Borrill, F. R. Bouchet, F. Boulanger, M. Bucher, C. Burigana, R. C. Butler, E. Calabrese, J. F. Cardoso, J. Carron, B. Casaponsa, A. Challinor, H. C. Chiang, L. P. L. Colombo, C. Combet, B. P. Crill, F. Cuttaia, P. de Bernardis, A. de Rosa, G. de Zotti, J. Delabrouille, J. M. Delouis, E. Di Valentino, J. M. Diego, O. Doré, M. Douspis,

A. Ducout, X. Dupac, S. Dusini, G. Efstathiou, F. Elsner, T. A. Enßlin, H. K. Eriksen, Y. Fantaye, R. Fernand ez-Cobos, F. Finelli, M. Frailis, A. A. Fraisse, E. Franceschi, A. Frolov, S. Galeotta, S. Galli, K. Ganga, R. T. Génova-Santos, M. Gerbino, T. Ghosh, Y. Giraud-Héraud, J. González-Nuevo, K. M. Górski, S. Gratton, A. Gruppuso, J. E. Gudmundsson, J. Hamann, W. Handley, F. K. Hansen, D. Herranz, E. Hivon, Z. Huang, A. H. Jaffe, W. C. Jones, E. Keihänen, R. Keskitalo, K. Kiiveri, J. Kim, T. S. Kisner, N. Krachmalnicoff, M. Kunz, H. Kurki-Suonio, G. Lagache, J. M. Lamarre, A. Lasenby, M. Lattanzi, C. R. Lawrence, M. Le Jeune, F. Levrier, A. Lewis, M. Liguori, P. B. Lilje, M. Lilley, V. Lindholm, M. López-Caniego, P. M. Lubin, Y. Z. Ma, J. F. Macías-Pérez, G. Maggio, D. Maino, N. Mandolesi, A. Mangilli, A. Marcos-Caballero, M. Maris, P. G. Martin, E. Martínez-González, S. Matarrese, N. Mauri, J. D. McEwen, P. R. Meinhold, A. Melchiorri, A. Mennella, M. Migliaccio, M. Millea, M. A. Miville-Deschênes, D. Molinari, A. Moneti, L. Montier, G. Morgante, A. Moss, P. Natoli, H. U. Nørgaard-Nielsen, L. Pagano, D. Paoletti, B. Partridge, G. Patanchon, H. V. Peiris, F. Perrotta, V. Pettorino, F. Piacentini, G. Polenta, J. L. Puget, J. P. Rachen, M. Reinecke, M. Remazeilles, A. Renzi, G. Rocha, C. Rosset, G. Roudier, J. A. Rubiño-Martín, B. Ruiz-Granados, L. Salvati, M. Sandri, M. Savelainen, D. Scott, E. P. S. Shellard, C. Sirignano, G. Sirri, L. D. Spencer, R. Sunyaev, A. S. Suur-Uski, J. A. Tauber, D. Tavagnacco, M. Tenti, L. Toffolatti, M. Tomasi, T. Trombetti, J. Valiviita, B. Van Tent, P. Vielva, F. Villa, N. Vittorio, B. D. Wandelt, I. K. Wehus, A. Zacchei, and A. Zonca. Planck 2018 results. V. CMB power spectra and likelihoods. *arXiv e-prints*, art. arXiv:1907.12875, Jul 2019.

POLARBEAR Collaboration. A Measurement of the Cosmic Microwave Background B-mode Polarization Power Spectrum at Sub-degree Scales with POLARBEAR. *ApJ*, 794:171, October 2014. doi: 10.1088/0004-637X/794/2/171.

W.H. Press and P. Schechter. Formation of galaxies and clusters of galaxies by self-similar gravitational condensation. *ApJ*, 187:425, 1974.

C. Pryke, N. W. Halverson, E. M. Leitch, J. Kovac, J. E. Carlstrom, W. L. Holzapfel, and M. Dragovan. Cosmological parameter extraction from the first season of observations with the degree angular scale interferometer. *The Astrophysical Journal*, 568(1):46–51, mar 2002. doi: 10.1086/338880. URL `https://doi.org/10.1086%2F338880`.

S. Raghunathan, S. Patil, E. J. Baxter, F. Bianchini, L. E. Bleem, T. M. Crawford, G. P. Holder, A. Manzotti, and C. L. Reichardt. Measuring galaxy cluster masses with CMB lensing using a Maximum Likelihood estimator: statistical and systematic error budgets for future experiments. *JCAP*, 8:030, August 2017. doi: 10.1088/1475-7516/2017/08/030.

S. Raghunathan, S. Patil, E. Baxter, B. A. Benson, L. E. Bleem, T. L. Chou, T. M. Crawford, G. P. Holder, T. McClintock, C. L. Reichardt, E. Rozo, T. N. Varga, T. M. C. Abbott, P. A. R. Ade, S. Allam, A. J. Anderson, J. Annis, J. E. Austermann, S. Avila, J. A. Beall, K. Bechtol, A. N. Bender, G. Bernstein, E. Bertin, F. Bianchini, D. Brooks, D. L. Burke, J. E. Carlstrom, J. Carretero, C. L. Chang, H. C. Chiang, H.-M. Cho, R. Citron, A. T. Crites, C. E. Cunha, L. N. da Costa, C. Davis, S. Desai, H. T. Diehl, J. P. Dietrich, M. A. Dobbs, P. Doel, T. F. Eifler, W. Everett, A. E. Evrard, B. Flaugher, P. Fosalba, J. Frieman, J. Gallicchio, J. García-Bellido, E. Gaztanaga, E. M. George, A. Gilbert, D. Gruen, R. A. Gruendl, J. Gschwend, N. Gupta, G. Gutierrez, T. de Haan, N. W. Halverson, N. Harrington, W. G. Hartley, J. W. Henning, G. C. Hilton, D. L. Hollowood, W. L. Holzapfel, K. Honscheid, Z. Hou, B. Hoyle, J. D. Hrubes, N. Huang, J. Hubmayr, K. D. Irwin, D. J. James, T. Jeltema, A. G. Kim, M. Carrasco Kind, L. Knox, A. Kovacs, K. Kuehn, N. Kuropatkin, A. T. Lee, T. S. Li, M. Lima, M. A. G. Maia, J. L. Marshall, J. J. McMahon, P. Melchior, F. Menanteau, S. S. Meyer, C. J. Miller, R. Miquel, L. Mocanu, J. Montgomery, A. Nadolski, T. Natoli, J. P. Nibarger, V. Novosad, S. Padin, A. A. Plazas, C. Pryke, D. Rapetti, A. K. Romer, A. Carnero Rosell, J. E. Ruhl, B. R. Saliwanchik, E. Sanchez, J. T. Sayre, V. Scarpine, K. K. Schaffer, M. Schubnell, S. Serrano, I. Sevilla-Noarbe, G. Smecher, R. C. Smith, M. Soares-Santos, F. Sobreira, A. A. Stark, K. T. Story, E. Suchyta, M. E. C. Swanson, G. Tarle, D. Thomas, C. Tucker, K. Vanderlinde, J. De Vicente, J. D. Vieira, G. Wang, N. Whitehorn, W. L. K. Wu, and Y. Zhang. Mass Calibration of Optically Selected DES Clusters Using a Measurement of CMB-cluster Lensing with SPTpol Data. *ApJ*, 872:170, February 2019a. doi: 10.3847/1538-4357/ab01ca.

S. Raghunathan, S. Patil, E. Baxter, B. A. Benson, L. E. Bleem, T. M. Crawford, G. P. Holder, T. McClintock, C. L. Reichardt, T. N. Varga, N. Whitehorn, P. A. R. Ade, S. Allam, A. J. Anderson, J. E. Austermann, S. Avila, J. S. Avva, D. Bacon, J. A. Beall, A. N. Bender, F. Bianchini, S. Bocquet, D. Brooks, D. L. Burke, J. E. Carlstrom, J. Carretero, F. J. Castander, C. L. Chang, H. C. Chiang, R. Citron, M. Costanzi, A. T. Crites, L. N. da Costa, S. Desai, H. T. Diehl, J. P. Dietrich, M. A. Dobbs, P. Doel, S. Everett, A. E. Evrard, C. Feng, B. Flaugher, P. Fosalba, J. Frieman, J. Gallicchio, J. García-Bellido, E. Gaztanaga, E. M. George, T. Giannantonio, A. Gilbert, R. A. Gruendl, J. Gschwend, N. Gupta, G. Gutierrez, T. de Haan, N. W. Halverson, N. Harrington, J. W. Henning, G. C. Hilton, D. L. Hollowood, W. L. Holzapfel, K. Honscheid, J. D. Hrubes, N. Huang, J. Hubmayr, K. D. Irwin, T. Jeltema, M. Carrasco Kind, L. Knox, N. Kuropatkin, O. Lahav, A. T. Lee, D. Li, M. Lima, A. Lowitz, M. A. G. Maia, J. L. Marshall, J. J. McMahon,

P. Melchior, F. Menanteau, S. S. Meyer, R. Miquel, L. M. Mocanu, J. J. Mohr, J. Montgomery, C. Corbett Moran, A. Nadolski, T. Natoli, J. P. Nibarger, G. Noble, V. Novosad, R. L. C. Ogand o, S. Padin, A. A. Plazas, C. Pryke, D. Rapetti, A. K. Romer, A. Roodman, A. Carnero Rosell, E. Rozo, J. E. Ruhl, E. S. Rykoff, B. R. Saliwanchik, E. Sanchez, J. T. Sayre, V. Scarpine, K. K. Schaffer, M. Schubnell, S. Serrano, I. Sevilla-Noarbe, C. Sievers, G. Smecher, M. Smith, M. Soares-Santos, A. A. Stark, K. T. Story, E. Suchyta, M. E. C. Swanson, G. Tarle, C. Tucker, K. Vanderlinde, T. Veach, J. De Vicente, J. D. Vieira, V. Vikram, G. Wang, W. L. K. Wu, V. Yefremenko, and Y. Zhang. A Detection of CMB-Cluster Lensing using Polarization Data from SPTpol. *arXiv e-prints*, art. arXiv:1907.08605, Jul 2019b.

Srinivasan Raghunathan, Gilbert P. Holder, James G. Bartlett, SanjayKumar Patil, Christian L. Reichardt, and Nathan Whitehorn. An Inpainting Approach to Tackle the Kinematic and Thermal SZ Induced Biases in CMB-Cluster Lensing Estimators. *arXiv e-prints*, art. arXiv:1904.13392, Apr 2019c.

A. Refregier, A. Amara, T. D. Kitching, A. Rassat, R. Scaramella, J. Weller, and for the Euclid Imaging Consortium. Euclid Imaging Consortium Science Book. *arXiv e-prints*, art. arXiv:1001.0061, Jan 2010.

C. L. Reichardt, P. A. R. Ade, J. J. Bock, J. R. Bond, J. A. Brevik, C. R. Contaldi, M. D. Daub, J. T. Dempsey, J. H. Goldstein, W. L. Holzapfel, C. L. Kuo, A. E. Lange, M. Lueker, M. Newcomb, J. B. Peterson, J. Ruhl, M. C. Runyan, and Z. Staniszewski. High-Resolution CMB Power Spectrum from the Complete ACBAR Data Set. *ApJ*, 694:1200–1219, April 2009. doi: 10.1088/0004-637X/694/2/1200.

A. G. Riess, A. V. Filippenko, P. Challis, A. Clocchiattia, A. Diercks, P. M. Garnavich, R. L. Gilliland, C. J. Hogan, S. Jha, R. P. Kirshner, B. Leibundgut, M. M. Phillips, D. Reiss, B. P. Schmidt, R. A. Schommer, R. C. Smith, J. Spyromilio, C. Stubbs, N. B. Suntzeff, and J. Tonry. Observational evidence from supernovae for an accelerating universe and a cosmological constant. *Astrophysical Journal*, 116:1009, 1998.

Ashley J. Ross, Lado Samushia, Cullan Howlett, Will J. Percival, Angela Burden, and Marc Manera. The clustering of the SDSS DR7 main Galaxy sample - I. A 4 per cent distance measure at z = 0.15. *MNRAS*, 449(1):835–847, May 2015. doi: 10.1093/mnras/stv154.

E. Rozo, R. H. Wechsler, E. S. Rykoff, J. T. Annis, M. R. Becker, A. E. Evrard, J. A. Frieman, S. M. Hansen, J. Hao, D. E. Johnston, B. P. Koester, T. A. McKay, E. S. Sheldon, and D. H. Weinberg. Cosmological Constraints from the Sloan Digital Sky Survey maxBCG Cluster Catalog. *ApJ*, 708:645–660, January 2010. doi: 10.1088/0004-637X/708/1/645.

E. Rozo, E. S. Rykoff, A. Abate, C. Bonnett, M. Crocce, C. Davis, B. Hoyle, B. Leistedt, H. V. Peiris, R. H. Wechsler, T. Abbott, F. B. Abdalla, M. Banerji, A. H. Bauer, A. Benoit-Lévy, G. M. Bernstein, E. Bertin, D. Brooks, E. Buckley-Geer, D. L. Burke, D. Capozzi, A. C. Rosell, D. Carollo, M. C. Kind, J. Carretero, F. J. Castander, M. J. Childress, C. E. Cunha, C. B. D'Andrea, T. Davis, D. L. DePoy, S. Desai, H. T. Diehl, J. P. Dietrich, P. Doel, T. F. Eifler, A. E. Evrard, A. F. Neto, B. Flaugher, P. Fosalba, J. Frieman, E. Gaztanaga, D. W. Gerdes, K. Glazebrook, D. Gruen, R. A. Gruendl, K. Honscheid, D. J. James, M. Jarvis, A. G. Kim, K. Kuehn, N. Kuropatkin, O. Lahav, C. Lidman, M. Lima, M. A. G. Maia, M. March, P. Martini, P. Melchior, C. J. Miller, R. Miquel, J. J. Mohr, R. C. Nichol, B. Nord, C. R. O'Neill, R. Ogando, A. A. Plazas, A. K. Romer, A. Roodman, M. Sako, E. Sanchez, B. Santiago, M. Schubnell, I. Sevilla-Noarbe, R. C. Smith, M. Soares-Santos, F. Sobreira, E. Suchyta, M. E. C. Swanson, J. Thaler, D. Thomas, S. Uddin, V. Vikram, A. R. Walker, W. Wester, Y. Zhang, and L. N. da Costa. redMaGiC: selecting luminous red galaxies from the DES Science Verification data. *MNRAS*, 461:1431–1450, September 2016. doi: 10.1093/mnras/stw1281.

Barbara Sue Ryden. *Introduction to Cosmology*. Addison-Wesley, 2003.

E. S. Rykoff, E. Rozo, M. T. Busha, C. E. Cunha, A. Finoguenov, A. Evrard, J. Hao, B. P. Koester, A. Leauthaud, B. Nord, M. Pierre, R. Reddick, T. Sadibekova, E. S. Sheldon, and R. H. Wechsler. redMaPPer. I. Algorithm and SDSS DR8 Catalog. *ApJ*, 785:104, April 2014. doi: 10.1088/0004-637X/785/2/104.

E. S. Rykoff, E. Rozo, D. Hollowood, A. Bermeo-Hernandez, T. Jeltema, J. Mayers, A. K. Romer, P. Rooney, A. Saro, C. Vergara Cervantes, R. H. Wechsler, H. Wilcox, T. M. C. Abbott, F. B. Abdalla, S. Allam, J. Annis, A. Benoit-Lévy, G. M. Bernstein, E. Bertin, D. Brooks, D. L. Burke, D. Capozzi, A. Carnero Rosell, M. Carrasco Kind, F. J. Castander, M. Childress, C. A. Collins, C. E. Cunha, C. B. D'Andrea, L. N. da Costa, T. M. Davis, S. Desai, H. T. Diehl, J. P. Dietrich, P. Doel, A. E. Evrard, D. A. Finley, B. Flaugher, P. Fosalba, J. Frieman, K. Glazebrook, D. A. Goldstein, D. Gruen, R. A. Gruendl, G. Gutierrez, M. Hilton, K. Honscheid, B. Hoyle, D. J. James, S. T. Kay, K. Kuehn, N. Kuropatkin, O. Lahav, G. F. Lewis, C. Lidman, M. Lima, M. A. G. Maia, R. G. Mann, J. L. Marshall, P. Martini, P. Melchior, C. J. Miller, R. Miquel, J. J. Mohr, R. C. Nichol, B. Nord, R. Ogando, A. A. Plazas, K. Reil, M. Sahlén, E. Sanchez, B. Santiago, V. Scarpine, M. Schubnell, I. Sevilla-Noarbe, R. C. Smith, M. Soares-Santos, F. Sobreira, J. P. Stott, E. Suchyta, M. E. C. Swanson, G. Tarle, D. Thomas, D. Tucker, S. Uddin, P. T. P. Viana, V. Vikram, A. R. Walker, Y. Zhang, and DES Collaboration. The RedMaPPer Galaxy Cluster Catalog From DES Science Verification Data. *ApJS*, 224:1, May 2016. doi: 10.3847/

0067-0049/224/1/1.

R. K. Sachs and A. M. Wolfe. Perturbations of a Cosmological Model and Angular Variations of the Microwave Background. *ApJ*, 147:73, Jan 1967. doi: 10.1086/148982.

L. Salvati, M. Douspis, and N. Aghanim. Constraints from thermal Sunyaev-Zel'dovich cluster counts and power spectrum combined with CMB. *A&A*, 614:A13, June 2018. doi: 10.1051/0004-6361/201731990.

A. Saro, S. Bocquet, E. Rozo, B. A. Benson, J. Mohr, E. S. Rykoff, M. Soares-Santos, L. Bleem, S. Dodelson, P. Melchior, F. Sobreira, V. Upadhyay, J. Weller, T. Abbott, F. B. Abdalla, S. Allam, R. Armstrong, M. Banerji, A. H. Bauer, M. Bayliss, A. Benoit-Lévy, G. M. Bernstein, E. Bertin, M. Brodwin, D. Brooks, E. Buckley-Geer, D. L. Burke, J. E. Carlstrom, R. Capasso, D. Capozzi, A. Carnero Rosell, M. Carrasco Kind, I. Chiu, R. Covarrubias, T. M. Crawford, M. Crocce, C. B. D'Andrea, L. N. da Costa, D. L. DePoy, S. Desai, T. de Haan, H. T. Diehl, J. P. Dietrich, P. Doel, C. E. Cunha, T. F. Eifler, A. E. Evrard, A. Fausti Neto, E. Fernand ez, B. Flaugher, P. Fosalba, J. Frieman, C. Gangkofner, E. Gaztanaga, D. Gerdes, D. Gruen, R. A. Gruendl, N. Gupta, C. Hennig, W. L. Holzapfel, K. Honscheid, B. Jain, D. James, K. Kuehn, N. Kuropatkin, O. Lahav, T. S. Li, H. Lin, M. A. G. Maia, M. March, J. L. Marshall, Paul Martini, M. McDonald, C. J. Miller, R. Miquel, B. Nord, R. Ogando, A. A. Plazas, C. L. Reichardt, A. K. Romer, A. Roodman, M. Sako, E. Sanchez, M. Schubnell, I. Sevilla, R. C. Smith, B. Stalder, A. A. Stark, V. Strazzullo, E. Suchyta, M. E. C. Swanson, G. Tarle, J. Thaler, D. Thomas, D. Tucker, V. Vikram, A. von der Linden, A. R. Walker, R. H. Wechsler, W. Wester, A. Zenteno, and K. E. Ziegler. Constraints on the richness-mass relation and the optical-SZE positional offset distribution for SZE-selected clusters. *MNRAS*, 454(3):2305–2319, Dec 2015. doi: 10.1093/mnras/stv2141.

J. T. Sayre, C. L. Reichardt, J. W. Henning, P. A. R. Ade, A. J. Anderson, J. E. Austermann, J. S. Avva, J. A. Beall, A. N. Bender, B. A. Benson, F. Bianchini, L. E. Bleem, J. E. Carlstrom, C. L. Chang, H. C. Chiang, R. Citron, C. Corbett Moran, T. M. Crawford, A. T. Crites, T. de Haan, M. A. Dobbs, W. Everett, J. Gallicchio, E. M. George, A. Gilbert, N. Gupta, N. W. Halverson, N. Harrington, G. C. Hilton, G. P. Holder, W. L. Holzapfel, J. D. Hrubes, N. Huang, J. Hubmayr, K. D. Irwin, L. Knox, A. T. Lee, D. Li, A. Lowitz, J. J. McMahon, S. S. Meyer, L. M. Mocanu, J. Montgomery, A. Nadolski, T. Natoli, J. P. Nibarger, G. Noble, V. Novosad, S. Padin, S. Patil, C. Pryke, J. E. Ruhl, B. R. Saliwanchik, K. K. Schaffer, C. Sievers, G. Smecher, A. A. Stark, C. Tucker, K. Vanderlinde, T. Veach, J. D. Vieira, G. Wang,

N. Whitehorn, W. L. K. Wu, and V. Yefremenko. Measurements of B-mode Polarization of the Cosmic Microwave Background from 500 Square Degrees of SPTpol Data. *arXiv e-prints*, art. arXiv:1910.05748, Oct 2019.

S. Y. Sazonov and R. A. Sunyaev. Microwave polarization in the direction of galaxy clusters induced by the cmb quadrupole anisotropy. *MNRAS*, 310:765, December 1999. URL `http://adsabs.harvard.edu/cgi-bin/nph-bib_query?bibcode=1999MNRAS.310..765S&db_key=AST`.

K. K. Schaffer, T. M. Crawford, K. A. Aird, B. A. Benson, L. E. Bleem, J. E. Carlstrom, C. L. Chang, H. M. Cho, A. T. Crites, T. de Haan, M. A. Dobbs, E. M. George, N. W. Halverson, G. P. Holder, W. L. Holzapfel, S. Hoover, J. D. Hrubes, M. Joy, R. Keisler, L. Knox, A. T. Lee, E. M. Leitch, M. Lueker, D. Luong-Van, J. J. McMahon, J. Mehl, S. S. Meyer, J. J. Mohr, T. E. Montroy, S. Padin, T. Plagge, C. Pryke, C. L. Reichardt, J. E. Ruhl, E. Shirokoff, H. G. Spieler, B. Stalder, Z. Staniszewski, A. A. Stark, K. Story, K. Vanderlinde, J. D. Vieira, and R. Williamson. The First Public Release of South Pole Telescope Data: Maps of a 95 deg^2 Field from 2008 Observations. *ApJ*, 743:90, December 2011. doi: 10.1088/0004-637X/743/1/90.

Douglas Scott and George F. Smoot. Cosmic Microwave Background Mini-review. *arXiv e-prints*, art. arXiv:1005.0555, May 2010.

N. Sehgal, P. Bode, S. Das, C. Hernandez-Monteagudo, K. Huffenberger, Y.-T. Lin, J. P. Ostriker, and H. Trac. Simulations of the Microwave Sky. *ApJ*, 709:920–936, February 2010. doi: 10.1088/0004-637X/709/2/920.

M. Seiffert, C. Borys, D. Scott, and M. Halpern. An upper limit to polarized submillimetre emission in Arp 220. *MNRAS*, 374:409–414, January 2007. doi: 10.1111/j.1365-2966.2006.11186.x.

U. Seljak and M. Zaldarriaga. A Line-of-Sight Integration Approach to Cosmic Microwave Background Anisotropies. *ApJ*, 469:437–444, October 1996. URL `http://adsabs.harvard.edu/cgi-bin/nph-bib_query?bibcode=1996ApJ...469..437S&db_key=AST`. astro-ph/9603033.

Mauro Sereno, Cosimo Fedeli, and Lauro Moscardini. Comparison of weak lensing by NFW and Einasto halos and systematic errors. *JCAP*, 2016(1):042, Jan 2016. doi: 10.1088/1475-7516/2016/01/042.

L. D. Shaw, D. Nagai, S. Bhattacharya, and E. T. Lau. Impact of Cluster Physics on the Sunyaev-Zel'dovich Power Spectrum. *ApJ*, 725:1452–1465, December 2010. doi: 10.1088/0004-637X/725/2/1452.

L. D. Shaw, D. H. Rudd, and D. Nagai. Deconstructing the Kinetic SZ Power Spectrum. *ApJ*, 756:15, September 2012. doi: 10.1088/0004-637X/756/1/15.

E. Shirokoff, C. L. Reichardt, L. Shaw, M. Millea, P. A. R. Ade, K. A. Aird, B. A. Benson, L. E. Bleem, J. E. Carlstrom, C. L. Chang, H. M. Cho, T. M. Crawford, A. T. Crites, T. de Haan, M. A. Dobbs, J. Dudley, E. M. George, N. W. Halverson, G. P. Holder, W. L. Holzapfel, J. D. Hrubes, M. Joy, R. Keisler, L. Knox, A. T. Lee, E. M. Leitch, M. Lueker, D. Luong-Van, J. J. McMahon, J. Mehl, S. S. Meyer, J. J. Mohr, T. E. Montroy, S. Padin, T. Plagge, C. Pryke, J. E. Ruhl, K. K. Schaffer, H. G. Spieler, Z. Staniszewski, A. A. Stark, K. Story, K. Vanderlinde, J. D. Vieira, R. Williamson, and O. Zahn. Improved Constraints on Cosmic Microwave Background Secondary Anisotropies from the Complete 2008 South Pole Telescope Data. *ApJ*, 736:61–+, July 2011. doi: 10.1088/0004-637X/736/1/61.

J. Silk. Cosmic black-body radiation and galaxy formation. *ApJ*, 151:459, 1968.

M. Simet, T. McClintock, R. Mandelbaum, E. Rozo, E. Rykoff, E. Sheldon, and R. H. Wechsler. Erratum: Weak Lensing Measurement of the Mass-Richness Relation of SDSS redMaPPer Clusters. *MNRAS*, 480:5385–5385, November 2018. doi: 10.1093/mnras/sty2318.

J. Song, A. Zenteno, B. Stalder, S. Desai, L. E. Bleem, K. A. Aird, R. Armstrong, M. L. N. Ashby, M. Bayliss, G. Bazin, B. A. Benson, E. Bertin, M. Brodwin, J. E. Carlstrom, C. L. Chang, H. M. Cho, A. Clocchiatti, T. M. Crawford, A. T. Crites, T. de Haan, M. A. Dobbs, J. P. Dudley, R. J. Foley, E. M. George, D. Gettings, M. D. Gladders, A. H. Gonzalez, N. W. Halverson, N. L. Harrington, F. W. High, G. P. Holder, W. L. Holzapfel, S. Hoover, J. D. Hrubes, M. Joy, R. Keisler, L. Knox, A. T. Lee, E. M. Leitch, J. Liu, M. Lueker, D. Luong-Van, D. P. Marrone, M. McDonald, J. J. McMahon, J. Mehl, S. S. Meyer, L. Mocanu, J. J. Mohr, T. E. Montroy, T. Natoli, D. Nurgaliev, S. Padin, T. Plagge, C. Pryke, C. L. Reichardt, A. Rest, J. Ruel, J. E. Ruhl, B. R. Saliwanchik, A. Saro, J. T. Sayre, K. K. Schaffer, L. Shaw, E. Shirokoff, R. Šuhada, H. G. Spieler, S. A. Stanford, Z. Staniszewski, A. A. Stark, K. Story, C. W. Stubbs, A. van Engelen, K. Vanderlinde, J. D. Vieira, R. Williamson, and O. Zahn. Redshifts, Sample Purity, and BCG Positions for the Galaxy Cluster Catalog from the First 720 Square Degrees of the South Pole Telescope Survey. *ApJ*, 761:22, December 2012. doi: 10.1088/0004-637X/761/1/22.

K. T. Story, C. L. Reichardt, Z. Hou, R. Keisler, K. A. Aird, B. A. Benson, L. E. Bleem, J. E. Carlstrom, C. L. Chang, H.-M. Cho, T. M. Crawford, A. T. Crites, T. de Haan, M. A. Dobbs, J. Dudley, B. Follin, E. M. George, N. W. Halverson, G. P. Holder, W. L. Holzapfel, S. Hoover, J. D. Hrubes, M. Joy, L. Knox, A. T. Lee, E. M. Leitch, M. Lueker, D. Luong-Van, J. J. McMahon, J. Mehl, S. S. Meyer, M. Millea, J. J. Mohr, T. E. Montroy, S. Padin, T. Plagge, C. Pryke, J. E. Ruhl, J. T. Sayre, K. K.

Schaffer, L. Shaw, E. Shirokoff, H. G. Spieler, Z. Staniszewski, A. A. Stark, A. van Engelen, K. Vanderlinde, J. D. Vieira, R. Williamson, and O. Zahn. A Measurement of the Cosmic Microwave Background Damping Tail from the 2500-Square-Degree SPT-SZ Survey. *ApJ*, 779:86, December 2013. doi: 10.1088/0004-637X/779/1/86.

R.Ã. Sunyaev and Y.B̃. Zel'dovich. Small-scale fluctuations of relic radiation. *Astrophysics and Space Science*, 7:3, 1970. URL `http://adsabs.harvard.edu/cgi-bin/nph-bib_query?bibcode=1970Ap%26SS...7....3S&db_key=AST`.

R. A. Sunyaev and Y. B. Zel'dovich. The Observations of Relic Radiation as a Test of the Nature of X-Ray Radiation from the Clusters of Galaxies. *Comments on Astrophysics and Space Physics*, 4:173–+, November 1972.

A. Suzuki, P. Ade, Y. Akiba, C. Aleman, K. Arnold, C. Baccigalupi, B. Barch, D. Barron, A. Bender, D. Boettger, J. Borrill, S. Chapman, Y. Chinone, A. Cukierman, M. Dobbs, A. Ducout, R. Dunner, T. Elleflot, J. Errard, G. Fabbian, S. Feeney, C. Feng, T. Fujino, G. Fuller, A. Gilbert, N. Goeckner-Wald, J. Groh, T. De Haan, G. Hall, N. Halverson, T. Hamada, M. Hasegawa, K. Hattori, M. Hazumi, C. Hill, W. Holzapfel, Y. Hori, L. Howe, Y. Inoue, F. Irie, G. Jaehnig, A. Jaffe, O. Jeong, N. Katayama, J. Kaufman, K. Kazemzadeh, B. Keating, Z. Kermish, R. Keskitalo, T. Kisner, A. Kusaka, M. Le Jeune, A. Lee, D. Leon, E. Linder, L. Lowry, F. Matsuda, T. Matsumura, N. Miller, K. Mizukami, J. Montgomery, M. Navaroli, H. Nishino, J. Peloton, D. Poletti, G. Puglisi, G. Rebeiz, C. Raum, C. Reichardt, P. Richards, C. Ross, K. Rotermund, Y. Segawa, B. Sherwin, I. Shirley, P. Siritanasak, N. Stebor, R. Stompor, J. Suzuki, O. Tajima, S. Takada, S. Takakura, S. Takatori, A. Tikhomirov, T. Tomaru, B. Westbrook, N. Whitehorn, T. Yamashita, A. Zahn, and O. Zahn. The Polarbear-2 and the Simons Array Experiments. *Journal of Low Temperature Physics*, 184(3-4):805–810, Aug 2016. doi: 10.1007/s10909-015-1425-4.

R. Takahashi, T. Hamana, M. Shirasaki, T. Namikawa, T. Nishimichi, K. Osato, and K. Shiroyama. Full-sky Gravitational Lensing Simulation for Large-area Galaxy Surveys and Cosmic Microwave Background Experiments. *ApJ*, 850:24, November 2017. doi: 10.3847/1538-4357/aa943d.

The Simons Observatory Collaboration, P. Ade, J. Aguirre, Z. Ahmed, S. Aiola, A. Ali, D. Alonso, M. A. Alvarez, K. Arnold, P. Ashton, and et al. The Simons Observatory: Science goals and forecasts. *Journal of Cosmology and Astro-Particle Physics*, 2019 (2):056, Feb 2019. doi: 10.1088/1475-7516/2019/02/056.

J. Tinker, A. V. Kravtsov, A. Klypin, K. Abazajian, M. Warren, G. Yepes, S. Gottlöber, and D. E. Holz. Toward a Halo Mass Function for Precision Cosmology: The Limits of Universality. *ApJ*, 688:709–728, December 2008. doi: 10.1086/591439.

H. Trac, P. Bode, and J. P. Ostriker. Templates for the Sunyaev-Zel'dovich Angular Power Spectrum. *ApJ*, 727:94–+, February 2011. doi: 10.1088/0004-637X/727/2/94.

A. Vikhlinin, A. V. Kravtsov, R. A. Burenin, H. Ebeling, W. R. Forman, A. Hornstrup, C. Jones, S. S. Murray, D. Nagai, H. Quintana, and A. Voevodkin. Chandra Cluster Cosmology Project III: Cosmological Parameter Constraints. *ApJ*, 692:1060–1074, February 2009. doi: 10.1088/0004-637X/692/2/1060.

A. von der Linden, M. T. Allen, D. E. Applegate, P. L. Kelly, S. W. Allen, H. Ebeling, P. R. Burchat, D. L. Burke, D. Donovan, R. G. Morris, R. Blandford, T. Erben, and A. Mantz. Weighing the Giants - I. Weak-lensing masses for 51 massive galaxy clusters: project overview, data analysis methods and cluster images. *MNRAS*, 439: 2–27, March 2014. doi: 10.1093/mnras/stt1945.

S.D.M. White, J.F. Navarro, A.E. Evrard, and C.S. Frenk. The baryon content of galaxy clusters: A challenge to cosmological orthodoxy. *Nature*, 366:429, 1993.

J. Yoo and M. Zaldarriaga. Improved estimation of cluster mass profiles from the cosmic microwave background. *PRD*, 78(8):083002, October 2008. doi: 10.1103/PhysRevD.78.083002.

Íñigo Zubeldia and Anthony Challinor. Cosmological constraints from Planck galaxy clusters with CMB lensing mass bias calibration. *arXiv e-prints*, art. arXiv:1904.07887, Apr 2019.

F. Zwicky. Die Rotverschiebung von extragalaktischen Nebeln. *Helvetica Physica Acta*, 6:110–127, Jan 1933.

Appendix A

Appendix A

A.1 Simulated skies

The MLE presented in this work depends being able to produce large numbers of realistic simulated skies, incorporating a diverse range of astrophysical signals: the CMB (lensed by the galaxy cluster), radio galaxies, dusty galaxies, the kSZ effect, and the tSZ effect. One unique challenge for cluster studies is that the galaxy cluster itself can source most of these signals in addition to contributions from other unrelated haloes. These simulated skies are used for the calculation of the pixel-pixel covariance matrix, and for the creation of mock data sets (§3.2.1). In this appendix, we detail the creation of these these sky simulations.

The sequence of operations is as follows. First, simulations of each signal are created on $50' \times 50'$ boxes with a $0.25'$ pixel resolution. Most of this appendix will focus on how this is done. The CMB maps are then lensed by the galaxy cluster, convolved by a Gaussian beam of the appropriate size, and rebinned to $0.5'$ pixels. This final rebinning reduces the number of map pixels four-fold and substantially speeds up the MLE without significantly reducing the SNR. White, Gaussian instrumental noise is added, with a pixel RMS level based on an experiment's sensitivity, observing time and survey area. For computational reasons, the $50' \times 50'$ box is cut down to the central $10' \times 10'$ area used in the analysis. Finally we point out a subtle effect because of constraining the simulations to a $50' \times 50'$ box. Choosing a smaller box will reduce the background CMB gradient and subsequently the lensing signal generated by the cluster – which will tend to worsen $\Delta M/M$ –. To quantify this, we repeated our simulations with a larger $2^\circ \times 2^\circ$ such that it encompasses the first peak of the CMB. At $\Delta T = 1 \mu K - arcmin$ for a sample of 100,000 clusters, the mass uncertainty $\Delta M/M$ is now 0.237% as opposed to 0.252% in the left panel of Fig. 3.3, a very small effect.

Since we are dealing with very small areas of sky, we adopt the flat-sky ap-

proximation and substitute Fourier transforms for spherical harmonic transforms. The Fourier wavenumber k is related to the multipole ℓ by $k = \sqrt{k_x^2 + k_y^2} = \frac{\ell}{2\pi}$. We define the azimuthal angle ϕ_ℓ as $tan^{-1}(k_y/k_x)$.

A.1.1 Cosmic Microwave Background

To simulate CMB maps that have been lensed by a massive galaxy cluster, we begin by creating T, Q, and U maps that are Gaussian realizations (Kamionkowski et al., 1997) of the CMB power spectra ($C_\ell^{TT}, C_\ell^{TE}, C_\ell^{EE}$, and C_ℓ^{BB}). For these fiducial power spectra, we use the lensed CMB power spectra predicted by `CAMB` (Lewis et al., 2000) for the *Planck* 2015 ΛCDM cosmology[1]. Note that the tensor-to-scalar ratio r is zero in this chain, and there is no contribution from inflationary B-modes (Baumann et al., 2009). By using Gaussian realizations of the lensed CMB power spectra, we are effectively assuming (1) that the lensing due to large-scale structures (LSS) occurs at higher redshift than the galaxy cluster, and (2) that the small non-Gaussianities due to this LSS lensing are negligible. We then lens the T, Q, and U maps using with the cluster convergence profile described in §3.1. We deal with sub-pixel deflection angles by interpolating over the maps using a fifth-degree B-spline interpolation.

A.1.2 Sunyaev-Zel'dovich (SZ) effect

There are two SZ effects of interest: the kinematic SZ (kSZ) effect and the thermal SZ (tSZ) effect. Both SZ effects have contributions from the cluster itself as well as from unrelated haloes. For the latter signal, we assume the best-fit tSZ and kSZ power spectra from George et al. (2015). We use the Shaw et al. (2010) model for the tSZ power spectrum with an overall normalization of $D_{\ell=3000}^{\mathrm{tSZ,150GHz}} = 3.7\ \mu K^2$. For the kSZ spectrum, we take the Shaw et al. (2012) model with an overall normalization of $D_{\ell=3000}^{\mathrm{kSZ}} = 2.9\,\mu K^2$. For the uncorrelated tSZ and kSZ signals, we simply create Gaussian realizations of these two spectra.

In some cases, we wish to study the effect of the kSZ and tSZ signals from the galaxy cluster in question. At these times, we add the cutouts around comparable mass haloes in simulated SZ maps to the simple Gaussian CMB realizations. We use the kSZ maps provided for the Flender et al. (2016) N-body simulations, while for tSZ maps, we use the smoothed-particle hydrodynamics (SPH) simulations of

[1]More specifically, we use the best-fit parameters from the *Planck* 2015 chain that combines the *Planck* 2015 temperature, polarization, lensing power spectra with BAO, H_0, and SNe data (`TT,TE,EE+lowP+lensing+ext` in Table 4 of Planck Collaboration et al. (2016b)).

McCarthy et al. (2014).

We ignore the extremely small polarized SZ signals in all cases. To generate polarization the free electrons of the intracluster medium must be exposed to a quadrupole radiation field, due to the CMB quadrupole mode for tSZ polarization, p_{tSZ}, and to an apparent CMB quadrupole created by the Doppler effect of bulk velocities in the electrons for kSZ polarization, p_{kSZ}. The level of the tSZ polarization is $p_{tSZ} \sim 0.1(\tau_e/0.02)\ \mu K$ while the kSZ polarization level is $p_{kSZ} \sim 0.1\beta_t^2\tau_e\ K$ (Sazonov and Sunyaev, 1999; Carlstrom et al., 2002) where τ_e is the optical depth of the cluster and $\beta_t = v/c$ transverse component of the electron's velocity. The clusters used in this work have $M_{200} = 2 \times 10^{14}\ M_\odot$ and an expected optical depth of $\tau_e \sim 0.004$ (Flender et al., 2016). We assume a velocity, $v = 1000\ km\ s^{-1}$, leading to $p_{tSZ} = 20\,\mathrm{nK}$ and $p_{kSZ} = 2\,\mathrm{nK}$. This level of polarization is negligible.

A.1.3 Radio and Dusty Galaxies

We also create simulated maps of radio and dusty galaxies. These maps include four terms:

1. radio galaxies following a spatial Poisson distribution ($C_\ell^{radio} \propto$ constant),
2. dusty star forming galaxies (DGs) also following a spatial Poisson distribution ($C_\ell^{\mathrm{DG-Po}} \propto$ constant),
3. clustering of DGs ($C_\ell^{\mathrm{DG-clus}} \propto \ell^{0.8}$), and
4. the overdensity of DGs in galaxy clusters

The first three items are uncorrelated with the galaxy cluster and are expected to reduce the SNR of the estimators without biasing the reconstructed lensing mass. However, the relative overdensity of DGs in galaxy clusters can potentially bias the derived masses, and is discussed in §3.4. We assume the galaxies are randomly polarized at the 4% level, based on Manzotti et al. (2017). This 4% level is expected to be an over-estimate for the DGs (Seiffert et al., 2007).

For radio galaxies, we draw a Poisson realization of the number counts as a function of flux (De Zotti et al., 2005). We ignore the clustering of radio galaxies as it is irrelevant at frequencies observed by the CMB telescopes (De Zotti et al., 2005; George et al., 2015). We take a more sophisticated approach for the dusty galaxies to handle the clustering and tSZ-CIB correlation. We

begin by taking a Poisson distribution for the unusually bright dusty galaxies ($> 1\,\mathrm{mJy}$) (Béthermin et al., 2011) . For fainter DGs, we create a set of number density contrast maps $\delta(\hat{\mathbf{n}})^{\mathrm{DG-Po}}$ covering narrow flux bins. We adjust these number density contrast maps to account for the desired clustering and correlation properties as outlined below, and then assign random fluxes to each pixel in Jy/sr (drawn uniformly across the flux bin). The resulting flux maps are then converted to CMB temperature units (μK_{CMB}).

For the tSZ-CIB correlation, we use the tSZ simulations produced by McCarthy et al. (2014) and the $C_\ell^{\mathrm{tSZ\times CIB}}$ cross spectrum measured by George et al. (2015). Using these we produce a tSZ $\times$ CIB correlated map $T(\hat{\mathbf{n}})^{\mathrm{tSZ\times CIB}}$ and a weight map $W(\hat{\mathbf{n}})^{\mathrm{DG\times tSZ}}$ to modify $\delta(\hat{\mathbf{n}})^{\mathrm{DG-Po}}$ as

$$T_\ell \equiv T_\ell^{\mathrm{tSZ\times CIB}} = T_\ell^{\mathrm{tSZ}} \frac{C_\ell^{\mathrm{tSZ\times CIB}}}{C_\ell^{\mathrm{tSZ}}} \tag{A.1}$$

$$W(\hat{\mathbf{n}}) \equiv W(\hat{\mathbf{n}})^{\mathrm{DG\times tSZ}} = \frac{|T(\hat{\mathbf{n}})|}{\sum |T(\hat{\mathbf{n}})|} \tag{A.2}$$

$$\widetilde{\delta}(\hat{\mathbf{n}})^{\mathrm{DG\times tSZ}} = W(\hat{\mathbf{n}})\ \delta(\hat{\mathbf{n}})^{\mathrm{DG-Po}} \tag{A.3}$$

where subscripts ℓ refer to the harmonic space transforms of the CMB map $T(\hat{\mathbf{n}})$. Eq.(A.2) and Eq.(A.3) ensure that the number of point sources are conserved and are predominantly clustered near massive dark matter haloes. For the clustering component of DG we modify Eq.(A.3) following González-Nuevo et al. (2005)

$$\widetilde{\delta}_\ell^{DG} \equiv \widetilde{\delta}_\ell^{\mathrm{DG-Po,clus,tSZ}} = \widetilde{\delta}_\ell^{\mathrm{DG\times tSZ}} \frac{\sqrt{C_\ell^{Po} + C_\ell^{clus}}}{\sqrt{C_\ell^{Po}}} \tag{A.4}$$